Università degli Studi di Padova

Dipartimento di Ingegneria Industriale

Corso di Laurea Magistrale in
Ingegneria Aerospaziale

Systematic Analysis of Nonlinear Reduced-Order Models for Aeroelastic Applications

Relatore: Dr.-Ing. Ernesto Benini

Supervisor: Dr.-Ing. Christian Breitsamter

Tutor: Dipl.-Ing. Maximilian Winter

Laureando: Emanuele Romeo

Matricola: 1061884

Anno Accademico 2014/15

The intuitive mind is a sacred gift
and the rational mind is a faithful servant.

We have created a society that honors the servant
and has forgotten the gift.
-Albert Einstein

Abstract

In order to design and certificate an airplane, the unsteady aerodynamic response imposed by different loads and the system stability must be accurately measured. Since the cruise velocity of modern commercial aircrafts is in the transonic flight regime some nonlinearities can occur due to the shock wave motion and the separated flow on the wings surfaces. Nowadays, computational fluid dynamics (CFD) codes are employed to study complex aerodynamic as well as aeroelastic problems. However, using these codes computational costs are still too high, especially for preliminary design phases and for a coupled structural/aerodynamic analysis. On the other hand, the established techniques for the aeroelastic analysis are usually based on the potential flow theory, which is unable to accurately capture the nonlinearities present in the flow field. Both problems can be solved using the reduced order models (ROMs) with the aim to reduce the computational effort and to capture the principal nonlinearities. Hence, only a limited number of CFD simulations are needed in order to train the ROM. Afterwards, the model can be employed to study different input signals like air turbulence and to build a fluid-structure model.

In this thesis, a radial basis function neural network (RBF-NN) will be used as well as a local linear model tree (LOLIMOT) algorithm of the existing AER-ROM MATLAB-Toolbox as nonlinear unsteady aerodynamic modeling.

Particular emphasis will be given to nonlinear aeroelastic analysis, where the nonlinear ROM will be coupled to a structural model in order to study the persistent periodical neutrally stable solutions, called Limit Cycle Oscillation (LCO). In this field, the NLR7301 supercritical aerofoil will be analysed with the existing ROMs to determine the behaviour of the LCOs that occurs in the transonic regime. Finally, the properties of the obtained LCOs will be compared with those detected in literature using the CFD, in order to determine the accuracy of the application of the ROMs.

Sommario

In fase di progettazione e di certificazione di un velivolo, i carichi aerodinamici non stazionari agenti sul sistema e la stabilità del sistema stesso devono essere accuratamente misurati. Poiché la velocità di crociera dei moderni aeromobili da trasporto è nel regime di volo transonico, possono insorgere non linearità dovute al movimento delle onde d'urto e separazioni di flusso sulla superficie alare. Ad oggi, per studiare le complessità apportate dall'aerodinamica e dall'aeroelasticità, sono stati abitualmente impiegati metodi della fluidodinamica computazionale, *Computational Fluid Dynamics* (CFD). Tuttavia, utilizzando questi metodi i tempi di simulazione sono ancora troppo elevati, particolarmente per le fasi di progettazione preliminare e per lo studio della risposta di un sistema aerodinamico-strutturale accoppiato. D'altra parte, le tecniche oramai affermate per l'analisi aeroelastica sono solitamente basate sul metodo della teoria del flusso a potenziale, le quali non sono in grado di catturare adeguatamente le non linearità presenti nel campo di moto. Entrambi i problemi possono essere risolti impiegando modelli di ordine ridotto, *Reduced Order Models* (ROMs), con lo scopo di ridurre il carico computazionale e catturare le principali non linearità. Pertanto, in questo modo, saranno necessarie soltanto un numero limitato di simulazioni CFD, utilizzate per allenare la rete neurale del modello di ordine ridotto. Successivamente il modello potrà essere impiegato per lo studio di differenti segnali d'ingresso, come una turbolenza dell'aria, e per costruire un modello fluidodinamico-strutturale.
In questa tesi, come modelli di ordine ridotto, verranno utilizzati una rete neurale che ricorre a una funzione radiale come funzione di base, *Radial Basis Function* (RBF), ed un algoritmo lineare locale, *Local Linear Model Tree Algorithm* (LOLIMOT).
Particolare attenzione sarà data all'analisi di stabilità di un sistema aeroelastico, dove il modello non lineare di ordine ridotto verrà accoppiato ad un modello strutturale per studiare la risposta periodica neutralmente stabile chiamata ciclo limite, *Limit Cycle Oscillation* (LCO). In questo campo, il profilo alare supercritico NLR7301 verrà testato con i modelli di ordine ridotto proposti per determinare il comportamento delle oscillazioni di ciclo limite che si instaurano nel regime

transonico. Infine, le proprietà delle oscillazioni di ciclo limite ottenute saranno comparate con quelle ottenute in letteratura mediante simulazioni CFD per determinare l'accuratezza dell'applicazione di sistemi dei ordine ridotto.

Contents

Nomenclature

General quantities

SYMBOL	UNIT	MEANING
Δt	$[s]$	time step
$\Delta \tau$		nondimensional time step
$\vec{f_b}$	$[N \cdot m^{-3}]$	bulk force
$\vec{f}$	$[N]$	force
f	$[Hz]$	frequency
I	$[kg \cdot m^2]$	mass moment of inertia
m	$[kg]$	mass
n		number of degree of freedom
ω	$[rad \cdot s^{-1}]$	circular frequency
T	$[K]$	temperature
t	$[s]$	time
τ		nondimensional time
x, y, z	$[m]$	Cartesian coordinates
$\xi,\ \eta,\ \zeta$	$[m]$	curvilinear coordinates

Aerodynamics

SYMBOL	UNIT	MEANING
α	$[deg]$	angle of attack
b	$[m]$	wingspan
C_L	[-]	aerofoil lift coefficient
C_D	[-]	aerofoil drag coefficient
C_M	[-]	aerofoil pitching moment coefficient
C_p	[-]	pressure coefficient
c	$[m]$	chord
E	$[J \cdot m^{-3}]$	total energy
f	$[m \cdot s^{-2}]$	specific volume force
GAF		generalized aerodynamic forces
k_{red}	[-]	reduced frequency
k		isentropic coefficient
L	$[N]$	lift force
M	$[N \cdot m]$	pitching moment
Ma	[-]	Mach number
ν	$[m^2 \cdot s^{-1}]$	kinematic viscosity
p	$[N \cdot m^{-2}]$	pressure
q	$[N \cdot m^{-2}]$	dynamic pressure
q	$[J]$	heat
R	$[J \cdot kg^{-1} \cdot K^{-1}]$	specific gas constant
Re	[-]	Reynolds number
ρ	$[kg \cdot m^{-3}]$	density
S	$[m^2]$	surface element
τ		shear stress tensor
$\vec{u}$	$[m \cdot s^{-1}]$	velocity
V	$[m \cdot s^{-1}]$	velocity (norm)

Structural dynamics

Symbol	Unit	Meaning
a	$[m]$	amplitude
α		modal amplitude
$\boldsymbol{D}$		damping matrix
$\underline{\boldsymbol{D}}$		modal damping matrix
δ		Kronecker delta
$\boldsymbol{\Phi}$		modal matrix
$\vec{\Phi}$		eigenvector
$\boldsymbol{I}$		identity matrix
$\boldsymbol{K}$		stiffness matrix
$\underline{\boldsymbol{K}}$		modal stiffness matrix
$\boldsymbol{M}$		mass matrix
$\underline{\boldsymbol{M}}$		modal mass matrix
$\vec{q}$	$[m]$	modal displacements vector
$\vec{y}$	$[m]$	structural deflections vector
ξ		damping ratio

Reduced order model

SYMBOL	UNIT	MEANING
$\vec{c}$	$[m]$	center vector
Δ		extension of the hyperrectangle
e		error
$\vec{\theta}$		hidden layer parameter vector
I		loss function
k_σ		proportionality factor
M		number of hidden layer neurons
m		delay input order
n		delay output order
ϕ		basis function
p		dimensional input space
$\vec{\sum}$		norm matrix
σ		standard deviation
$\vec{u}$	$[m]$	input vector
w		output layer weight
x	$[m]$	distance
$\vec{y}$	$[m]$	output vector

Subscripts

SUBSCRIPT	MEANING
α	pitch
cr	critic
f	flutter
gen	generalized
h	heave
∞	far-field
k	time step number
LCO	limit cycle oscillation
$pred$	predictor
red	reduced
ref	reference

List of Abbreviations

Abbreviation	Meaning
AER	Lehrstuhl für **Aer**odynamik und Strömungsmechanik
APRBS	**A**mplitude Modulated **P**seudo **R**andom **B**inary **S**ignal
ARX	**A**uto**r**egressive with E**x**ogeneous Input
B-L-D-S	**D**egani **S**chiff modified **B**aldwin-**L**omax Turbulence Model
CFD	**C**omputational **F**luid **D**ynamics
CSD	**C**omputational **S**tructural **D**ynamics
DOF	**D**egree **O**f **F**reedom
Eu	**Eu**ler
FEM	**F**inite **E**lement **M**ethod
GAF	**G**eneralized **A**erodynamic **F**orces
HLM	**H**ybrid **L**inear **M**ultistep
IALM	**A**dams **L**inear **M**ultistep Scheme
IPS	**I**nfinite **P**lane **S**pline
LCO	**L**imit **C**ycle **O**scillation
LLM	**L**ocal **L**inear **M**odel
LOLIMOT	**Lo**cal **Li**near **Mo**del **T**ree Algorithm
LU-SSOR	**L**ower **U**pper **S**ymmetric **S**uccessive **O**ver**r**elaxation
MIMO	**M**ulti **I**nput **M**ulti **O**utput
NARX	**N**onlinear **A**uto**r**egressive with E**x**ogeneous Input
NASA	**N**ational **A**eronautics and **S**pace **A**dministration
NN	**N**eural **N**etwork
OLS	**O**rthogonal **L**east **S**quare Algorithm
PDE	**P**artial **D**ifferential **E**quation

Abbreviation	Meaning
POD	**P**roper **O**rthogonal **D**ecomposition
PRBS	**P**seudo **R**andom **B**inary **S**ignal
PSD	**P**ower **S**pectral **D**ensity
RANS	**R**eynolds-**A**veraged **N**avier-**S**tokes
RBF	**R**adial **B**asis **F**unction
ROM	**R**educed **O**rder **M**odel
RSS	**R**andom **S**inusoidal **S**ignal
S-A	**S**palart **A**llmaras Turbulence Model
SCW	**S**uper **C**ritical **W**ing
TFI	**T**rans**f**inite **I**nterpolation
TPS	**T**hin **P**late **S**pline
TSS	**T**ransonic **S**hock **S**eparation
TUM	**T**echnische **U**niverität **M**ünchen

List of Figures

List of Tables

Chapter 1

Introduction

Nowadays, most modern commercial transport aircrafts, as well as fighter planes, operate in a transonic flow regime. Hence, there is the need to stimulate these conditions during the design phases using methods that can accurately simulate the aerodynamic conditions and the behaviours that aerodynamics drives on the structure. This kind of interaction leads to the so called aeroelasticity, which describes the relation between the aerodynamic, the inertia and elastic forces for a flexible structure. This subject can be summarized by the classical Collar aeroelastic triangle, Figure 1.1, which shows how the fundamental aeroelastic phenomena result from the interaction of three types of forces. Two fundamental types of aeroelastic problem occur. One involves the interaction of aerodynamic and elastic forces and it takes the name of *static aeroelasticity*, which considers the nonoscillatory effects of the aerodynamic forces acting on a flexible structure and leads to phenomena like *divergence* and *control reversal*. The second class of problems involves the inertia of the structure as well as aerodynamic and elastic forces and it is called *dynamic aeroelasticity*. Dynamic loading system induces oscillations of structural components. When the natural or resonant frequency of the component is in the region of the frequency of the applied loads, then the amplitude of the oscillations may diverge causing failure (flutter). Also, the presence of fluctuating loads is a fatigue hazard. In this group are included *flutter*, *buffeting* and *limit cycle oscillations* (LCO). The aeroelastic phenomena can be summarized in the

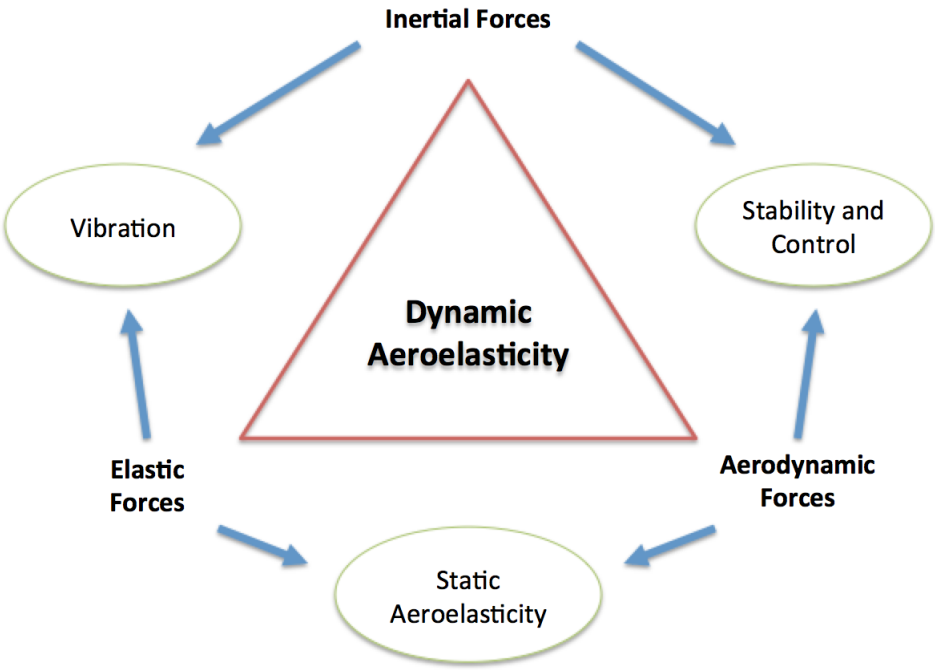

Figure 1.1: Collar aeroelastic triangle

form of a "tree", as in Figure 1.2, [38, 12, 39].

In this work only the nonlinear aeroelastic response of the system will be treated, especially the amplitude limit cycle oscillation (LCO), which can be considered as bounded flutter. This phenomenon arises from classical nonlinearities, as cubic spring, free play, hysteresis and control surface and occurs primarily in the transonic flight regime or at a large angle of attack. Some researchers believe that the LCO is a purely aerodynamic phenomenon, due to transonic shock oscillation and shock induced flow separation, which is sometimes referred to the transonic shock/separation (TSS) model suggested by Edwards [18]. The physical understanding of the LCO is of technical interest for an accurate prediction of the nonlinear response of the system and to extend the operational flight regime. In order to design a safe structure, it is obvious that the LCOs have to be of sufficiently small amplitudes so that the structure does not fail under this kind of vibration exceeding its ultimate load limit. Hence, the study of the limit cycle

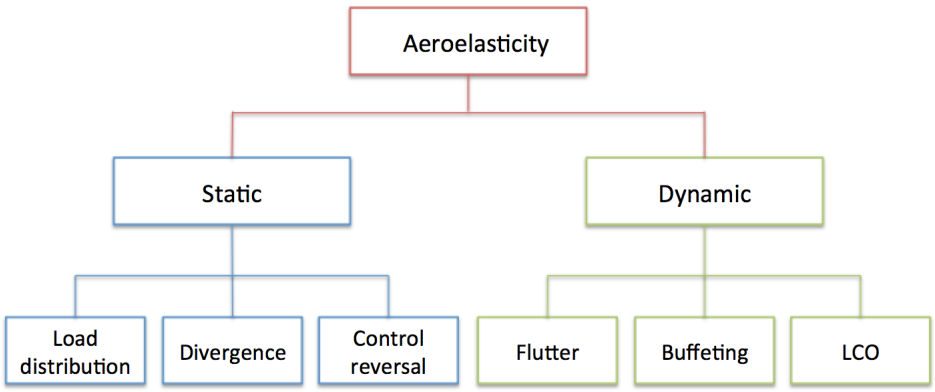

Figure 1.2: Aeroelastic "tree"

oscillations becomes a fatigue problem.

LCOs have been studied in Tang et al. [7] and Vio et al. [15] using computational fluid dynamics (CFD) codes. However, these kinds of codes involve millions of degree of freedom, which limit their applications in optimal design. CFD codes are system of Partial differential Equation (PDE) that can be discretized and solved with numerical algorithms, but with a high computational cost, even with today's powerful computers [6].

Reduced Order Models (ROMs) are a set of numerical structures that allow to construct and reproduce a nonlinear system with a small number of degrees of freedom (DOF). Thus, they can give a simple formulation of the generic nonlinear problem, once they are able to capture the main fundamental dynamics embedded in the system [6, 27]. In the last year the uses of ROMs have increased in the analysis of physical system, because numerical simulations have two main problems. The direct simulation (CFD) can provide a detailed response of the system, but such results don't help the user to understand the physics of the problem better. Furthermore, without powerful computers, the simulations of large scale problems remain unworkable in various design phases, where fast simulations are needed [12].

Reduced order models help to capture physical phenomena, like limit cycle oscillation behaviour mantaining a low number of DOF [12]. Using a ROM is possible

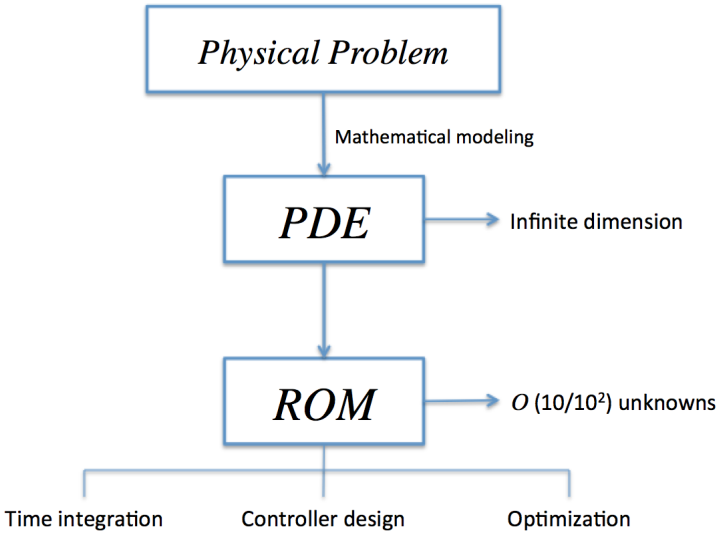

Figure 1.3: Flow chart of a reduced order analysis

to provide an accurate description of the system's dynamic with a lower computational cost than that required by a direct simulation. Hence, such order reduction models project the full order system, with a high number of DOFs, into a much smaller space, which can reproduce the fundamental dynamics of the system [6, 11], as shown in Figure 1.3.

In order to reduce the computational effort different methods for modeling nonlinear system with few DOF have been developed during the last years. However, most of the ROM proposed to predict the aerodynamic behaviour are for linear models, like the proper orthogonal decomposition (POD) [10, 11], first order Volterra series [8] and autoregressive with exogeneous input model (ARX) [40]. This means that the ROM behaves like a linear system near the reference solution, in which the aerodynamic load is proportional to the structural motion.

Modern airplanes that flight near the transonic domain requires special attention during the design phase, because of nonlinearity. The potential based methods are not adequate when strong shocks are present in the flow field and in this situation the Euler's model is required. In case of very strong shocks the latter model can't be used, because it neglects the effect of thermal conductivity. Another more com-

plex case is the viscous case with the possibility of large flow separation [1]. All these cases can be predicted by high fidelity CFD codes. However, coupling the CFD with a structural solver for the aeroelastic analysis can be expensive from the computational point of view, even with high-performance computers. Moreover, during the conceptual and preliminary design phases of an aircraft several simple models are required to predict the dynamic response of the system using a little computational effort.

In the current thesis, in order to capture the nonlinear behaviour of the system and reduce the design computational cost, several reduced order models has been constructed using the *radial basis function* (RBF) neural network model, as suggested by Zhang et al. [39], and the *local linear model tree algorithm* (LOLIMOT). The aerodynamic reduced order models are then coupled to the structural dynamics permitting a fast simulation of the resulting nonlinear aeroelastic system, which will be employed for the LCOs study.

Chapter 2

Theoretical Basis

Fluid dynamics and its relative properties, as well as structural dynamics are the theoretical basis of this work.
The characteristics of a viscous flow are described by the Navier-Stokes equations, which can be solved at high computational costs. In order to reduce the computational effort and hence the time required for the flow solution, the Euler model has been used, which considers the flow inviscid, without any viscous effect. In section 2.1.1, the fundamental equations and the relevant differences of the Navier-Stokes and the Euler equations are presented.
During the fluid dynamics study, in order to obtain the forces on the aerofoil, several steady and unsteady simulations have been employed. These fluid dynamics computations are performed with the AER-Eu solver from the *Institute of Aerodynamics and Fluid Mechanics* of the *Technische Universität München*.
In this chapter the theory of the steady aerodynamics will be introduced, as well as the unsteady aerodynamics. The steady CFD solution is necessary as a starting point of the unsteady simulations.
One of the principal aims of this work is to reduce the computational cost of the CFD simulations building a reduced order model (ROM), which can well approximate the response of the model obtained by the CFD simulations. The design of a ROM can be built using different kinds of models. Section 2.4 describes several approaches to obtain a reduced model based on neural networks. In this section

two approaches of different neural networks used in this thesis and their respective drawbacks and benefits will be presented. Using a ROM, the unsteady simulations performed previously with the CFD, can be carried out with a lower computational effort.
Finally the non-linear aerodynamic of the ROM and a structural model are coupled in order to study the aeroelastic effects. Hence, the structural dynamics and especially the step that leads to the interaction between the aerodynamic and the structural part, i.e the generalized aerodynamic forces (GAF) obtained by the neural network, will be explained.
In the last section 2.5 will be introduced the aeroelasticity of an aircraft and the phenomena that described the non-linear aeroelasticity, like the limit cycle oscillations (LCO).

2.1 Fluid dynamics

The fundamental aspects of viscous flow are described by the Navier-Stokes equations, probably the most pivotal equations in theoretical fluid dynamics. However, as it is well known, the Navier-Stokes equations can be solved at a high computational cost, which is achieved with powerful computers. Furthermore, a specific CFD-grid is necessary, which takes time to be built well, because the wall boundary layer should be much better refined than a grid for the Euler equations. Therefore, various empirical models of turbulence have been developed so that solutions to the Navier-Stokes equations can be made computationally tractable.
The simplest form of aerodynamic modelling, the so-called *inviscid* flow, assumes that there are no effects from the viscosity of the air. This assumption implies that the flow passing an aerofoil, even on the surface, incurs no friction. In practice, viscosity does have an effect on the flow and this is most notably demonstrated by the presence of the boundary layer, where the flow slows down from the velocity in the free stream to zero velocity on the surface. Hence, omitting or neglecting the viscous terms, one obtains the Euler equations, which can be solved at a lower computational cost [1, 5].

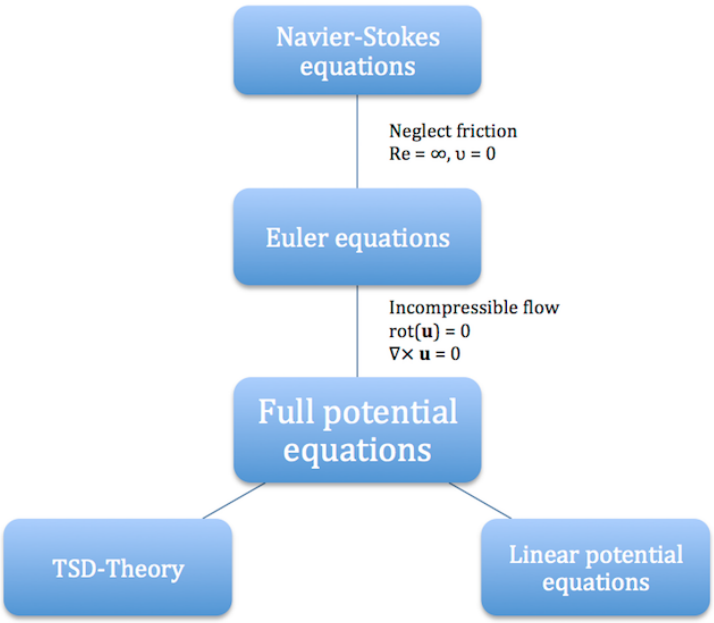

Figure 2.1: Fluid dynamics equations

A common simplification is to assume that the density of the air is constant (i.e. *incompressible*) throughout the flow, and this is valid for flows where $M < 0.3$ [17]. This simplification permits to treat the Euler equations with the potential flow theory, simplifying once more the set of equations. Beyond this Mach number, *compressibility* effects need to be taken into account and the density will vary through the flow field. Much of this work is realized using Mach numbers mostly in the transonic domain, so the potential flow theory will not be used.

2.1.1 Navier-Stokes and Euler equations

The Navier-Stokes system of equations, which describes the general viscous flow, can be written using the Einstein summation convention as follows [1]:

- Continuity equation:

$$\frac{\partial \rho}{\partial t} + \nabla \cdot (\rho \vec{u}) = 0 \tag{2.1}$$

- Momentum conservation equation:

$$\frac{\partial \rho u_i}{\partial t} + \frac{\partial \rho u_i u_j}{\partial x_j} = -\frac{\partial p}{\partial x_i} + \frac{\partial \tau_{ij}}{\partial x_j} + \rho f_i \quad with\ i = 1, 2, 3 \tag{2.2}$$

- Energy conservation equation:

$$\frac{\partial E}{\partial t} + \frac{(u_i E)}{\partial x_i} = -\frac{\partial (u_i p)}{\partial x_i} + \frac{\partial (u_i \tau_{ij})}{\partial x_j} + \rho f_i u_i - \frac{\partial q_i}{\partial x_i} \quad with\ i = 1, 2, 3 \tag{2.3}$$

To complete this set of equations, a further material independent equation is still needed. The air is considered as an ideal gas and therefore the state relation (Equation 2.4) is used, which binds the pressure p with the density ρ and the temperature T.

$$p = \rho R T \tag{2.4}$$

With these equations, turbulence, boundary layer effects as well as thermal transfer can be modeled. To reduce the computational costs, turbulence can be modeled with the Reynolds-Averaged Navier-Stokes (RANS) equations. They can be derived from the Navier-Stokes equations, replacing the velocity by the sum of an averaged term and a time-varying term. This yields new terms, which can be gathered in the Reynolds stress tensor [1, 37, 28].
The Euler equations can be derived from the Navier-Stokes equations. The following assumptions have to be made [5]:

- the fluid is inviscid $\tau_{ij} = 0$
- there is no bulk force $f_{b,i} = 0$
- there is no thermal transfer (adiabatic) $q_i = 0$

For these conditions, the governing equations are the *three-dimensional Euler equations* and may be expressed in strong conservation form as:

$$\frac{\partial \vec{q}}{\partial t} + \frac{\partial \vec{a_i}}{\partial x_i} \quad with \quad i = 1, 2, 3 \tag{2.5}$$

where

$$\vec{q} = \begin{bmatrix} \rho \\ \rho u_1 \\ \rho u_2 \\ \rho u_3 \\ E \end{bmatrix} \qquad \vec{a_1} = \begin{bmatrix} \rho u_1 \\ \rho u_1^2 + p \\ \rho u_1 u_2 \\ \rho u_1 u_3 \\ u_1(E+p) \end{bmatrix} \tag{2.6}$$

$$\vec{a_2} = \begin{bmatrix} \rho u_2 \\ \rho u_2 u_1 \\ \rho u_2^2 + p \\ \rho u_2 u_3 \\ u_2(E+p) \end{bmatrix} \qquad \vec{a_3} = \begin{bmatrix} \rho u_3 \\ \rho u_1 u_3 \\ \rho u_2 u_3 \\ \rho u_3^2 + p \\ u_3(E+p) \end{bmatrix}$$

And as for the Navier-Stokes equations, if a perfect gas is assumed, the necessary closing condition is given by the equation of state (equation 2.4). To ensure the generality of the solution it is practical to use non-dimensional quantities. The dimensionless parameters that characterize the unsteadiness of the problem are summarized below [9]:

- dimensionless time:

$$\tau^* = \frac{u_\infty t}{l_{ref}} = \frac{Ma_\infty \sqrt{k}}{l_{ref}} \sqrt{\frac{p_\infty}{\rho_\infty}} \cdot t \tag{2.7}$$

- reduced frequency:

$$k_{red} = \frac{l_{ref} \cdot \omega}{u_\infty} = \frac{l_{ref} \cdot 2\pi f}{u_\infty} = \frac{l_{ref}}{Ma_\infty \sqrt{k}} \sqrt{\frac{\rho_\infty}{p_\infty}} \cdot 2\pi f \tag{2.8}$$

2.1.2 Steady aerodynamics

Aircrafts are able to fly because the lift generated by the airflow over the wings and horizontal tail surfaces supports their weight. For a flexible aircraft, these lift

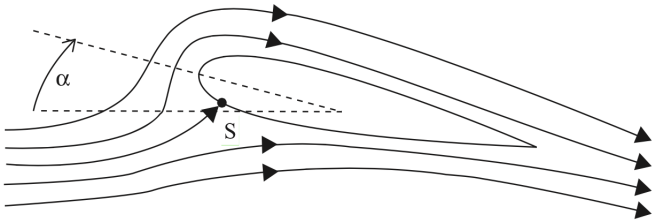

Figure 2.2: Flow around an aerofoil at a small angle of incidence [17]

forces give rise to deflections in the aerodynamic shape, which in turn change the characteristics of the airflow, hence leading to aeroelastic phenomena and affecting the dynamics loads, [17]. An understanding of how aerodynamic flows around an aerofoil or a surface during flight is very important in order to be able to develop mathematical models that describe the aeroelastic behaviour.

Only a brief introduction of steady aerodynamics will be exposed here.

From Anderson [1], a *steady* flow is a flow where the flow field is invariant with time.

Hence, in a flow field that follows the law of the steady aerodynamic in any point of the flow it is possible to continuously observe the same constant values for the pressure p, the density ρ, the vector of the velocity $\mathbf{V}$ and the temperature T.

More theoretical information is detailed in Anderson [1].

Figure 2.2 shows streamlines for an aerofoil at a small positive angle of incidence α. Lift occurs because the flow is deflected downwards by the aerofoil. This leads to a faster flow over the upper surface. This difference in speeds is due to the aerofoil shape. From Bernoulli's equations, see Anderson [1], for a velocity $V > V_\infty$ the pressure becomes $P < P_\infty$, so an increase in velocity leads to a suction in the flow field, whereas for a velocity $V < V_\infty$ the pressure becomes $P > P_\infty$ so a decrease in velocity leads to a compression in the flow field. Finally for a velocity $V = V_\infty$ the pressure remains $P = P_\infty$ and there is no change in the flow field.

It is common to describe the pressure distribution in terms of the non-dimensional

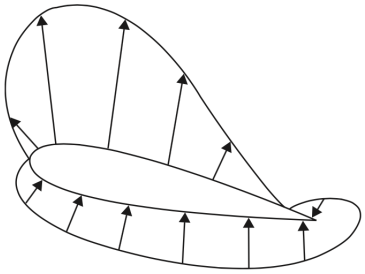

Figure 2.3: Typical pressure distribution for an aerofoil at a small angle of incidence [17]

pressure coefficient C_p, which is defined for a point in the flow as

$$C_p = \frac{P - P_\infty}{\frac{1}{2}\rho V_\infty^2} \tag{2.9}$$

which is the measure of the ratio of the local static pressure on the aerofoil to the free stream dynamic pressure. For clarity, the C_p distribution on a symmetric aerofoil at an angle of incidence below stall is plotted in Figure 2.3. It is common to present the pressure distribution on both surfaces in relation with the non-dimensional factor x/c, as shown in Figure 2.4, where the lift is dominated by suction on the upper surface due to the faster flow velocity on this surface [17].

The pressure distribution acting over the surface gives rise to a total force, whose resultant acts on a point of the chord called *centre of pressure*. During the flight condition the angle of incidence α changes, then the pressure distribution changes; this leads to a repositioning of the centre of pressure. This change leads to a difficulties due to the continual recalculation of the force and moments that act on the aerofoil [17]. For this reason, the net force is replaced by two resultant orthogonal forces (*lift* and *drag*) and a moment (*pitching moment*). It is usual to use coefficients which relate the above quantities to the dynamic pressure and chord for a unit span aerofoil (two-dimensional case), so the lift, drag and moment coefficients are defined as [1, 17]:

$$C_L = \frac{L}{\frac{1}{2}\rho V^2 c} \qquad (Lift) \tag{2.10}$$

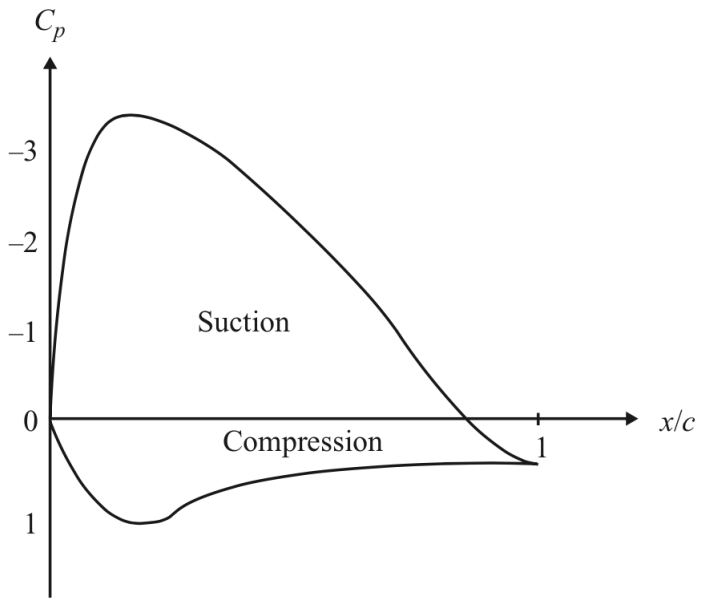

Figure 2.4: Pressure coefficient representation for a symmetric aerofoil [17]

$$C_D = \frac{D}{\frac{1}{2}\rho V^2 c} \qquad (Drag) \tag{2.11}$$

$$C_M = \frac{M}{\frac{1}{2}\rho V^2 c^2} \qquad (Pitching\ Moment) \tag{2.12}$$

where c is the aerofoil chord.

2.1.3 Unsteady aerodynamics

For flutter, manoeuvre and gust response analyses the behaviour of the aerodynamic flow field on the aerofoil surfaces under dynamic motion is required and it is necessary to include these effects upon the resulting forces and moments of the steady aerodynamics. These *unsteady* effects are an outcome of the changing

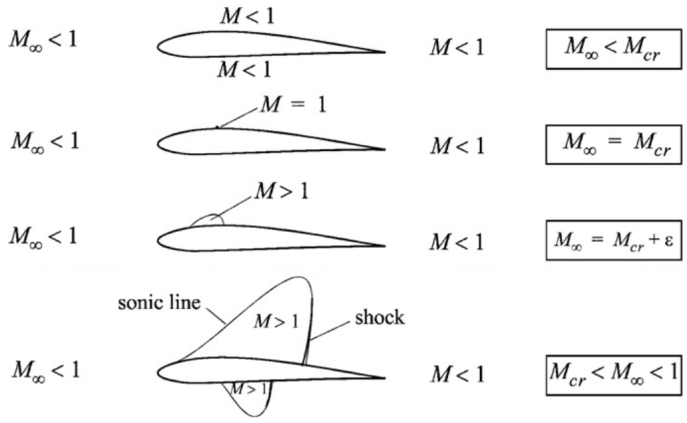

Figure 2.5: Flow patterns around aerofoils and wings in sub-transonic and transonic flows without boundary layer separation [28]

circulation and wake acting upon a moving aerofoil, and can have a considerable influence upon the resulting aerodynamic forces and moments [17].
By definition, see Anderson[1], an unsteady flow is a flow where the flow field variables, presented in section 2.1.2, at any given point are changing with time.
This work will focus particularly on the unsteady aerodynamic in the transonic flow, which is the crucial regime for the aeroelastic analysis.
A flow is considered transonic if both subsonic and supersonic regions exist near the body at the same time. For example, if an aircraft is flying at a subsonic speed ($M_\infty < 1$), local regions of supersonic flow will form on the wing surface if the flight Mach number is above the so-called critical Mach number M_{cr} for the wing. The critical Mach number depends on the shape, thickness, and attitude of the wing-body combination, but typically falls in the range $0.6 - 1.2$ for most aircraft under steady flight conditions such as cruise.
For more details see Bendiksen [28].
Transonic flutter of aircraft wings is dominated by the inherent nonlinearities in the unsteady transonic flow, resulting from moving shocks on the wing surface and from shock-boundary layer interactions. At transonic flight local regions of supersonic flow exist on and near the wing surface, as shown in Figure 2.5 and 2.6.
It can be seen how at the aft end of these regions, the flow is decelerated to sub-

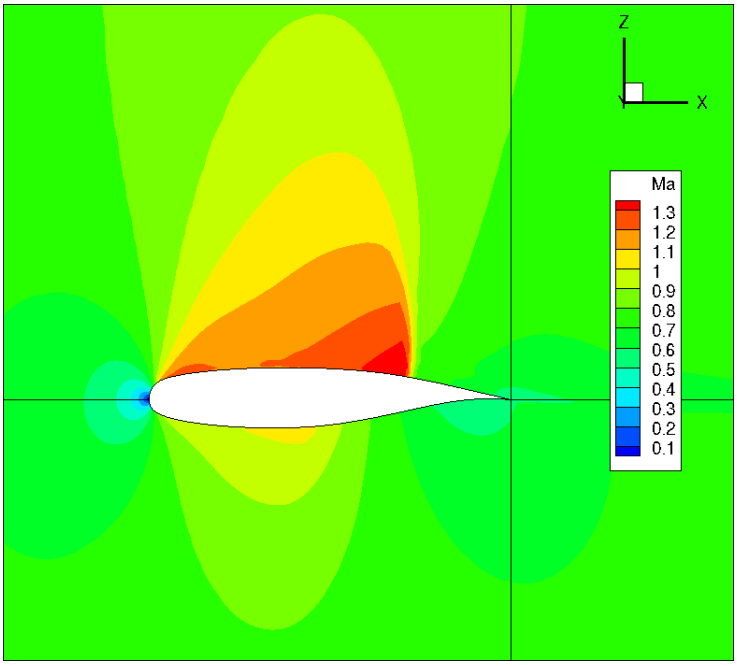

Figure 2.6: Steady Euler-CFD analysis of the NLR7301 supercritical aerofoil at $Ma_\infty = 0.753$ and an angle of attack $\alpha = 0.0$

sonic speeds through a nearly surface-normal shock wave. As the wing deforms in response to unsteady loads, the supersonic regions grow and shrink with the wing motion; thus, the shocks move along the wing surface, changing in intensity and position and possibly vanishing over part of the oscillation cycle. These moving shocks play an important role for the highly nonlinear aerodynamic behaviours observed in the transonic regime. In order to model an aeroelastic system with mixed subsonic-supersonic flow field with moving shocks, nonlinear field equations are required [28]. The modeling of unsteady transonic flow is shown in hierarchal order in Figure 2.7, based on the physical fidelity of the approximations involved. For flutter calculations, the general unsteady aerodynamic behaviour in the time domain is rarely used, since the motion at a single oscillation frequency is of more interest. For example, with an aerofoil oscillating in pitch at frequency ω, and applying the convolution approach using Wagner's function to obtain the lift time history, the effect of varying the frequency is shown in Figure 2.8. Compared to the quasi-steady lift values, there is a reduction in the magnitude of the lift and an

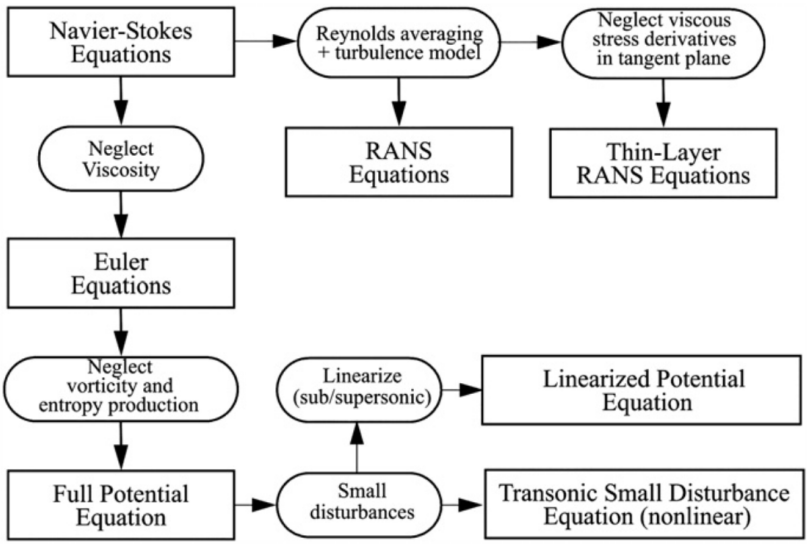

Figure 2.7: Unsteady aerodynamic modeling hierarchy in computational fluid dynamics and aeroelasticity [28]

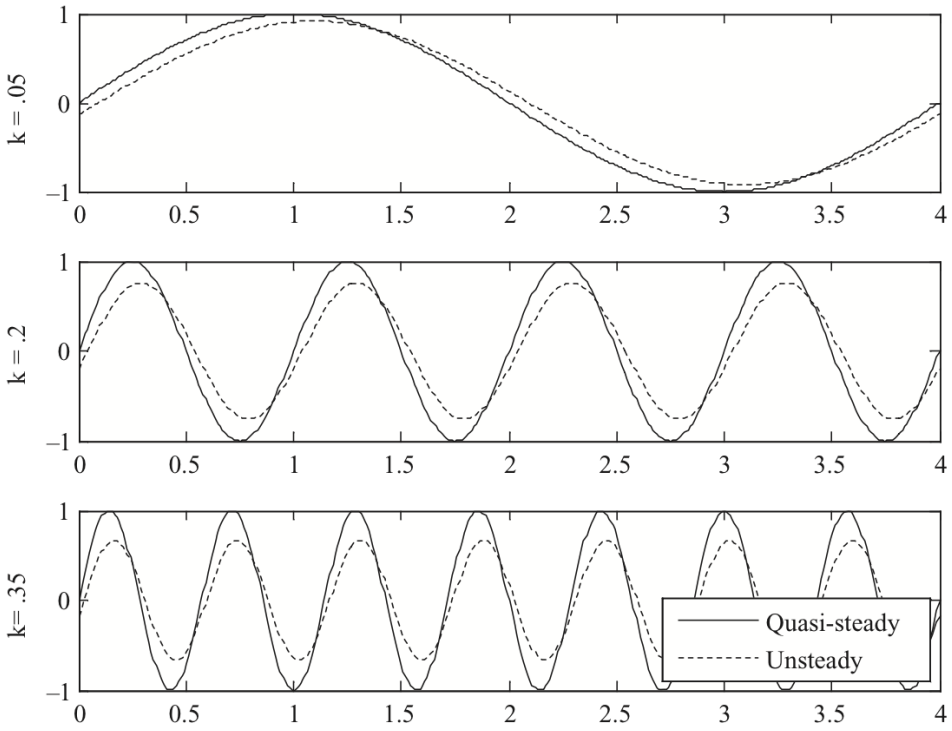

Figure 2.8: Unsteady lift for an oscillating aerofoil at different reduced frequencies [17]

introduction of a phase lag between the aerofoil motion and the unsteady forces. These two effects are a function of the dimensionless *frequency parameter* ν defined as

$$\nu = \frac{\omega c}{V} \tag{2.13}$$

which can be interpreted as the number of oscillations undergone by the aerofoil during the time taken for the airflow to travel across the chord of the aerofoil, multiplied by 2π. However, often the so-called *reduced frequency* k is used, equation 2.8.

2.1.4 CFD Solver

Unsteady transonic flow calculations are much more difficult than subsonic or supersonic flow calculations. First, the governing partial differential equations are nonlinear. Second, the flow field is of a mixed type, with embedded subsonic and supersonic regions. Third, the extent of the embedded supersonic or subsonic regions are *time-varying*, as are the moving shocks, and must be determined in a time-accurate manner as part of the solution.
The CFD-solver used in the current work is the AER-Eu solver from the *Institute of Aerodynamics and Fluid Mechanics* of the *Technische Universität München*, which will be discussed in the following. Since it is not the main subject of this work, the explanation will remain coincise (more informations in Kreiselmaier [9] and Fleischer [5]). The coordinate system and the grid used for the computation have to be adapted to the geometry of the wing or aerofoil. Indeed, the cartesian coordinate system would require interpolations on the structural boundaries to enforce the boundary conditions. Hence, the Euler or Navier-Stokes equations have to be transformed into curvilinear coordinates which are adapted to the geometry. The AER-Eu solver uses the finite volume method on the given grid, that offers the possibility to perform computations in the subsonic and supersonic domain, as well as in the transonic domain. In fact, the method assumes the field quantities to be concentrated in the kernel of each cell. This yields a conservative set of equations that allows to take shocks into account. The five partial equation are

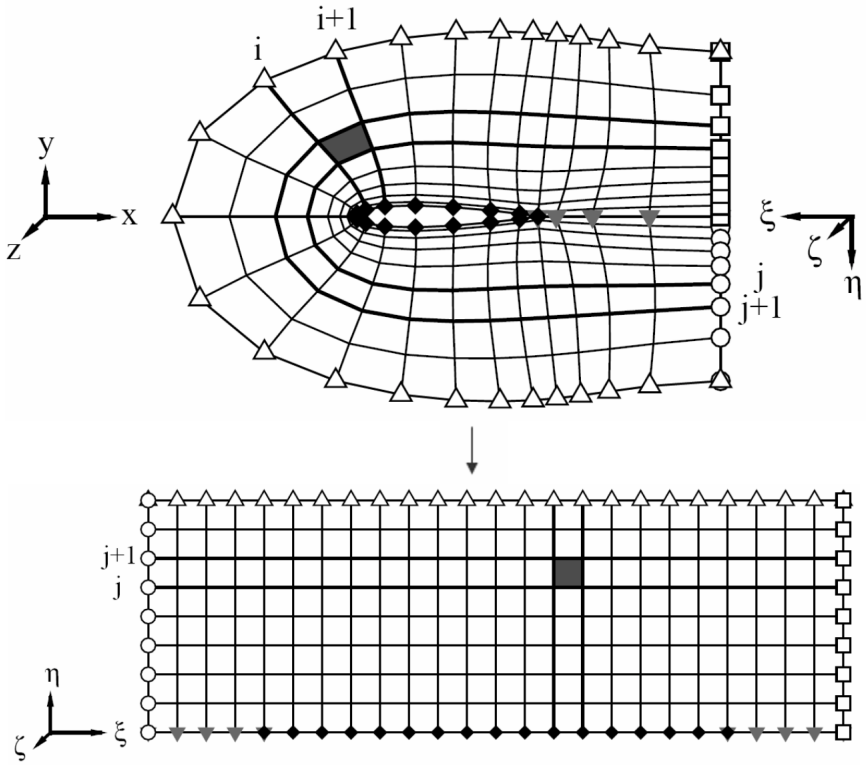

Figure 2.9: Representation of the adapted grid in the cartesian (x, y, z) and curvilinear (ξ, η, ζ) coordinate system [5]

Table 2.1: Advantages and drawbacks of implicit and explicit temporal integration schemes according to Fleischer [5]

Explicit time integration	**Implicit time integration**
easy to implement	time and resource consuming implementation
biggest time step limited by CFL-number	no time step limitation
tends to be unstable	good convergence and stability

solved approximately with the *flux difference splitting* method, under the assumption that the flux in one direction does not affect the flux in the other directions. Discontinuities at the interfaces and compression shocks are then accurately described. However, continuous transformations can in some cases be represented as expansion shocks, which breaks the entropy condition. Therefore, additional equations have been implemented in order to take the entropy changes caused by the shocks into account.

Another aspect of the numerical solver is the time discretization. For steady problems, pseudo-time will be iterated until a steady state is reached. For transient problems, one has to iterate over the real time in addition to the inner iterations over pseudo-time (dual time stepping).

Implicit and explicit temporal integration schemes are available in the CFD solver. Explicit temporal integration is realised with Runge-Kutta schemes and implicit temporal integration is based on the LU-SSOR scheme. Implicit and explicit schemes have both advantages and drawbacks, which are explained in Table 2.1. To reduce computational costs, only implicit schemes will be used for the CFD simulation here. In addition to the flow field equations and initial conditions, several boundary conditions have to be specified (*physical* boundary conditions like far-field velocity, no-slip condition, Euler wall condition and *numerical* boundary conditions like symmetry conditions, grid blocks, etc.).

2.2 Structural Dynamics

In the following section the structural model that will be coupled with the unsteady aerodynamic model for aeroelastic analysis will be outlined. Especially, the modal transformation of the structural model that leads to the state space form used subsequently in the fluid-structure interaction will be outlined.

2.2.1 Modal Transformation

In modern aeroelastic analysis, the structure of a flexible aircraft is usually discretized using the *Finite-Element method* (FEM). The initial finite-element model in physical space is often transferred into modal coordinates in order to reduce the degrees of freedom. The well-known equations of motion for a multi-modal structural system can be written as [17, 31]:

$$\boldsymbol{M}\ddot{\vec{y}} + \boldsymbol{D}\dot{\vec{y}} + \boldsymbol{K}\vec{y} = \vec{f} \tag{2.14}$$

where $\boldsymbol{M}$, $\boldsymbol{D}$ and $\boldsymbol{K}$ are the mass, damping and stiffness matrices of the structure, while $\vec{y}$ is the displacement field and $\vec{f}$ represents the external forces applied on the structure. Assuming a harmonic displacement field it can write the displacement, the velocity and the acceleration in a complexity notation as

$$\vec{y} = \vec{\Phi} exp(j\omega t) \tag{2.15}$$

$$\dot{\vec{y}} = j\omega\vec{\Phi} exp(j\omega t) \tag{2.16}$$

$$\ddot{\vec{y}} = -\omega^2\vec{\Phi} exp(j\omega t) \tag{2.17}$$

Hence eq. 2.14 can be written as

$$[-\omega^2\boldsymbol{M} + j\omega\boldsymbol{D} + \boldsymbol{K}]\vec{\Phi} = \vec{f} \tag{2.18}$$

The mass and stiffness matrices are yielded by the FEM analysis, whereas the damping matrix can be derived from experimental data or can be assumed as a linear combination of both mass and stiffness matrix, such as

$$\boldsymbol{C} = \alpha\boldsymbol{M} + \beta\boldsymbol{K} \tag{2.19}$$

where α and β are scalar coefficients.
However, for the modal analysis, only the free vibrations of the undamped structure are of interest, so the damping term as well as the external forces will be omitted. With these simplification the preceding equation becomes

$$[-\omega^2\boldsymbol{M} + \boldsymbol{K}]\vec{\Phi} = \vec{0} \tag{2.20}$$

so

$$\boldsymbol{K}\vec{\Phi} = \omega^2\boldsymbol{M}\vec{\Phi} \tag{2.21}$$

Equation 2.21 represents an eigenvalue problem, where ω is the so-called *undamped natural frequency* of the system and $\vec{\Phi}$ is the eigenvector. Both, $\boldsymbol{M}$ and $\boldsymbol{K}$ are positive symmetric matrices of ranks inferior to the number of degrees of freedom of the problem. For each degrees of freedom (DoF) there exists a set of n linear independent vectors $\vec{\Phi}_i$ and a set of scalars ω_i:

$$\boldsymbol{K}\vec{\Phi}_i = \omega_i^2\boldsymbol{M}\vec{\Phi}_i \tag{2.22}$$

$$\vec{\Phi}_{i'}^T\boldsymbol{K}\vec{\Phi}_i = \delta_{i'i}m_i\omega_i^2 \tag{2.23}$$

with the modal masses m_i, the Kronecker delta $\delta_{ii'}$ and $i, i' = 1, 2, ..., n$.
In practical applications, a number $n < n_{DOF}$ of eigenvectors are chosen [32], thus the displacement vector can be written as

$$\vec{y} = \sum_{i=1}^{n} \alpha_i(t)\vec{\Phi}_i \tag{2.24}$$

where α_i are the modal amplitudes, which can be gathered in the *modal vector* $\vec{q} = [\alpha_1, ..., \alpha_n]^T$. Substituting equation 2.24 in equation 2.14, neglecting the damping term, and pre-multiplying by $\vec{\Phi_{i'}^T}$ yields

$$m_i\ddot{\alpha}_i + m_i\omega_i\alpha_i = \vec{\Phi_{i'}}^T \vec{f} \qquad i = 1, ..., n \tag{2.25}$$

Now it has n independent single degrees of freedom equations. The number of the eigenvectors n remains relatively small in comparison to the number of degrees of freedom (DoF) of the initial model, but large enough to accurately depict the displacement of the structure. The so-called *modal matrix* is defined as the matrix having the mode shapes as columns:

$$\boldsymbol{\Phi} = [\vec{\Phi_1} \quad \vec{\Phi_2} \quad ... \quad \vec{\Phi_n}] \tag{2.26}$$

hence equation 2.24 reads as

$$\vec{y} = \boldsymbol{\Phi}\vec{q} \tag{2.27}$$

Now substituting $\vec{y}$ of equation 2.27 in equation 2.14 and pre-multiplying by the transponse of the modal matrix yields

$$\boldsymbol{\Phi}^T\boldsymbol{M}\boldsymbol{\Phi}\ddot{\vec{q}} + \boldsymbol{\Phi}^T\boldsymbol{K}\boldsymbol{\Phi}\vec{q} = \boldsymbol{\Phi}^T\vec{f} \tag{2.28}$$

or

$$\underline{\boldsymbol{M}}\ddot{\vec{q}} + \underline{\boldsymbol{K}}\vec{q} = \vec{f}_{gen} \tag{2.29}$$

where $\underline{\boldsymbol{M}}$ and $\underline{\boldsymbol{K}}$ are known as the *modal mass matrix* and the *modal stiffness matrix*. The generalized external forces (*modal force vector*) are the external forces transposed into the modal space $\vec{f}_{gen} = \boldsymbol{\Phi}^T\vec{f}$. The statement of orthogonality with respect to the mass matrix is expressed as $\underline{\boldsymbol{M}} = \boldsymbol{\Phi}^T\boldsymbol{M}\boldsymbol{\Phi} = \boldsymbol{I}_n$.
When the damping matrix $\boldsymbol{D}$ is known, equation 2.29 becomes

$$\underline{\boldsymbol{M}}\ddot{\vec{q}} + \underline{\boldsymbol{D}}\dot{\vec{q}} + \underline{\boldsymbol{K}}\vec{q} = \vec{f}_{gen} \tag{2.30}$$

where $\underline{\boldsymbol{D}} = \boldsymbol{\Phi}^T\boldsymbol{D}\boldsymbol{\Phi}$ is the *modal damping matrix*.
More detailed information about the structural dynamics can be found in Lot [32] or in Wright and Cooper [17].

2.2.2 State-Space Model

For numerical purposes, Equation 2.30 can be transformed into a first order vectorial differential equation. A state variable is defined as

$$\vec{x} = \begin{bmatrix} \vec{q} \\ \dot{\vec{q}} \end{bmatrix} \tag{2.31}$$

so the Equation 2.30 can be written, according to Zhang et al. [39], as

$$\dot{\vec{x}} = \underbrace{\begin{bmatrix} \mathbf{0}_n & \boldsymbol{I}_n \\ -\underline{\boldsymbol{M}}^{-1}\underline{\boldsymbol{K}} & -\underline{\boldsymbol{M}}^{-1}\underline{\boldsymbol{D}} \end{bmatrix}}_{\boldsymbol{A}} \vec{x} + \underbrace{\begin{bmatrix} \mathbf{0}_n \\ \boldsymbol{I}_n \end{bmatrix}}_{\boldsymbol{B}} \vec{f}_{gen} \tag{2.32}$$

This notation allows to implement easier numerical time integration models for coupling purpose.
Hence, the equation that denotes the state-space form is:

$$\dot{\vec{x}} = \boldsymbol{A}\vec{x} + \boldsymbol{B}\vec{u} \tag{2.33}$$

$$\dot{\vec{y}} = \boldsymbol{C}\vec{x} + \boldsymbol{D}\vec{u} \tag{2.34}$$

where $\vec{u}$ is the input vector, $\vec{y}$ the output vector and f_{gen} the generalized external forces vector.

2.3 Generalized Aerodynamic Forces (GAF)

Usually, to study the unsteady aerodynamic, there is a way to represent the aerodynamic forces applied to the structure ($\vec{f}_{gen,i}$). Considered only time domain formulation, an element of the generalized aerodynamic forces vector in relation to the i-th modal displacement can be written as

$$\vec{f}_{gen,i}(t) = q_\infty \cdot \int_S c_p(t) \cdot \vec{\Phi}_i d\vec{S} \tag{2.35}$$

where q_∞ is the dynamic pressure of the free stream, $d\vec{S}$ is a surface element, c_p the pressure coefficient and $\vec{\Phi}_i$ is the i-th modal vector.

2.4 Neural Network

Artificial neural networks were originally motivated by the biological structures in the brains of humans and animals, which are extremely powerful for such tasks as information processing, learning and adaptation. The most important characteristics of neural networks are [27]:

- large number of simple units
- highly parallel units
- strongly connected units
- robustness against the failure of single units
- learning from data

These properties make artificial neural networks well suited for fast hardware implementation.
The engineer's interest is to develop a universal tool for problem-solving inspired by the impressive examples of nature but without any pretension to model biological neural networks. For these reasons, neural networks are a possible method to derive the unsteady aerodynamic forces. In the case of the prediction of aerodynamic forces, a CFD computation with prescribed structural deformations has to be performed to yield the data to train the network.
In order to study the unsteady aerodynamic, several approaches with different neural networks (NNs) can be employed.
In the following section the differences and mechanism of the different NNs will be briefly introduced. But for more information see Nelles [27] and Haykin [34].

2.4.1 Radial Basis Function Networks (RBF)

The *radial basis function (RBF)* network utilizes a radial construction mechanism.
The construction of a radial basis function network, in its basis form, involves

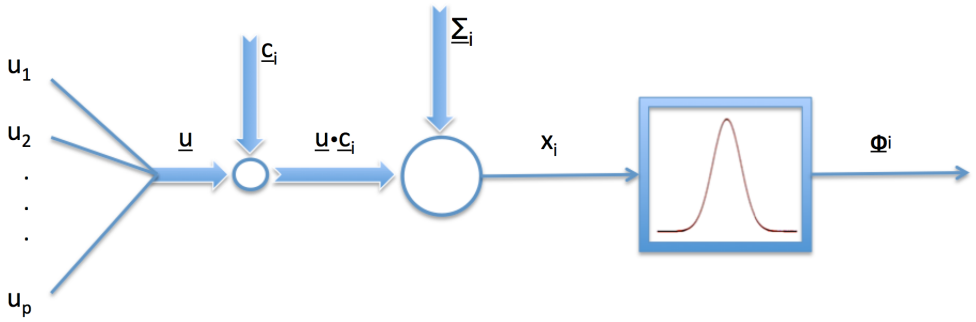

Figure 2.10: The i-th neuron of an RBF network

three layers with entirely different roles. The input layer is made up of source nodes (sensory units) that connect the network to its environment. The second layer, the hidden layer, applies a nonlinear transformation from the input space to the hidden space, which is of high dimensionality. A pattern-classification problem cast in a high-dimensional space is more likely to be linearly separable than in a low-dimensional space; hence, this is the reason for frequently making the dimension of the hidden space in a RBF high. Another point is the fact that the dimension of the hidden space is directly related to the capacity of the network to approximate a smooth input-output mapping; the higher the dimension of the hidden space, the more accurate the approximation will be, according to Niyogi [29].

In Figure 2.10 a neuron of a RBF network is shown.
The operation of a neuron can be split into two parts:

- The distance of the input vector $\underline{u} = [u_1, u_2, ..., u_p]^T$ to the center vector $\underline{c}_i = [c_{i1}, c_{i2}, ..., c_{ip}]^T$ with respect to the norm matrix $\underline{\sum}_i$ is calculated.

- The scalar distance x is transformed by the nonlinear activation function $g(x)$.

Figure 2.10 shows, for a Gaussian activation function, how the hidden layer parameters influence the basis function, where the typical Gaussian function can be

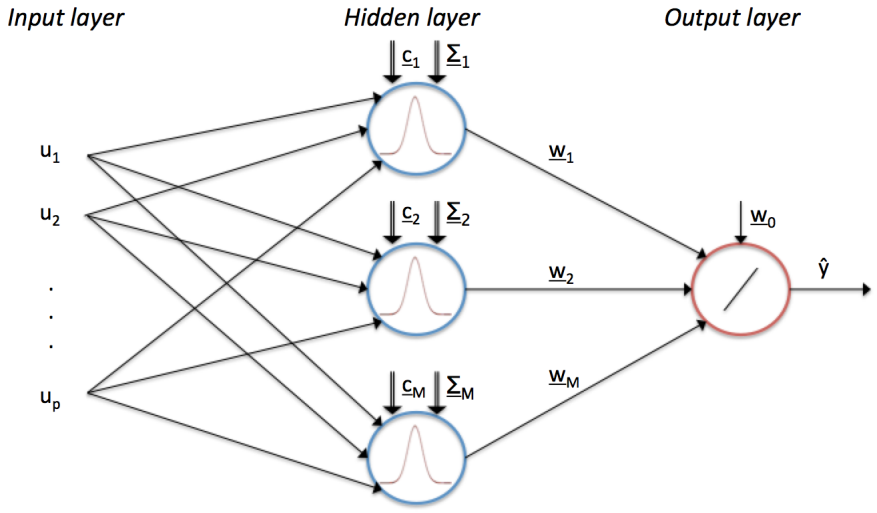

Figure 2.11: A radial basis function network. p is the number of inputs and M the number of hidden layer neurons

written as

$$g(x) = exp(-\frac{1}{2}x^2) \tag{2.36}$$

The distance x_i is calculated using the center $\underline{c}_i$ and norm matrix $\underline{\underline{\sum}}_i$, which are the hidden layer parameters of the i-th RBF neuron:

$$x_i = \|\underline{u} - \underline{c}_i\|_{\sum_i} = \sqrt{(\underline{u} - \underline{c}_i)^T \underline{\underline{\sum}}_i (\underline{u} - \underline{c}_i)} \tag{2.37}$$

The basis function of a Gaussian RBF network can be written as

$$\Phi_i(\underline{u}, \underline{\theta}_i^{(nl)}) = exp\Big(-\frac{1}{2}\|\underline{u} - \underline{c}_i\|^2_{\underline{\underline{\sum}}_i} \Big) \tag{2.38}$$

where the hidden layer parameter vector $\underline{\theta}_i^{(nl)}$ consists of the center vector coordinates and the entries of the norm matrix.
If several RBF neurons are used in parallel and are connected to an output neuron the radial basis function network is obtained, Figure 2.11. In basis function formulation the RBF network can be written as

$$\hat{y} = \sum_{i=0}^{M} w_i \Phi_i(\|\underline{u} - \underline{c}_i\|_{\underline{\underline{\sum}}_i}) \qquad with\ \Phi_0 = 1 \tag{2.39}$$

with the output layer weights w_i. Hence, the output $\hat{y}$ is a linear combination of M radial basis functions weighted by the w_i coefficients, where M is the number of hidden layer neurons. The centers are nonlinear parameters of the hidden layer neurons and determine the position of the basis functions. The standard deviations are nonlinear parameters of the hidden layer neurons and determine the widths and rotations of the basis functions.
During the training of the network the most suited parameters are optimized and selected. Different strategies can be used for training a RBF network. Most of these strategies determine the hidden layer parameters first, and subsequently the output layer weights are estimated by least squares approaches (RAWN). Alternatively, as it has been suggested by Chen [33], an orthogonal least squares algorithm (OLS)[1] can be applied. Thus, from the knowledge of input/output, the parameters of the network will be tuned or optimized, as far as the output predicted by the network is accurate in order to evaluate the solution carried out by the CFD. More information about the different training strategies are explained in Nelles [27].
The most important properties of RBF presented in Nelles [27] are:

- Interpolation behaviour tends to possess "dips" when the standard deviations of some RBFs are chosen too small.
- Extrapolation behaviour tends to zeros because the activation functions are typically local.
- Accuracy is typically medium because more neurons than the other NNs model are required for the same accuracy.
- Smoothness depends on the chosen activation function.
- Sensitivity to noise is low.
- Parameter optimization is fast.

[1]The approach based on the orthogonal least squares (OLS) algorithm is an efficient supervised learning approach for choosing the basis function centers.

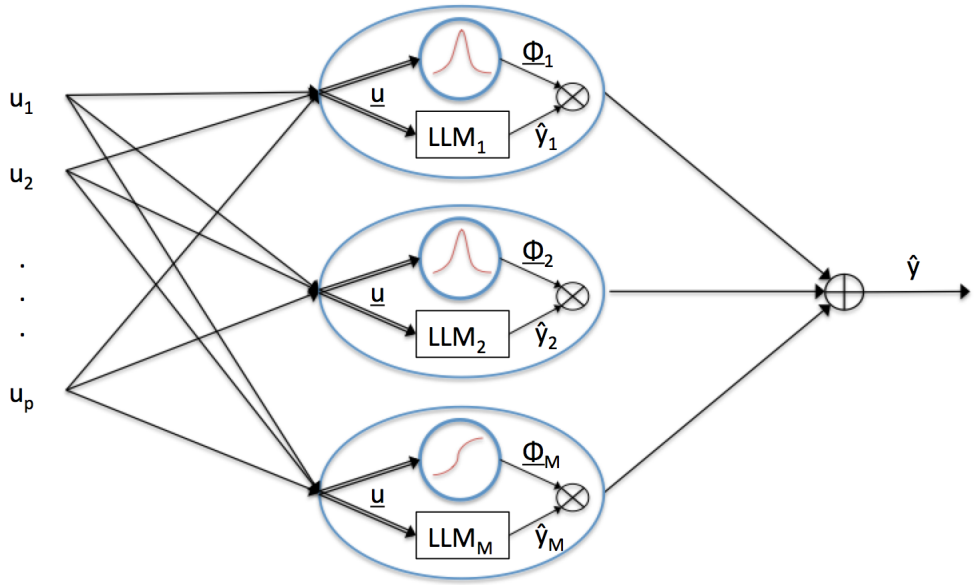

Figure 2.12: Local linear neuro-fuzzy model

- Training speed strictly depends on the training method used.
- Evaluation speed is medium because many neurons are required for a good accuracy.
- Incorporation of prior knowledge is possible because the parameters can be interpreted.

2.4.2 Local Linear Neuro-Fuzzy Models

"The local linear modeling approach is based on a divide and conquer strategy. A complex modeling problem is divided into a number of smaller and simpler subproblems, which are solved independently by identifying simple linear models", Nelles [27]. The most important behaviour for the success of the local linear approach is the division strategy of the original complex problem.
The network structure of a local linear neuro-fuzzy model is shown in Figure 2.12. Each neuron carries out two tasks. First, it realizes a local linear model (LLM) and second, it realizes an associated validity function that determines the region of va-

lidity of the LLM. In Figure 2.12, where the structure of the whole LLM is depicted, the different LLM associated to the hidden neurons M ($LLM_1, LLM_2, ..., LLM_M$) are represented.
Hence, the final outputs of the LLMs are:

$$\hat{y} = w_{i0} + w_{i1}u_1 + ... + w_{ip}u_p \tag{2.40}$$

where w_{ij} denote the LLM parameters for neuron i.
Any model input $\underline{u} = [u_1\ u_2\ ...\ u_p]^T$ is normalized by a validity function such that

$$\sum_{i=1}^{M} \Phi_i(u) = 1 \tag{2.41}$$

where M is the number of the neurons. This property is of fundamental relevance in order to interpret the Φ_i as validity functions because it ensures that the contributions of all local linear models sum up to 100%.
Considering equation 2.41 the output becomes

$$\hat{y} = \sum_{i=1}^{M} (w_{i0} + w_{i1}u_1 + ... + w_{ip}u_p)\Phi_i(\underline{u}) \tag{2.42}$$

From equation 2.42 the whole network output is calculated as a weighted sum of the single outputs of each local linear models. The validity functions are typically chosen as normalized Gaussians and depends on the center c_{ij} and the dimension of the individual standard deviations σ_{ij}. This validity functions are also called activation functions since they control the activity of the LLMs. One of the most important tasks is to choose the optimal standard deviation for the LLM model.
For example, the nonlinear function in Figure 2.13 is approximated by a network with four neurons, the same centers and different standard deviations. Small standard deviations lead to a non smooth network output, Figure 2.13 b). With a medium value for the standard deviation the smoothness of the model output is better, Figure 2.13 c). Instead, using high standard deviation, the validity function becomes wide and the maximum value decreases, Figure 2.13 d).
In this context, there are two special cases to consider [27]:

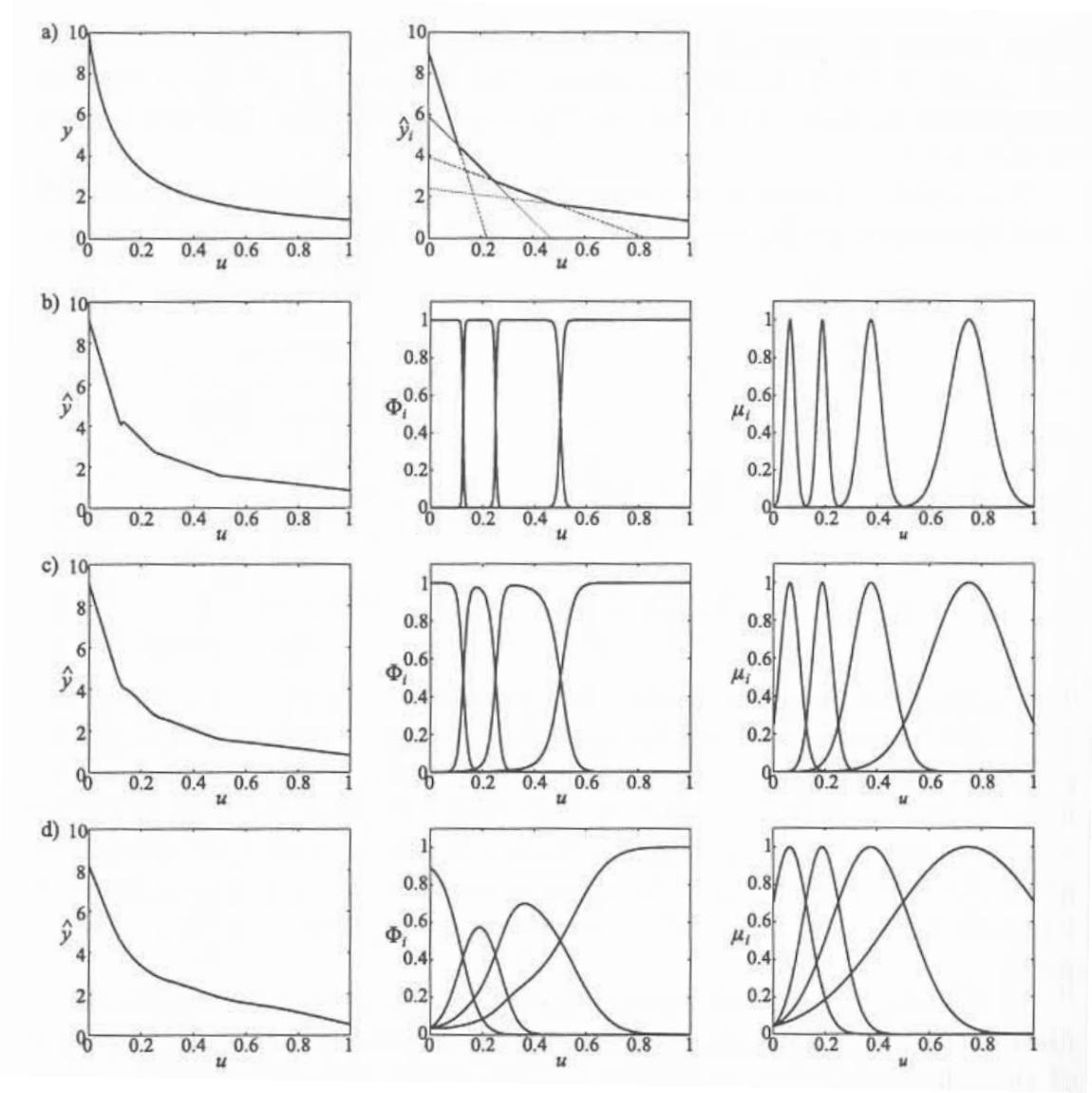

Figure 2.13: Local linear neuro-fuzzy model: a) function to be approximated and local linear models, b) small, c) medium, d) large standard deviation. [27]

- $\sigma \to 0$: as the standard deviation tends to zero, the validity function becomes step-like, Figure 2.13 b). In this case for any input only a single local linear model is active and this leads to a non smooth output.
- $\sigma \to \infty$: as the standard deviation tends to infinity, the validity functions become constant with an amplitude of $1/M$ and all the models are active for each input because the validity functions are too wide.

Obviously, a compromise must be found and it is strictly dependent on the specific case.

2.4.3 Local Linear Model Tree Algorithm (LOLIMOT)

"LOLIMOT is an incremental tree-construction algorithm that partitions the input space by axis-orthogonal splits" [27]. Each iteration increases the number of the sub-models by adding a new rule or local linear model to the old model, like an *incremental or growing algorithm* [27].
In each step of this growing algorithm there are two main tasks:

- The validity function belonging to the considered partitioning of the input space is computed.
- A local weighted least squares technique optimizes the rule corresponding to the i-th step.

In each iteration the validity functions that correspond to the actual partitioning of the input space are computed, as in Figure 2.14, and the corresponding rules consequents are optimized by a local weighted least square technique. The proportionality factor between the rectangles' extension and the standard deviations is a fixed parameter, that has to be selected by the user. There is not a fixed optimal value, but the common value in use is [27]:

$$k_\sigma = \frac{1}{3} \tag{2.43}$$

In the LOLIMOT algorithm the standard deviations are calculated as follows:

$$\sigma_{ij} = k_\sigma \cdot \Delta_{ij} \tag{2.44}$$

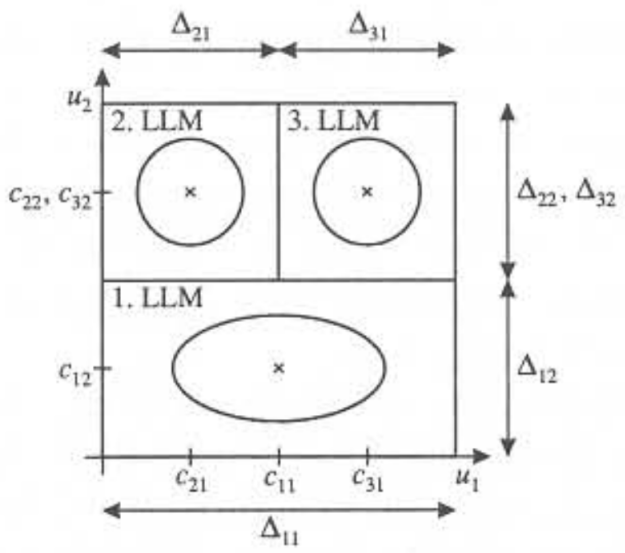

Figure 2.14: Sub-division of the LOLIMOT model and the respective extension of the hyperrectangle Δ_{ij} [27]

where Δ_{ij} denotes the extension of the hyperrectangle of local model i in dimension u_j, as in Figure 2.14.

LOLIMOT Algorithm. The algorithm consists of an outer and inner loop split in four main steps [27]:

1. *Initial model:* Construct the validity function for the initially given input space and use the local weighted least square algorithm to estimate the LLM parameters.

2. *Find the worst LLM:* The worst Local Linear Model is defined according to local loss function, $\max(I_i)$:

$$I_i = \sum_{j=1}^{N} e^2(j)\Phi_i(\underline{u}(j)) \tag{2.45}$$

   This LLM is selected to be refined.

3. *Check and construct all divisions:* The hyperrectangle of the worst LLM is split into two halves with the axis-orthogonal split in all dimensions. For each

division some several steps are carried out, like construction of the multidimensional membership functions (MSFs) for the hyperrectangle, construction of a validity function, local estimation of the parameters for the new LLM and calculation of the loss function for the overall model considered after the division.

4. *Find the best division:* Finally, the best division for the new neuron have to be find from the previous step and must be added in order to increment the number of LLMs.

In step 3 a fundamental task has been spoken about: the *local estimation* of the parameters. The idea behind the local estimation is to consider the optimization of the parameters relative to the specific iteration as an individual problem. Hence, the parameters for the new local linear model generated by the algorithm are estimated *separately*. The major advantage of local estimation is its low computational complexity and regularization effect.
From Nelles [27], local estimation seems to be superior to global estimation in terms of:

- *Fast training*
- *Regularization effect*
- *Higher flexibility*

The overall local model quality depends on the training data distribution. The complexity of LOLIMOT grows linearly with the number of neurons. Figure 2.15 illustrates the first five iterations of the LOLIMOT algorithm for a two-dimensional input space (p = 2), whereas Figure 2.16 illustrates an example of the LOLIMOT approximation in the first seven iterations. It's possible to see how increasingly the iterations, and hence the number of the sub-models, improve the function approximation.
So far, the only parameter that has to be chosen by the user before starting LOLIMOT is the smoothness k_σ of the model. It is very important to understand the influence of this parameter on the model quality. To explain the changes in

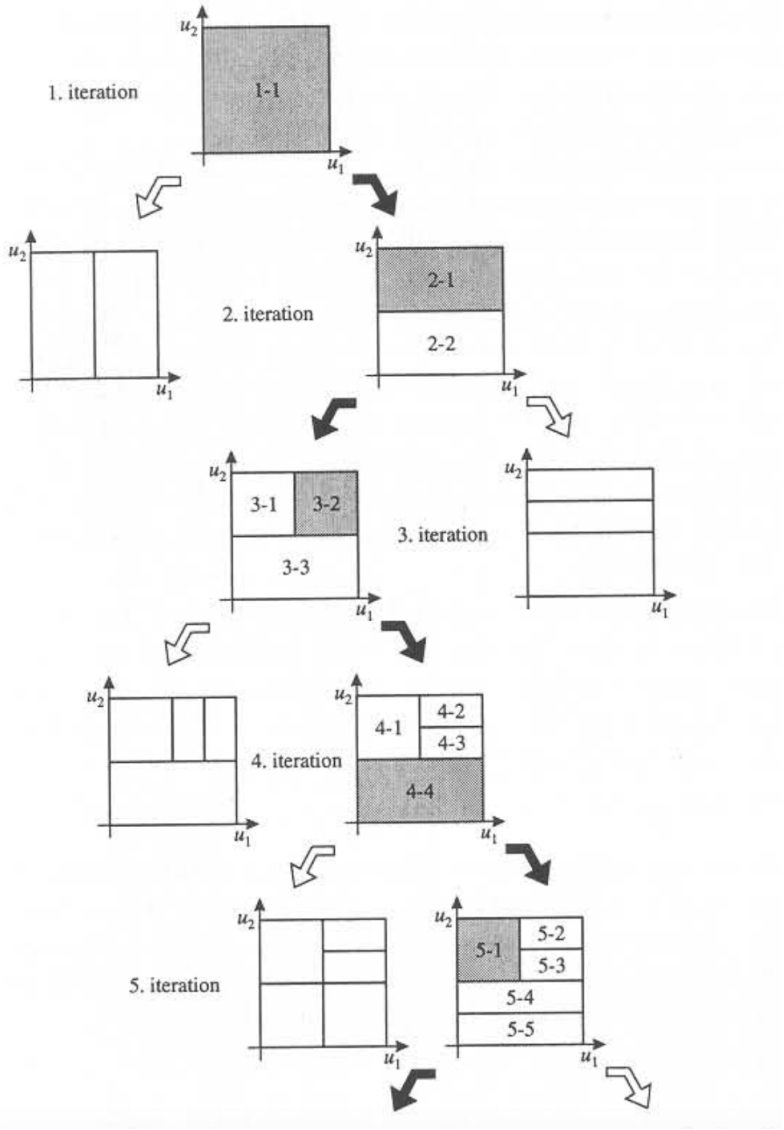

Figure 2.15: Operation of the LOLIMOT algorithm in the first five iterations for a two-dimensional input space (p = 2) [27]

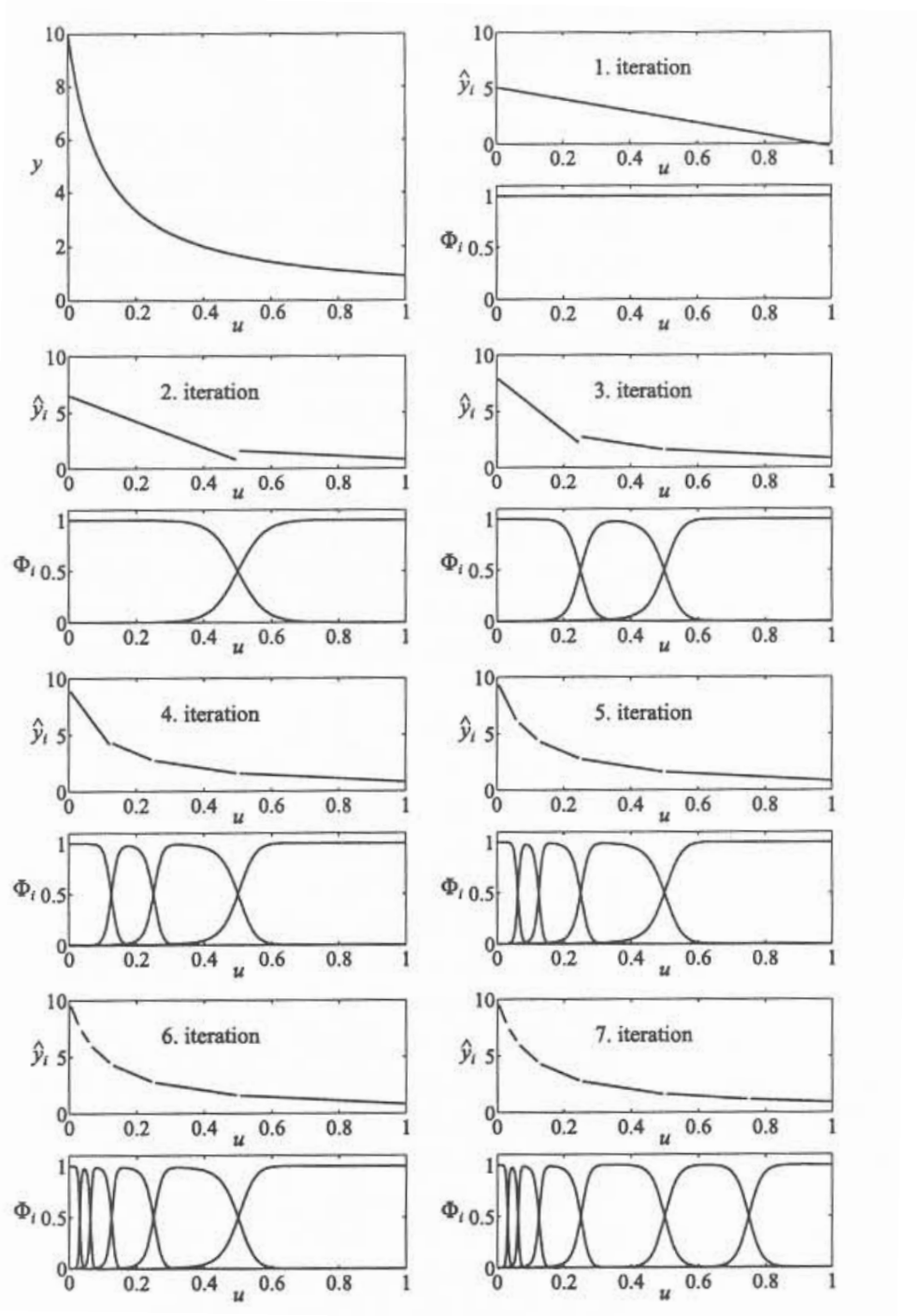

Figure 2.16: Example of the first seven LOLIMOT iterations for one-dimensional function approximation. [27]

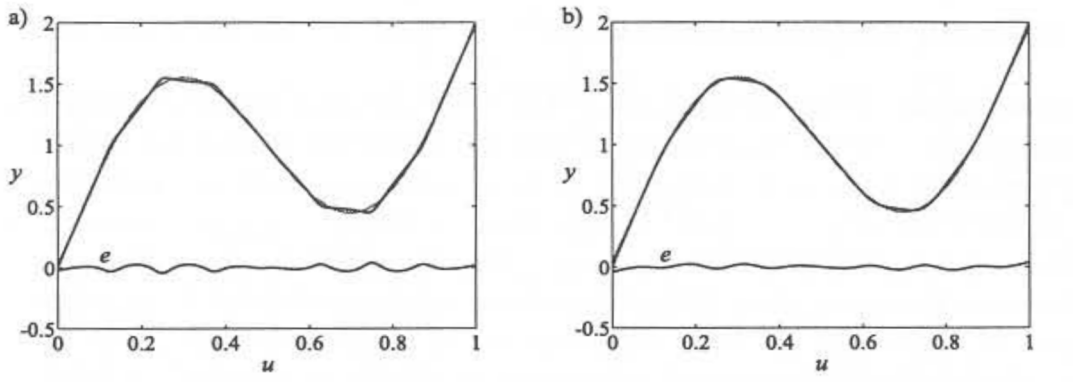

Figure 2.17: Smoothness optimization: a) before optimization, b) after optimization. [27]

the approximation made by a different choice of the smoothness parameter we can take an example from Nelles [27]. Figure 2.17 shows the approximation of a sine function obtained by the LOLIMOT algorithm with $M = 8$ iterations and the better quality for an approximation obtained after the optimization of k_σ. As for equation 2.43, the smoothness parameter was chosen a priori as $k_\sigma = 1/3$. A subsequent nonlinear optimization of k_σ yields the optimal smoothness parameter $k_\sigma^{(opt)} = 0.53$. This kind of optimization requires higher computational effort. Hence, usually it is more efficient to accept slightly more rules and avoid the nonlinear optimization of k_σ. Of course, this tradeoff between model complexity and training time is problem dependent.

2.4.4 Non-Linear System Identification

A fundamental task of the reduced order model (ROM) is the modeling of *dynamic system*, since an unsteady flow with a large amplitude of shock wave motion or flow separation is a typical nonlinear dynamic system. In such a case the network should be able to learn the evolution path of a general system from the input-output data. This kind of memory is obtained through a *delay* applied to the hidden neurons. The network process the input together with the input delays and the output delays. Hence, the input layer is now composed by a set

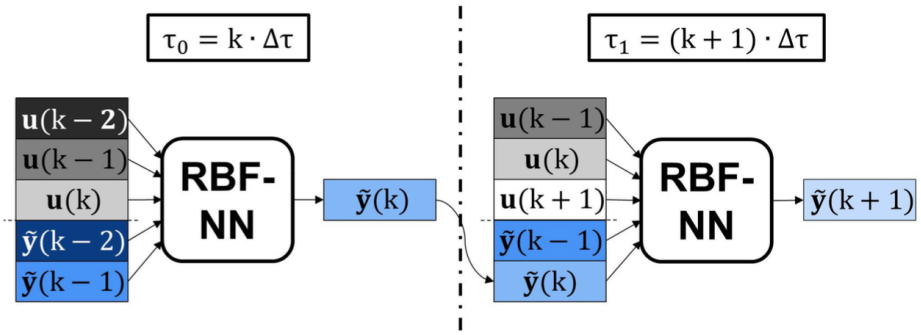

Figure 2.18: Example of a single-input single-output model with a delay-order of two for a RBF-NN, Winter and Breitsamter [23]

of input data and a set of delayed output and input from the hidden neurons. A fully connected recurrent neural network feedbacks all the neurons output of an hypothetical step i-th to the input layer of the step $i+1$, as in Figure 2.18, whereas a partially connected recurrent neural network feedbacks only a fraction of this neurons outputs. The number of the maximum delayed input-output samples must be chosen by the user, but the effective number of the delays changes in each time step and depends on the network optimization. The scheme of a recursive RBF neural network is shown in Figure 2.18 and its corresponding function can be written, according to [39], as

$$\{\hat{y}_k\}^T = f(\underline{u}_{k-1}, \underline{u}_{k-2}, ..., \underline{u}_{k-m}, \hat{y}_{k-1}, \hat{y}_{k-2}, ..., \hat{y}_{k-n}) \tag{2.46}$$

where f is a nonlinear function, $\underline{u}$ is the vector of the system inputs (generalized structural coordinate vector), and $\hat{y}$ is the vector of the system outputs (generalized aerodynamic force vector). m and n are respectively the delay orders of the input and the output that are determined by the user.

The use of the delay in the model leads to some drawbacks according to Winter [22]:

- The use of the delayed input-output can lead to a failure accumulation and an instability of the system.
- This method depends strictly on the quality of the training data and the training process.

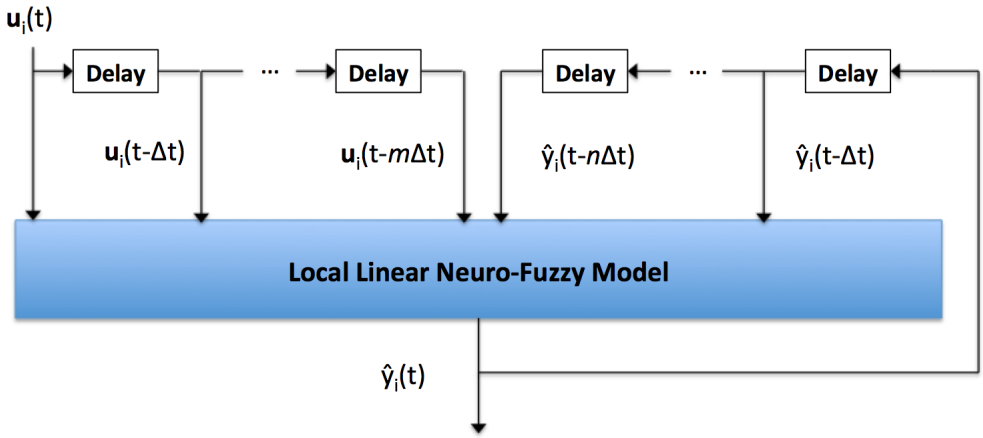

Figure 2.19: Non-linear system approach scheme for a local linear-neuro fuzzy model

- The time step for application of NN must be the same used in the training data.

This section is only an introduction to the approaches to evaluate the non-linear system. A recurrent neural network with RBF is only one of the different approaches that can be used. This recurrent RBF can be interpreted as a nonlinear version of the AutoRegressive model with eXogenous input (ARX) identification technique, and can be also defined as Nonlinear AutoRegressive model with eXogenous input (NARX).
Figure 2.19 summarizes the mechanism adopted by a local linear neuro-fuzzy model, like the LOLIMOT, to evaluate a non-linear system using m dynamic delay-orders for the inputs and n delay-orders for the output.
The selection of the delay-orders and the respective results will be explained in chapter 5.
More information can be found in Haykin [34] and Nelles [27].

2.5 Non-linear Aeroelasticity

Aeroelasticity is the science that concerns the interaction of aerodynamic, elastic and inertial forces. Static or linear aeroelasticity effects result from the interaction between aerodynamic and inertial forces, whereas dynamic or nonlinear aeroelastic effects occur by the interaction of all the three forces.
The most important aeroelastic phenomena, as flutter and divergence, can potentially lead to structural failure. In order to ensure the structural integrity, aircraft structural designs have to be made heavier (the so-called aeroelastic penalty), [38].
Non-linear effects can appear through aerodynamic, structural or control system mechanisms. In the transonic regime, aerodynamic nonlinearity can occur due to the movement of shockwaves on the aerofoil surface. Structural non-linearity depends on the cubic stiffness, such as interaction of engine pylon and wing interface or freeplay caused by the flap/wing interaction. Control systems are also causes of aeroelastic non-linearities due to the non-linear control laws [16, 25].
This work will focus only on the nonlinear aerodynamic phenomena, like Limit Cycle Oscillations (LCOs).
In this field previous studies have pointed out some important characteristics of the transonic flutter phenomena [35]:

- Transonic dip
- Limit cycle oscillations (LCO)

Figure 2.20 shows a typical plot of the flutter speed versus Mach number, and it can be seen that in the transonic region there is a dramatic reduction in the flutter speed. The area of this plot where the Mach number leads to a drastic reduction of the flutter velocity is called transonic "dip".
Limit cycle oscillations are a peculiar phenomenon encountered only in the analysis of nonlinear dynamic systems and are related to flutter phenomena. Indeed, flutter is considered to be a violent unstable vibration, whereas LCO can be described as a bounded flutter.
LCOs can be associated to the formation of large vortical flow structures, as in the

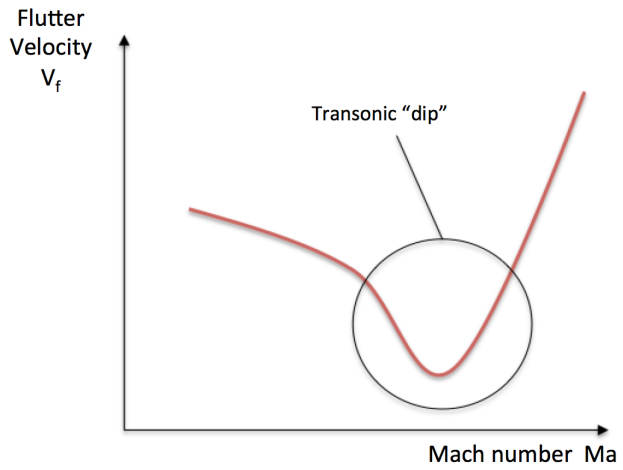

Figure 2.20: Example of transonic dip related to the flutter velocity and the Mach number

case of low speed and high angle of attack flow regime or associated with moving shocks in the transonic regime.

One of the advantages of studying theoretical models is that each of the several possible physical phenomena that lead to LCO can be studied separately. Considering only the effects of an inviscid flow, as the Euler model used in this work, the principal effects of interest is the relatively large motion of the shock wave as the amplitude of the pitch motion of the aerofoil becomes sufficiently large. This motion leads to a movement of the center of pressure with the amplitude that may lead to LCO rather than the catastrophic exponentially growing oscillations predicted by time linearized aerodynamic models. For dynamically non-linear aerodynamic models it is different, because these allow larger and more general shock motions, including the appearance and disappearance of shocks during a cycle of aerofoil motion [25, 16, 17, 7, 24].

A limit cycle oscillation is characterized by sustained periodic oscillations that neither increase nor decrease in amplitude along the time for a given flight condition, see Figure 2.21. The high frequency and large amplitude motion of an LCO can lead to the loss of the structural integrity in different parts of the aircraft and can lead to a damage caused by the fatigue accumulated. Therefore, the prediction of this kind of non-linearity is of fundamental importance during the design of a

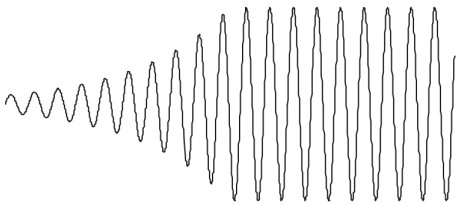

Figure 2.21: Example of limit cycle oscillations (LCO) [17]

modern aircraft [25, 17].

There are some examples of documented LCOs occurring on full-size aircraft. On the F-16 and F-18 fighter aircraft, LCOs have been observed for a wide range of different store combinations, i.e. missiles, [25, 4, 30].

The undamped and large-amplitude oscillations lead to a reduction in the fatigue life of certain components and hence can cause an early substitution of the component or a more frequent inspection. Both possible solutions add additional costs to the aircraft maintenance. Furthermore, when the stores under the LCOs motion are missiles or other weapons, it is possible to have the lock of the weapons or the separation from the wing of the fighter aircraft. Finally, the LCOs can lead to unwanted effects to the pilot, insofar the workload increases as well as the level of the fatigue and stress of the pilot himself.

Chapter 3

Training and Validation Signals

In this chapter the signals used during the unsteady analysis (AER-Eu simulation and ROM simulation) will be discussed. In this context the fundamental importance of the training signal, which has to be built to lead to an efficient trained model, will be explained. The training process is a key point of the work, which influences the response of the reduced order model and the behaviour of the LCOs during the aeroelastic simulation. Subsequently, the signals that have been employed to validate the reduced order model are considered. The validation phase will be used to verify the quality of the ROMs obtained using the different training signals.

3.1 Training Signal for Identification Task

The input training signal is the only datum that can play an important role in system identification, because it is the only possibility to build a trained system that can well approximate the response of the model.
In the *linear* system identification, the training signal must posses different characteristics [27]:

- The signal range must be fixed between a minimum and a maximum value
- The measurement time is always limited

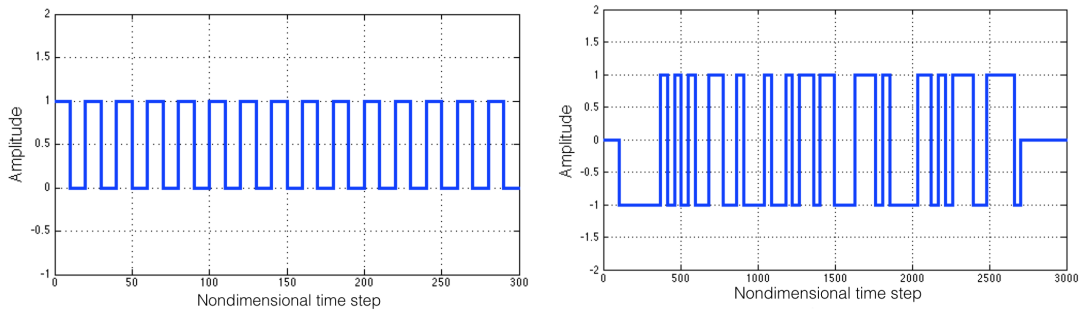

(a) Step signal (b) PRBS signal

Figure 3.1: Example of training signals for *linear* system identification

For the design of the input signal the purpose of the model is relevant and leads to a specific training signal with specific properties.

In *linear* system identification the signals used for training the model have the same amplitude and often the same frequency. These two properties have to be chosen in order to satisfy the purpose of the considered model. An example of training signals for linear system identification is shown in Figure 3.1. Figure 3.1(a) depicts a step series signal with a fixed amplitude and frequency, called *rectangular* signal, according to [27]. In Figure 3.1(b) a *pseudo random binary signal* (PRBS) is showed, which imitates white noise in discrete time with a deterministic signal, according to [27] and [42]. For example, in the aerodynamic field, this kind of signals can be chosen as identification signals for steady aerodynamic analysis.

Instead, the design of the training signal for the identification of a *non-linear* system is more decisive than for linear models because the non-linear dynamic models are significantly more complex and the data require more information [27]. In many practical situations, saving computational time is of extreme importance; hence, the training signal must not contain too much information to identify a black box model that is capable of describing the system in all situations. This underlines the importance of the prior knowledge in order to select only the relevant information for the training data.

Therefore, for a black box modeling the training signal is the most relevant source of information. If the signal does not excite all the frequencies and amplitudes of

interest, the response of the resulting ROM will not be capable of approximating the response as a full order model that used the CFD. Thus, the design of the training signal is a key step in the construction of a ROM. Independently of the chosen model architecture, the quality of the signal determines an upper bound on the accuracy achieved by the model. According to Nelles [27] the main issues that influence the design of the excitation signal are:

- *Purpose of modeling*: the purpose of the modeling should be specified. For example, a model utilized for the steady aerodynamic analysis must have a training signal with some constant values, or a model utilized for the control should be most accurate near the crossover frequency. Instead, in this work, the only behaviour of interest is the nonlinear aerodynamic effects. Hence, the input signal can be completely unsteady, without constant parts.

- *Maximum length of the training data set*: the length of the signal could be very high. However, the length should be a tradeoff between the number of information contained in the training data and the computational effort. The length of the signal must contain the appropriate number of information to allow a good interpretation of the system.

- *Range of input signal*: the signal should be built using all the operating properties that might occur in real operations. It is important that the data covers the limits of the input range because model extrapolation is much more inaccurate than interpolation.

An improvement in the CFD unsteady aerodynamic analysis is to involve simultaneous excitation of the structural modes of the system. Thus allows the computation of the unsteady aerodynamic state-space model using a single CFD execution, independently of the number of structural modes.
In the situation where the goal is the simultaneous excitation of a multiple-input multiple-output (MIMO) system, system identification techniques dictate that the nature of the input functions used to excite the system must be properly defined. Another important point to keep in mind when defining these input functions is that these functions need to be different, in some sense, from each other. This

makes sense since, if the excitation inputs are identical and they are applied simultaneously, it becomes practically impossible for any system identification algorithm to relate the effects of one input on a given output. With respect to unsteady aerodynamic MIMO system, these individual impulse responses correspond to time-domain generalized aerodynamic forces (GAF) [41].
Following the guidelines presented previously three signals have been considered for non-linear system identification:

- Amplitude-modulated pseudo-random binary signal (APRBS)
- Sinusoidal input with random amplitude and frequency
- Totally random signal

To build these signals, in aeroelasticity, the reduced frequency k_{red}, equation 2.8 is widely used, which is a non-dimensional frequency. Hence, the time domain frequencies of interest have been turned into the reduced frequencies in order to design a signal based on k_{red}. For the design of the input signal a frequency analysis based on the Power Spectral Density (PSD) has been used. The power spectrum of a signal describes how the variance of the data is distributed over the frequency components [32]. The spectrum helps to decompose the content of the signal into the different frequencies present in that process.
Furthermore, the ROM simulation works using a non-dimensional time step, which is defined by:

$$\Delta\tau = M_\infty \cdot \sqrt{k} \cdot \sqrt{\frac{p_\infty}{\rho_\infty}} \cdot \Delta t \tag{3.1}$$

where M_∞ is the Mach number, k is the isentropic coefficient, p_∞ and ρ_∞ are the pressure and density of the free-stream and Δt is the physical time step in the time domain.

3.1.1 Amplitude-Modulated Pseudo-Random Binary Signal (APRBS)

The *amplitude-modulated pseudo-random binary signal* (APRBS) is an extension of the PRBS signal. The PRBS is inappropriate for non-linear systems because there is no information about the system behaviour for the input amplitudes besides the two values of the range chosen, for example -1 and 1 for the PRBS in Figure 3.1(b). A possible solution is to extend the PRBS to different amplitudes, giving to each step of the PRBS a different random amplitude chosen from a range imposed by the user. Finally, the frequency is influenced by the hold time of each step throughout the signal. For this reason the minimum hold time must to be set by the user in order to excite the chosen range of frequency. The main advantage using the APRBS in relation to the PRBS is the large spectrum of excited frequencies and amplitudes. The APRBS employed in this work for identification task is represented in Figure 3.2 with its respective PSD.

3.1.2 Random Sinusoidal Signal (RSS)

The *random sinusoidal signal* is generated by a series of sinusoidal waves, which randomly change amplitude and frequency each period. The frequency is chosen from a range specified by the user and the amplitude in the range of interest for the specific case. In this work a range of amplitude of -1.05 and 1.05 is employed for the current signal in order to approximate a test signal with an amplitude range between -1 and 1. If a range of -1 and 1 for the training signal had been chosen, probably the maximum amplitude would be less than 1. This is why the selected range of the amplitude is bigger than 1. When the frequency has been chosen from the specified range, it is held constant for one period. Then the frequency is chosen again and the process continues. With this kind of signal most of the frequencies and amplitudes of interest should be excited. Figure 3.3 depicts this kind of signal and the respective PSD. In this case the reduced frequency is chosen in a range between 0.1 and 0.5. This choice will be explained in chapter 5.

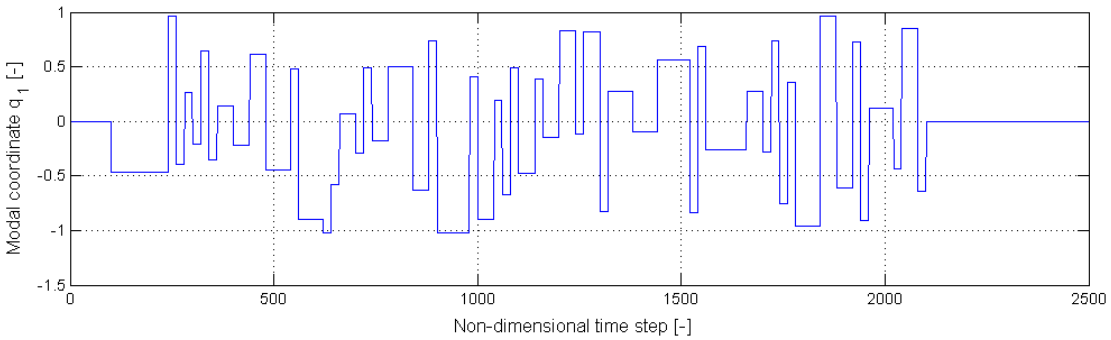

(a) APRBS in non-dimensional time domain

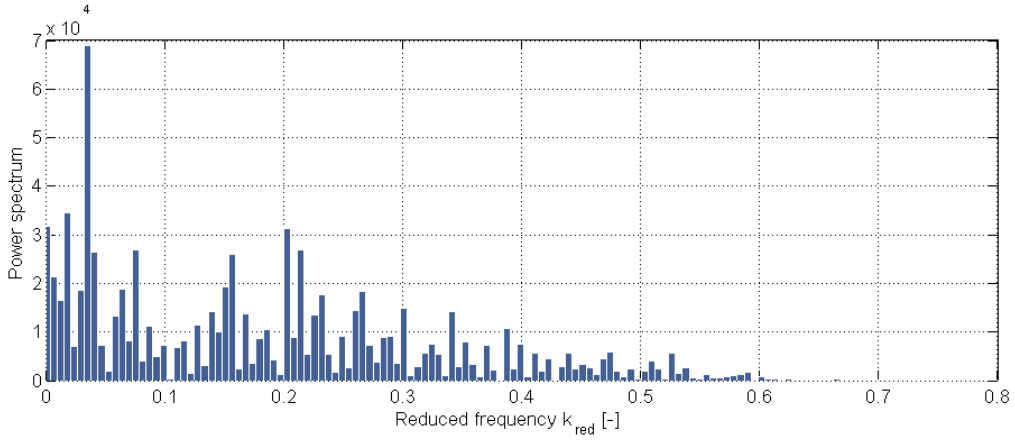

(b) APRBS signal PSD

Figure 3.2: APRBS signal for the first mode used for non-linear system identification

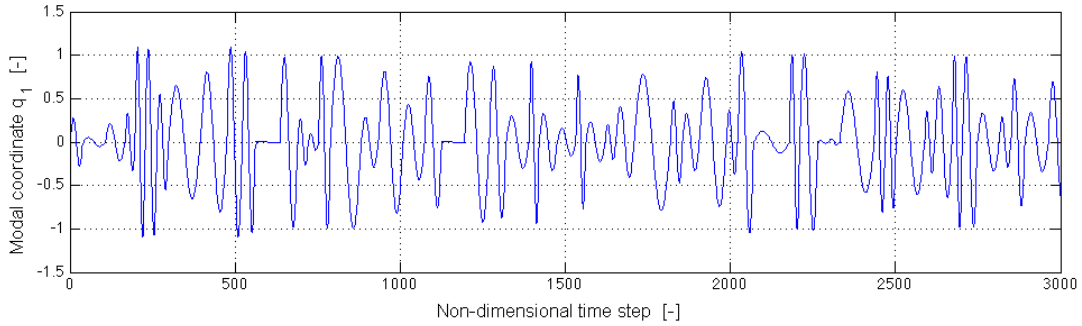

(a) Sinusoidal signal with randomly amplitudes and frequencies in the non-dimensional time domain

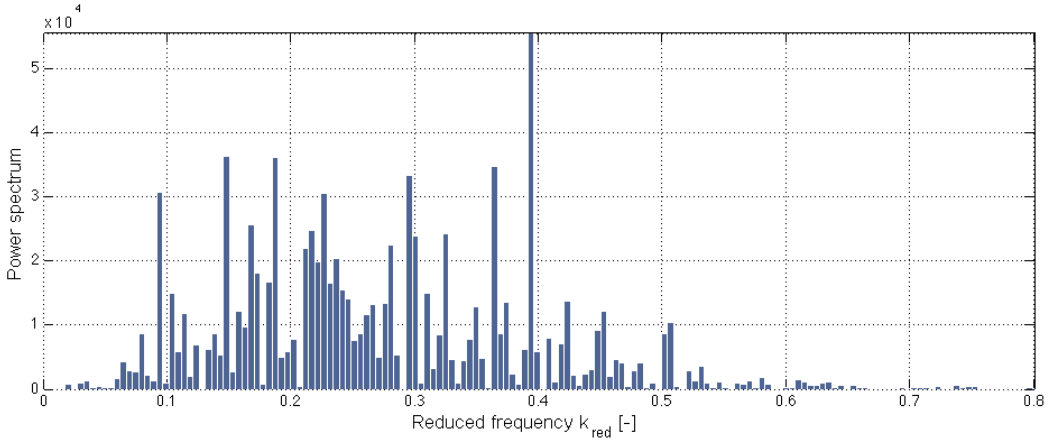

(b) PSD of the random sinusoidal signal

Figure 3.3: Sinusoidal signal with random amplitudes and frequencies used for the first mode

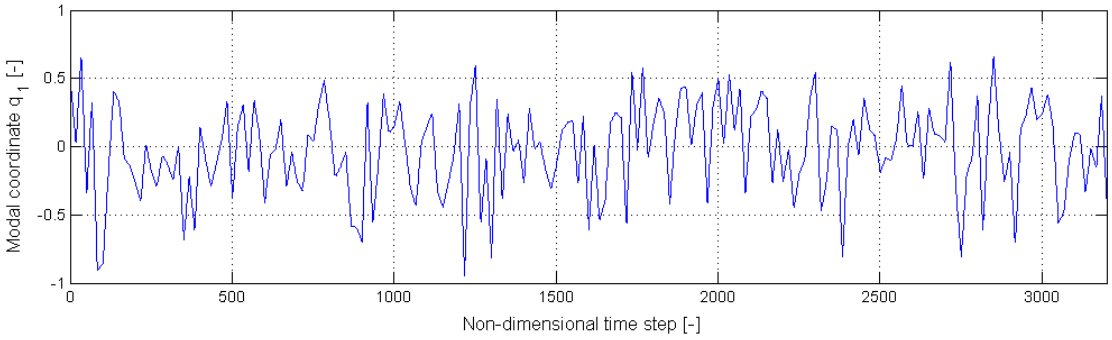

(a) Random signal in the non-dimensional time domain

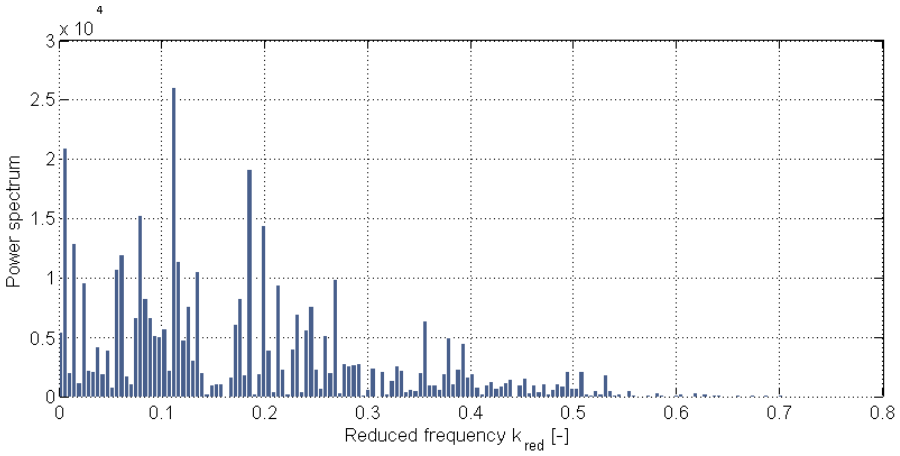

(b) Random signal PSD

Figure 3.4: Random signal for the first mode used for non-linear system identification

3.1.3 Random Signal

The last signal chosen to train the ROM is a totally *random signal*, which seems, as the APRBS and the random sinusoidal signal, to be able to be employed as a training signal. The random signal changes random the frequency and the amplitude from range defined a priori. This signal is very similar to the RSS one. The only difference is related to the irregularity of the signal due to the thin peaks, whereas the RSS is smoother. Figure 3.4 shows the random signal used for the identification purpose.

3.2 Validation Signal

The test signals designed in this work have been used for the validation phase of the reduced order model. To guarantee that the system has been trained in the right manner, different types of signals have been tested with the reduced frequency and the amplitude in the range of the training signal. The three signals selected for the validation phase are:

- *Sinusoidal signal.*
- *Generic signal.*
- *Turbulence excitation signal.*

3.2.1 Sinusoidal Signal

The sinusoidal signal has been chosen as the preliminary test for the trained ROM, because the signal has constant amplitude and frequency and for this reason should be easier to interpret by the ROM. Both, the amplitude and the frequency, have been chosen in the range of the training signal. Figure 3.5 shows an example of the sinusoidal signal suited for the validation phase. The signal selected has a constant amplitude of 0.6 and a reduced frequency of 0.24, as shown in Figure 3.5(b).

3.2.2 Generic Signal

For testing the ROM model, another interesting signal is the generic excitation [23]. This signal is an amplified frequency-modulated vibration signal as shown in Figure 3.6. The amplitude and frequency increase along the time step, up to an amplitude of 1 for both modes. With this signal it is possible to test the response of the ROM when it is excited with different amplitudes and frequencies. Using the

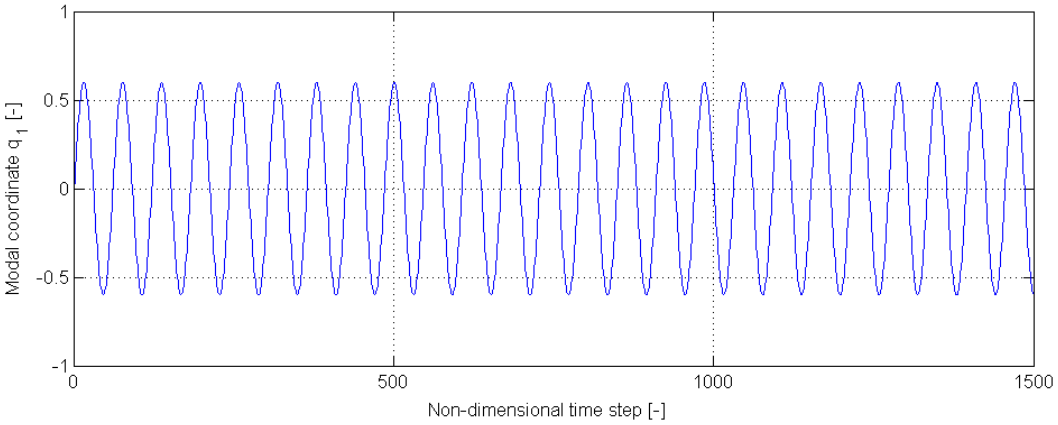

(a) Sinusoidal signal in the non-dimensional time domain

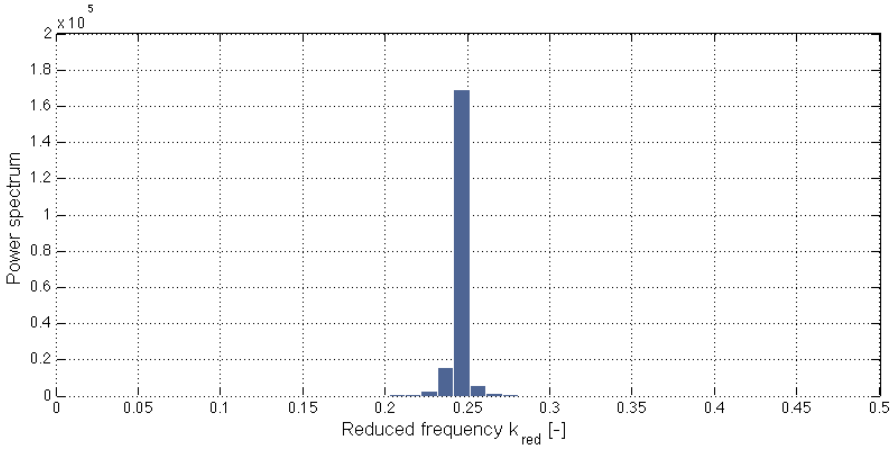

(b) Sinusoidal signal PSD

Figure 3.5: Sinusoidal signal for the first mode (validation phase)

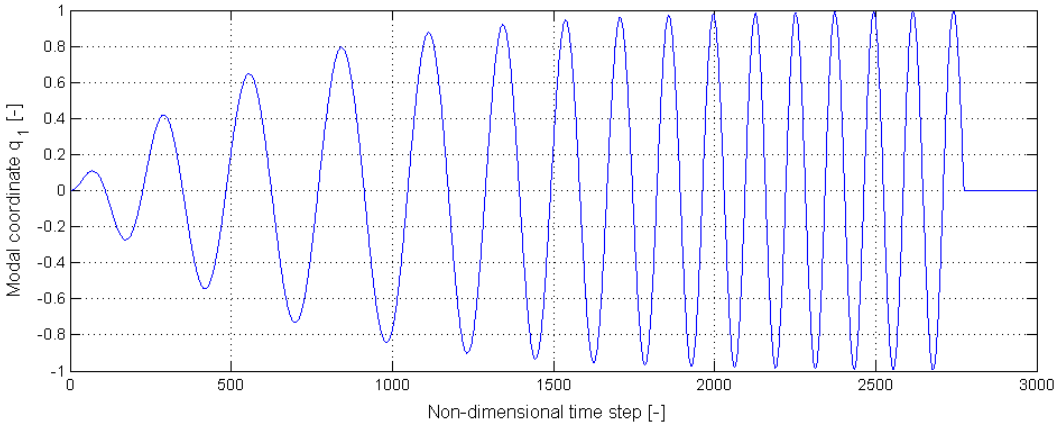

(a) Generic signal in the non-dimensional time domain [23]

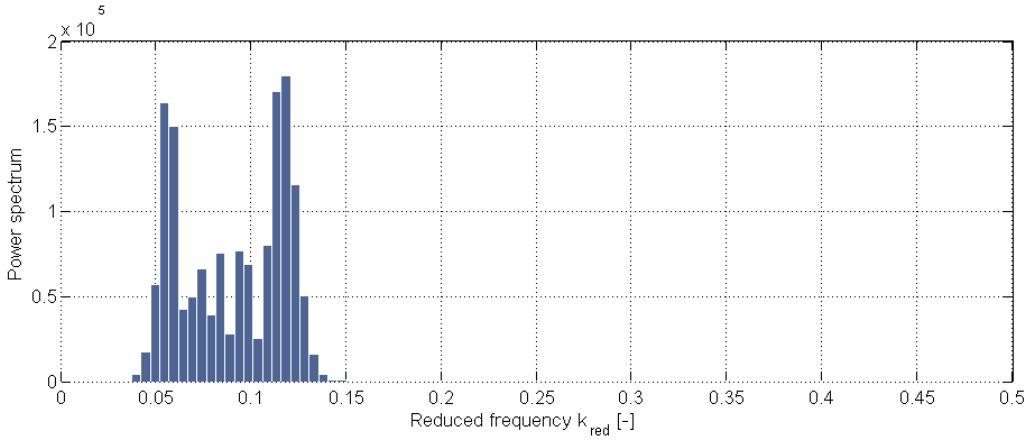

(b) Generic signal PSD

Figure 3.6: Generic signal (validation phase)

sinusoidal test signal and the generic signal the ROM is tested only with smooth signals. Therefore, the third signal selected for the validation phase is a random signal.

3.2.3 Turbulence Excitations

It is well known that, during the flight, aircrafts encounter atmospheric turbulence of varying degree of severity. Turbulence may be considered as the movement

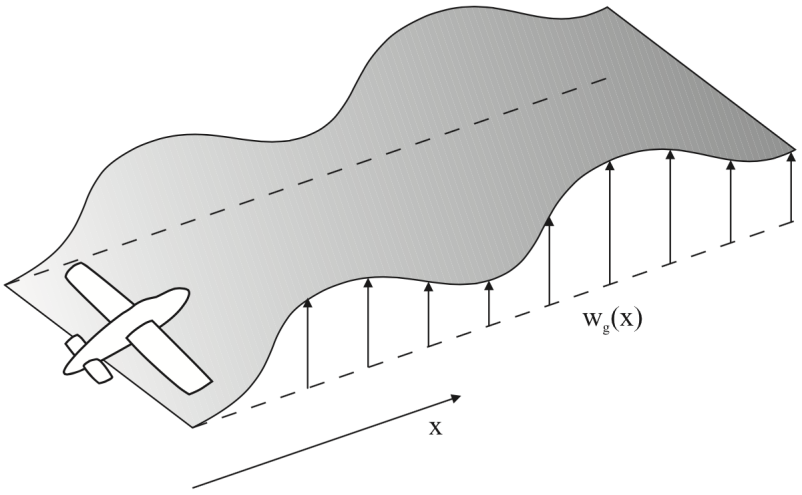

Figure 3.7: Aircraft encountering a vertical gust [17]

of the air through which the aircraft passes, which changes the effective incidence of the aerodynamic surfaces. The component of the velocity of the air that is normal to the flight path, as illustrated in Figure 3.7, causes sudden changes in the lift forces and hence a dynamic response of the aircraft involving flexible deformation. The response of the aircraft to the turbulence may give rise to discomfort for passengers and the crew and will introduce internal loads that need to be considered during the design for aircraft safety [17].
Turbulence, although a complicated phenomenon, is normally considered for design purposes in one of two idealized categories, namely [17]:

- *Discrete gust*, where the gust velocity varies in a deterministic manner, often in the form of a '1-cosine' shape.
- *Continuous turbulence*, where the gust velocity is assumed to vary in a random manner.

The difference between the two types of turbulence may be seen in Figure 3.8.

Gust and turbulence may be vertical, lateral or at any orientation to the flight path, but each direction is normally treated separately. Thus, for a symmetric air-

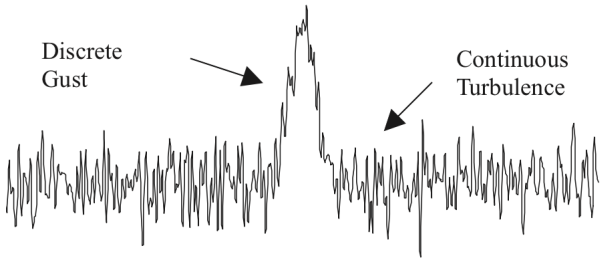

Figure 3.8: Continuous and discrete turbulence [17]

craft, a vertical gust will give rise to heave/pitch motions, whereas a lateral gust will cause sideslip/yaw/roll motions [17]. In this work, to simplify the simulation, only the vertical gust has been treated, which leads to a heave/pitch motion of the aerofoil. Furthermore, only the continuous turbulence has been considered, because it can be treated as a random signal.

Continuous turbulence is represented by a random variation in the velocity of the air normal to the flight path of the aircraft. The treatment of random continuous turbulence usually requires calculations to be performed in the frequency domain using a power spectral density (PSD). In this thesis the turbulence has been approximated by a random signal, which excites the aerofoil heave/pitch motions. Figure 3.9 depicts the random signal that has been used to stimulate the ROM model and the respective PSD.

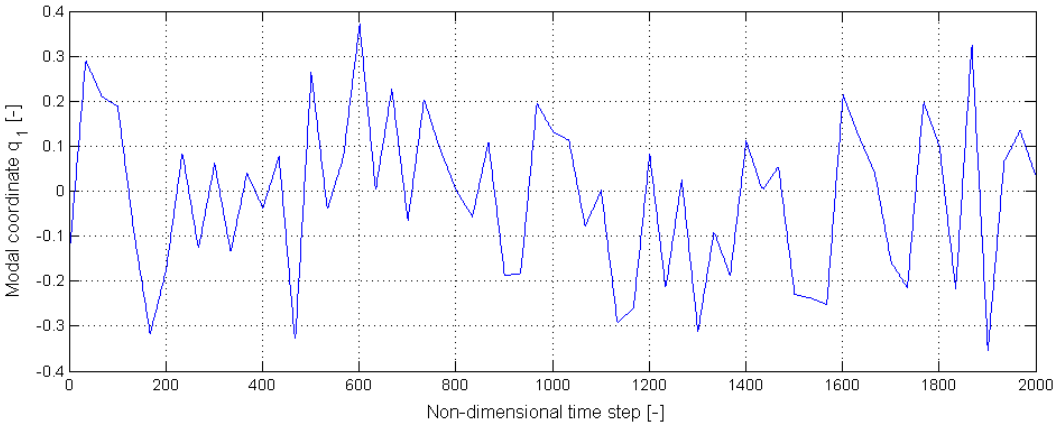

(a) Turbulence excitation in the non-dimensional time domain

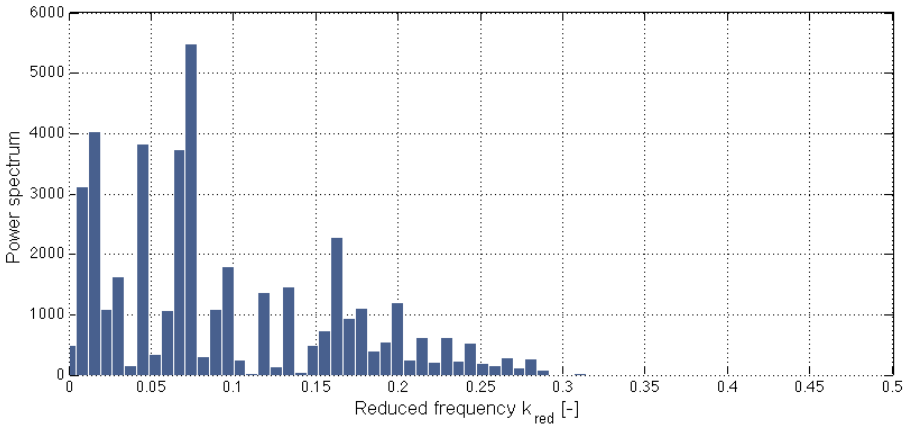

(b) Turbulence PSD

Figure 3.9: Turbulence excitation for the first mode (validation phase)

Chapter 4

Coupling of Structural Dynamics with Fluid Dynamics

In computational aeroelasticity fluid forces must be communicated to a structural grid and the resulting deflections of this grid must be communicated back to the aerodynamic mesh. Usually this is complicated, because the number of nodes in the CFD mesh is higher than the number of nodes in the structural grid. Thus, to obtain the equivalent accuracy the CFD mesh has more nodes than the structural grid.

An efficient and accurate coupling method is therefore critical in developing a coupled CFD-CSD methods [25].

A typical coupled fluid structure analysis diagram is shown in Figure 4.1. For every time step, one needs to map the surface loads from the CFD mesh onto the structural grid to obtain the forces on the CSD grid system, which are then used to obtain the displacements on the CSD grid. Maintaining accuracy in the data exchange process is very important in order to obtain correct aeroelastic results. The complexity of the coupled system increases and therefore the computational effort increases in turn. Several techniques exist to carry out these interpolations/extrapolations, i.e. infinite-plate splines (IPS) or thin-plate splines (TPS), see Kamakoti [31]. All these methods well approximate the response of the aeroelastic model; however, the whole computational time involves the effort for the

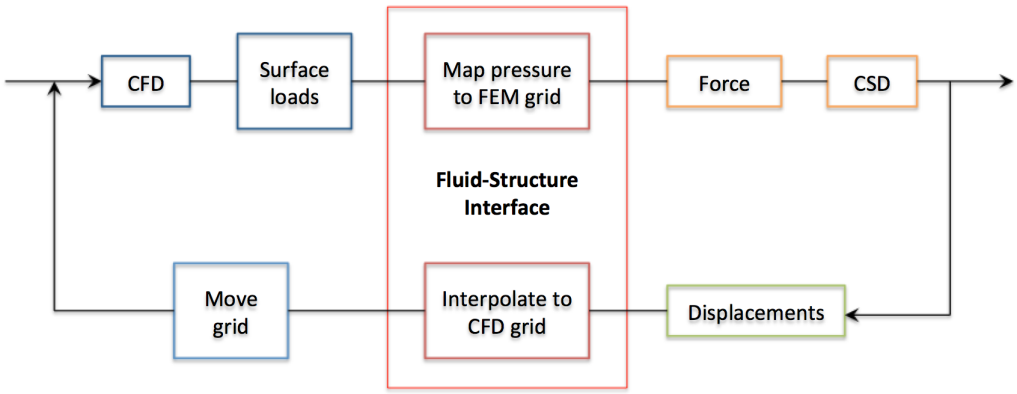

Figure 4.1: Coupled fluid-structure flow diagram

CFD unsteady simulations and the CFD-CSD simulations. For this reason other methods that can well approximate the aeroelastic solution and reduce considerably the computational effort have been developed.
In order to satisfy these requirements, the reduced order model can be coupled with the structure. The resulting aeroelastic system should be able to predict the main non-linearities of the flow, thus the LCO can be computed using a more compact model than the coupled CFD-CSD model.
A coupled fluid-structure simulation algorithm can be used to integrate the equation 2.33 of the structure in state-space form in the time domain along with any unsteady flow solver or ROM to determine the characteristics of the coupled aeroelastic system.
In this chapter several schemes used to integrate equation 2.33 in the time domain will be used.

4.1 Time Marching Methods

4.1.1 Euler Methods

The first order-method is one of the basic time integration schemes. It is an explicit method and therefore it is easier to implement. The equations of the Euler

method reads as

$$\dot{\vec{x}}_k = \frac{\vec{x}_k - \vec{x}_{k-1}}{\Delta t} \tag{4.1}$$

$$\vec{x}_k = \vec{x}_{k-1} + \Delta t(\boldsymbol{A}\vec{x}_{k-1} + \boldsymbol{B}\vec{u}_{k-1}) \tag{4.2}$$

where Δt is the time step chosen by the user in the previous unsteady simulation, $\vec{u}$ is the input vector, $\vec{x}$ is the state vector and k refers to the k-th time step. The main drawback of this method is that it tends to be unstable for not small enough time steps [37].
In order to avoid this problem in this work other approaches have been used.

4.1.2 Hybrid Linear Multistep Scheme

Referring to Zhang [39], a type of second-order hybrid linear multistep scheme for coupled fluid-structure simulation is used to integrate Equation 2.33 in the time domain. This scheme is based on the second order implicit *Adams Linear Multistep Scheme* (IALM) involving a predictor step and a corrector step.

$$\vec{x}_{pred,k} = \vec{x}_{k-1} + \frac{\Delta t}{2}(3\boldsymbol{A}\vec{x}_{k-1} - \boldsymbol{A}\vec{x}_{k-2}) + \frac{\Delta t}{2}(3\boldsymbol{B}\vec{u}_{k-1} - \boldsymbol{B}\vec{u}_{k-2}) \quad (predictor) \tag{4.3}$$

$$\vec{x}_k = \vec{x}_{k-1} + \frac{\Delta t}{2}(\boldsymbol{A}\vec{x}_{k-1} - \boldsymbol{A}\vec{x}_{pred,k}) + \frac{\Delta t}{2}(\boldsymbol{B}\vec{u}_{k-1} - \boldsymbol{B}\vec{u}_{pred,k}) \quad (corrector) \tag{4.4}$$

where $\vec{u}_{pred,k}$ denotes the input at time step k yielded by the predicted state vector $\vec{x}_{pred,k}$. For instance, the input vector of the structural model is the vector of the generalized forces, which are coupled to the modal displacements vector contained in the state vector. With this scheme, the aerodynamic loads will be evaluated twice at each time step; once for the corrector step and then for the computation of the actual loads yielded by the deformation that has just been provided by the scheme.

The *Hybrid Linear Multistep Scheme* (HLM) has been obtained once extrapolating the aerodynamic loads of the $k-$th corrector step from several prior values:

$$\vec{u}_k = 2\vec{u}_{k-1} - \vec{u}_{k-2} \tag{4.5}$$

and the second order HLM scheme reads

$$\vec{x}_{pred,k} = \vec{x}_{k-1} + \frac{\Delta t}{2}(3\boldsymbol{A}\vec{x}_{k-1} - \boldsymbol{A}\vec{x}_{k-2}) + \frac{\Delta t}{2}(3\boldsymbol{B}\vec{u}_{k-1} - \boldsymbol{B}\vec{u}_{k-2}) \tag{4.6}$$

$$\vec{x}_k = \vec{x}_{k-1} + \frac{\Delta t}{2}(\boldsymbol{A}\vec{x}_{k-1} + \boldsymbol{A}\vec{x}_{pred,k}) + \frac{\Delta t}{2}(3\boldsymbol{B}\vec{u}_{k-1} - \boldsymbol{B}\vec{u}_{k-2}) \tag{4.7}$$

The same method can be applied with the following fourth order extrapolation:

$$\vec{u}_k = 4\vec{u}_{k-1} - 6\vec{u}_{k-2} + 4\vec{u}_{k-3} - \vec{u}_{k-4} \tag{4.8}$$

Using the second order implicit IALM scheme as basis the 4th order HLM scheme can be obtained:

$$\begin{aligned}\vec{x}_{pred,k} = \vec{x}_{k-1} + \frac{\Delta t}{24}(55\boldsymbol{A}\vec{x}_{k-1} - 59\boldsymbol{A}\vec{x}_{k-2} + 37\boldsymbol{A}\vec{x}_{k-3} - 9\boldsymbol{A}\vec{x}_{k-4}) + \\ + \frac{\Delta t}{2}(55\boldsymbol{B}\vec{x}_{k-1} - 59\boldsymbol{B}\vec{x}_{k-2} + 37\boldsymbol{B}\vec{x}_{k-3} - 9\boldsymbol{B}\vec{x}_{k-4})\end{aligned} \tag{4.9}$$

$$\begin{aligned}\vec{x}_k = \vec{x}_{k-1} + \frac{\Delta t}{24}(9\boldsymbol{A}\vec{x}_{pred,k} + 19\boldsymbol{A}\vec{x}_{k-1} - 5\boldsymbol{A}\vec{x}_{k-2} + \boldsymbol{A}\vec{x}_{k-3}) + \\ + \frac{\Delta t}{2}(55\boldsymbol{B}\vec{u}_{k-1} - 59\boldsymbol{B}\vec{u}_{k-2} + 37\boldsymbol{B}\vec{u}_{k-3} - 9\boldsymbol{B}\vec{u}_{k-4})\end{aligned} \tag{4.10}$$

The HLM schemes of 2nd and 4th order don't require any evaluation of the aerodynamic forces in the corrector step. The implicit IALM scheme has been turned into an explicit scheme, yet using a predictor-corrector procedure. The superior accuracy, stability and computational efficiency of the scheme are also demonstrated in Zhang [39].

4.2 Coupling of a Non-Linear ROM with the Structural Model

As already introduced in section 2.4.4 a neural network capable of predicting the non-linear effects introduced by the aerodynamic has to take into account the delay inputs and the delay outputs of the system. The neural network used in this work provides at each time step an evaluation of the generalized aerodynamic forces (GAFs), taking several previous values m of inputs (modal displacements) and outputs n (GAFs) into account.
During the coupled simulation the time step is fixed by the non-dimensional time step used in the neural network, because the neural network does not involve any integration scheme and therefore there is no possibility to choose another $\Delta\tau$. The dimensionless time step $\Delta\tau$ is linked to the physical time step as follows:

$$\Delta t = \Delta\tau \cdot \sqrt{\frac{\rho_\infty}{p_\infty \cdot k}} \cdot \frac{1}{Ma_\infty} \tag{4.11}$$

where ρ_∞ and p_∞ are the density and the pressure of the free stream. The computed time step Δt will be used for the time integration of the structural model. First, the matrices of the state-space model form of the structural model $\boldsymbol{A}$ and $\boldsymbol{B}$ will be computed in order to get the parameters to solve the algorithm based on the state-space model equations.

The modal displacements contained in $\vec{x}_k$ are derived from prior values of the structural state vector and generalized aerodynamic forces using the HLM procedure:

$$\vec{x}_k = f(\boldsymbol{A}, \boldsymbol{B}, \vec{x}_{k-1}, \vec{x}_{k-2}, ..., \vec{x}_{k-m}, \vec{f}_{gen,k-1}, \vec{f}_{gen,k-2}, ..., \vec{f}_{gen,k-n}) \tag{4.12}$$

Under the assumption that the coupled system is at rest before the beginning of the simulation, the initialisation values are all set to the corresponding steady-state values. Thus, initial values for the $\vec{f}_{gen,1}$ and $\vec{f}_{gen,2}$ have to be chosen from the AER-Eu CFD steady aerodynamic simulations. Subsequently the modal displacements will be scaled with values computed by the *Lehrstuhl für Aerodynamik und Strömungsmechanik* in order to obtain the real displacements.

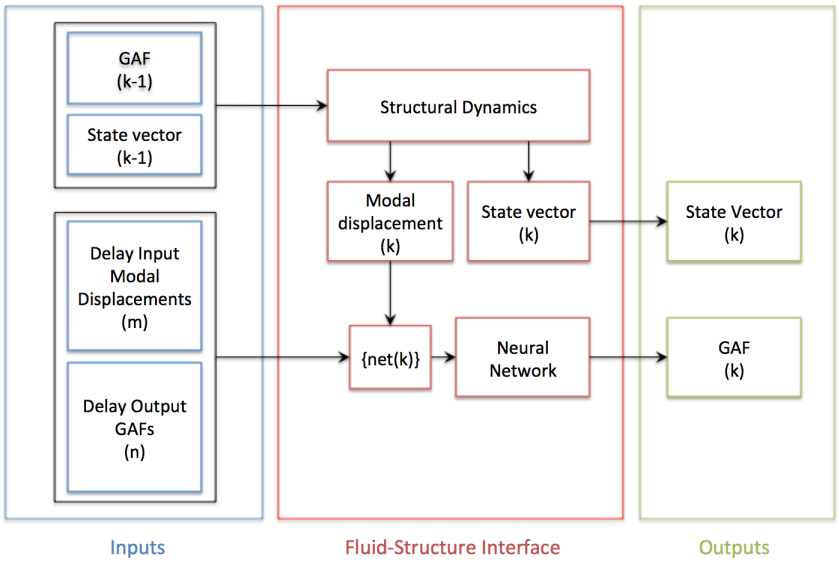

Figure 4.2: Coupling of a structural model with a ROM at time step k for a first order time integration scheme

The neural network function used in the coupled code will be referred as a function *net* and permits to compute the generalized aerodynamic forces. The input of this function consists of a vector input containing the current modal displacement vector as well as its m previous instances and the n previous values of the generalized aerodynamic forces computed by the ROM. It yields the generalized aerodynamic forces vector at the current time step:

$$\vec{f}_{gen,k} = net([\vec{q}_k, \vec{q}_{k-1}, ..., \vec{q}_{k-m}, \vec{f}_{gen,k-1}, ..., \vec{f}_{gen,k-n}]^T) \tag{4.13}$$

This procedure is repeated for a number of time steps N chosen by the user.
Figure 4.2 shows a flow scheme of the entire model used to obtain the non-linear aeroelastic response of the system at time step k for a first order time integration scheme.
Coupling the ROM with the structural dynamics allows to decrease the computational time with respect to the standard CFD-CSD simulation.

Chapter 5

Results and Discussion

5.1 Test Case: NLR 7301 Supercritical Aerofoil

A conventional wing is rounded on top and flat on the bottom. The supercritical wing is flatter on the top, rounded on the bottom, and the upper trailing edge is accented with a downward curve to restore lift lost by flattening the upper surface.

When an aircraft is flying at what is called critical speed, air flowing across the top and eventually the bottom of the wing moves faster and creates a shock wave. This shock wave causes the smooth flow of air hugging the upper surface of the wing to separate from the wing and create turbulence. The air becomes unsteady and churning, and drag increases. This increases fuel consumption and it can also cause vibrations. *Supercritical wings* (SCW) have a flat-on-top "upside down" look. As air moves across the top of the SCW, it does not speed up nearly as much as over a curved upper surface. This delays the onset of the shock wave and also reduces aerodynamic drag associated with boundary layer separation. Lift that is lost with less curvature on the upper surface of the wing is regained by adding more curvature to the upper trailing edge. Now the aircraft can cruise at a higher speed and fly up into the supercritical range and with less drag, the aircraft is using less fuel than it would otherwise consume [3].

The NLR7301 supercritical aerofoil section is shown in Figure 5.1. This geometry

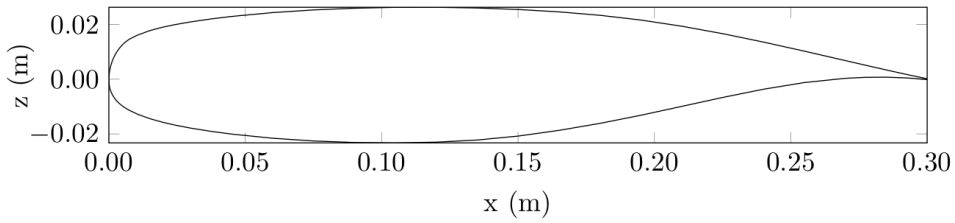

Figure 5.1: Geometry of the NLR7301 aerofoil [37]

has already been investigated in the context of nonlinear aeroelastic analysis, see Weber et al. [36], Harris [3] and Tang et al. [20]. It has a maximum thickness of 16.5% at 35% of the chord length and a maximum camber of 1.7% at 75% of the chord length. Figure 5.2 depicts a simplified model of the two-degree-of-freedom test set-up. The two-dimensional wing has a chord length of 0.3 m ($c = 0.3$ m) and a span of 1 m ($b = 1$ m). The plunge spring and the pitch spring are attached to the same $c/4$ position. The corresponding two-degree-of-freedom equation of motion of the set-up reads as [20]

$$\begin{bmatrix} m_h & -s_\alpha \\ -s_\alpha & I_{c/4} \end{bmatrix} \begin{bmatrix} \ddot{h} \\ \ddot{\alpha} \end{bmatrix} + \begin{bmatrix} D_h & 0 \\ 0 & D_\alpha \end{bmatrix} \begin{bmatrix} \dot{h} \\ \dot{\alpha} \end{bmatrix} + \begin{bmatrix} K_h & 0 \\ 0 & K_\alpha \end{bmatrix} \begin{bmatrix} h \\ \alpha - \alpha_0 \end{bmatrix} = \begin{bmatrix} L(t) \\ M(t) \end{bmatrix} \tag{5.1}$$

where m_h is the total mass, $I_{c/4}$ is the mass moment of inertia about $c/4$, s_α is the static unbalance, D_h and D_α are the damping factors of the plunge motion (h) and the pitch motion (α), K_h and K_α are the stiffness of the plunge spring and the pitch spring, and $L(t)$ and $M(t)$ are the aerodynamic lift and moment, respectively, in Newton and Newton-meter.

5.2 NLR 7301 Aerofoil Modal Analysis

For the modal analysis, the 2-dimensional wing[1] is considered, which is exposed in section 5.1. This section is subjected to a plunge h and a pitch α motion in the plane containing the section, which represent the torsional and bending motion of

[1]The wing is 3-dimensional, but its geometry is a simple extrusion of the NLR7301 aerofoil.

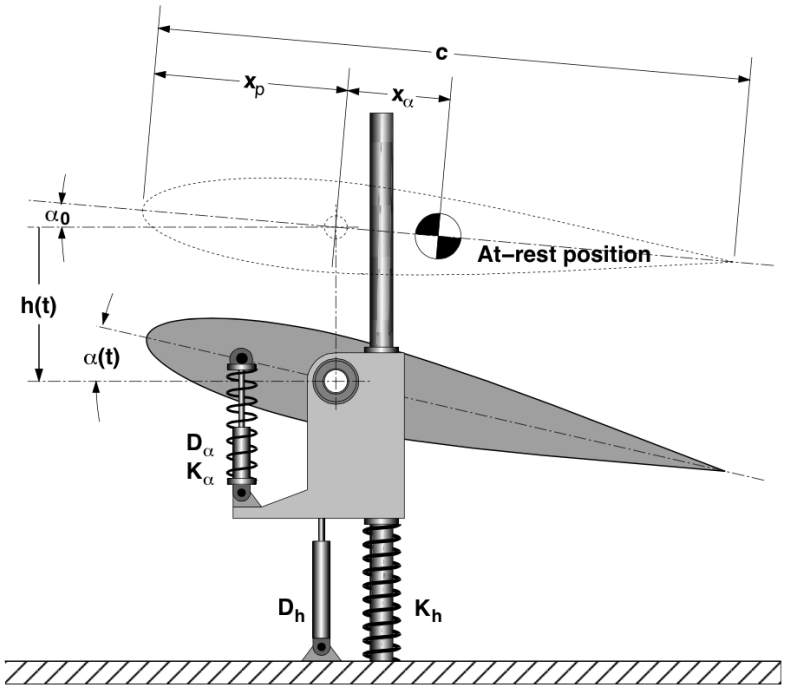

Figure 5.2: Two degree of freedom dynamic model [36]

the wing, governed by the lift L and pitching moment M respectively. From Figure 5.2 it can be seen how the system is characterized by a spring-damper system for the plunge motion (K_h and D_h) and one for the pitch motion (K_α and D_α).
The numerical values of the parameters used in the structure equation 5.1 of the NLR7301 can be found in Table A.1. These parameters referred to Weber et al. [36] and Tang et al. [20] experimental data.
Applying the modal transformation described in section 2.2 to equation 5.1 and solving using MATLAB the modal parameters listed in Table 5.1 has been found. From Table 5.2 it can be seen that the values computed with MATLAB are different from those computed in Tang et al. [20]. Since the values differ in very small percentage, these are considered acceptable.
The diagonal values of the modal stiffness matrix correspond to the squared values of the undamped natural frequencies of the plunge and the pitch motions, respectively $\omega_h = 205.6$ rad/s and $\omega_\alpha = 298.35$ rad/s. Hence, the structural equation

Table 5.1: Modal parameters of the NLR7301 aerofoil obtained with MATLAB

Matrix	**Variable**	**MATLAB**
Modal matrix	$\boldsymbol{\Phi}$	$\begin{bmatrix} -0.1741 & 0.0985 \\ 0.9139 & 3.4009 \end{bmatrix}$
Modal mass matrix	$\underline{\boldsymbol{M}}$	$\boldsymbol{I}_2$
Modal stiffness matrix	$\underline{\boldsymbol{K}}$	$\begin{bmatrix} 4.2272 \cdot 10^4 & 0 \\ 0 & 8.9010 \cdot 10^4 \end{bmatrix}$
Modal damping matrix	$\underline{\boldsymbol{D}}$	$\begin{bmatrix} 2.6785 & -0.8102 \\ -0.8102 & 3.0835 \end{bmatrix}$

Table 5.2: Modal matrix of the NLR7301 aerofoil obtained with MATLAB compared with the modal matrix computed in Tang et al. [20]

Matrix	**Variable**	**MATLAB**	**Tang et al.**
Modal matrix	$\boldsymbol{\Phi}$	$\begin{bmatrix} -0.1741 & 0.0985 \\ 0.9139 & 3.4009 \end{bmatrix}$	$\begin{bmatrix} -0.1735 & 0.1004 \\ 0.9277 & 3.4030 \end{bmatrix}$

becomes

$$[\boldsymbol{I}]\{\ddot{\boldsymbol{q}}\} + \begin{bmatrix} 2\omega_h\xi_h & 0 \\ 0 & 2\omega_\alpha\xi_\alpha \end{bmatrix} \{\dot{\boldsymbol{q}}\} + \begin{bmatrix} \omega_h^2 & 0 \\ 0 & \omega_\alpha^2 \end{bmatrix} \{\boldsymbol{q}\} = \boldsymbol{\Phi}^T \begin{Bmatrix} L(t) \\ M(t) \end{Bmatrix} \tag{5.2}$$

where ξ_h and ξ_α are the plunge and pitch damping ratios.

5.3 NLR 7301 Aerodynamic Analysis

In the following section, the aspects relative the NLR7301 steady aerodynamic analysis will be presented. The CFD grid will be introduced and the steady simulations exploited with the AER-Eu code will be analysed and compared with those computed in literature.

5.3.1 CFD Grid

The grid used for the CFD computations has been built by the aerodynamic department of the TUM with the ICEM CFD software. The grid is suited for Euler computation; hence, the quality of the grid is less refined, especially near the wall. A low quality grid can cause several numerical errors and thus influence the results of the CFD computation. However, a grid of good quality for complex geometry can be a very time-demanding task, since many parameters have to be taken into account.
A 2-D and 3-D view of the mesh that has been provided are depicted in Figure 5.3 and 5.4.

5.3.2 Steady Simulation Results

In order to evaluate the approximation of the Euler equations for the airflow on the NLR7301 aerofoil and in order to have a starting condition for the unsteady simulation a steady-state simulation is necessary.
The NLR7301 aerofoil offers a distinct nonlinear aerodynamic behaviour in the transonic flight regime due to the presence of a strong shock. For this reason, different Mach numbers have been tested to find the proper condition where the

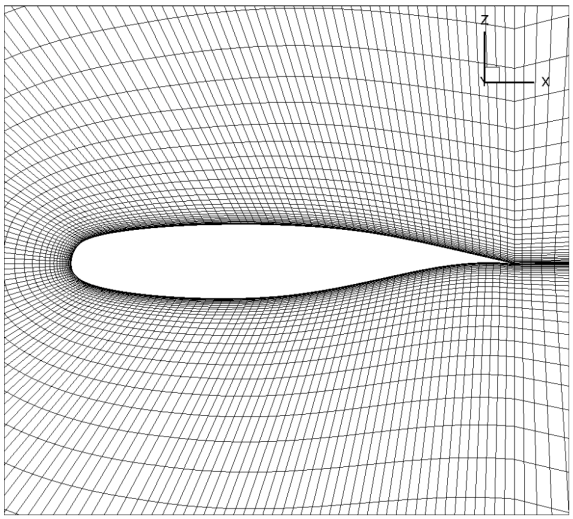

Figure 5.3: Grid used for the Euler computations of the airflow around the NLR7301 aerofoil

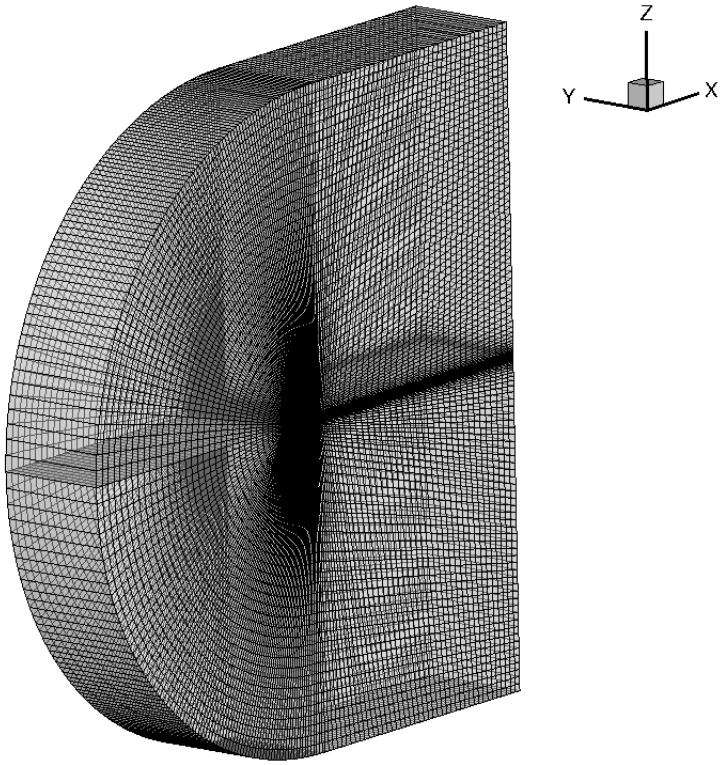

Figure 5.4: 3-D view of the grid used for the Euler computations of the airflow around the NLR7301 aerofoil

shock wave occurs. According to Weber et al. [36] and Tang et al. [20] the first choice is a Mach number of 0.753 and an angle of attack of 0.6 deg. In this manner it is possible to compare the results of the experimental test performed in Weber et al. [36] with the results of the AER-Eu software using the Euler equations.
Figure 5.5 depicts the difference of the pressure distribution (C_p) on the aerofoil between the experimental data measured in Weber et al. [36] and the data obtained from the AER-Eu code, whereas Figure 5.7 shows the distribution of the Mach number around the aerofoil. From the figure it is clearly visible how, at $Ma_\infty = 0.753$ for the Euler case, the flow on the upper side is more accelerated than in the experiment, so the pressure coefficient is lower and the lift coefficient slightly overestimated. Furthermore, the location of the predicted shock is behind the measured one. According to Tang et al. [20], it appears to be impossible to match both the measured strength and location of the shock using the Euler equations. Only using viscous models it is possible to approximate the experimental steady-state solution, as it is shown in Figure 5.6. In Tang et al. [20], two viscous computations are performed, one with the Degani-Schiff modified Baldwin-Lomax turbulence model (B-L-D-S) and the other with the Spalart-Allmaras turbulence model (S-A).
Despite these differences, Euler computation will be used for this work because of the lower computational effort compared to the Navier-Stokes simulation and the capacity to capture the nonlinear aerodynamic phenomena.

In order to verify at which Mach number the shock occurs and the behaviour of the airflow around the aerofoil two other steady simulations are then performed using a Mach number of $Ma_\infty = 0.5$ and $Ma_\infty = 0.9$ with an angle of attack of 0.0 deg.
The steady solution of the wing at $Ma_\infty = 0.5$ and $\alpha = 0.0$ deg, depicted in Figure 5.8, shows that the shock wave is not present due to the subsonic Mach number. Thus, the airflow does not meet the shock wave phenomenon. For the Euler computation at $Ma_\infty = 0.753$ and $\alpha = 0.0$ deg, a compression shock on the upper side of the aerofoil can be clearly seen from Figure 5.9(a), whereas a compression shock, with a different location on the aerofoil, on the upper and

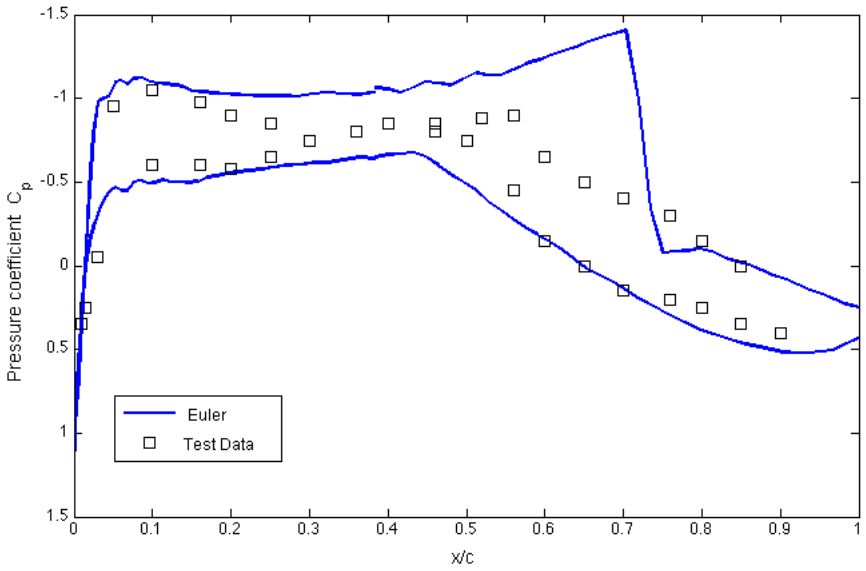

Figure 5.5: Pressure coefficient distribution of the steady-state on the NLR7301 aerofoil with a free stream Mach number $Ma_\infty = 0.753$ and an angle of attack $\alpha = 0.6$ deg

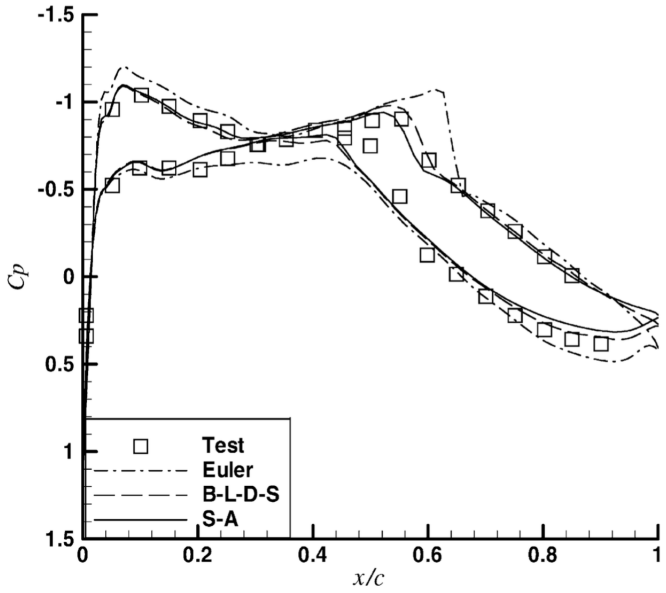

Figure 5.6: Pressure coefficient distribution of the steady-state on the NLR7301 aerofoil with a free stream Mach number $Ma_\infty = 0.753$ and an angle of attack $\alpha = 0.6$ deg performed by Tang et al. [20]

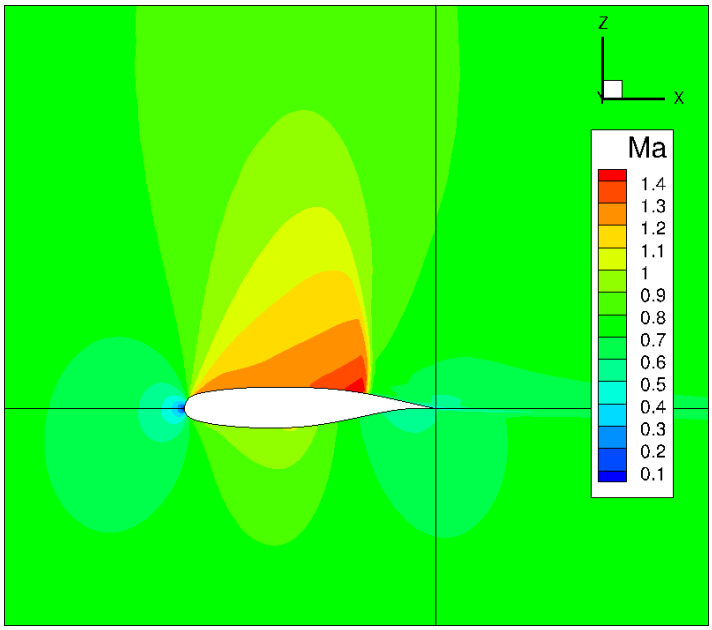

Figure 5.7: Steady simulation of the NLR7301 at $Ma_\infty = 0.753$ and $\alpha = 0.6$ deg

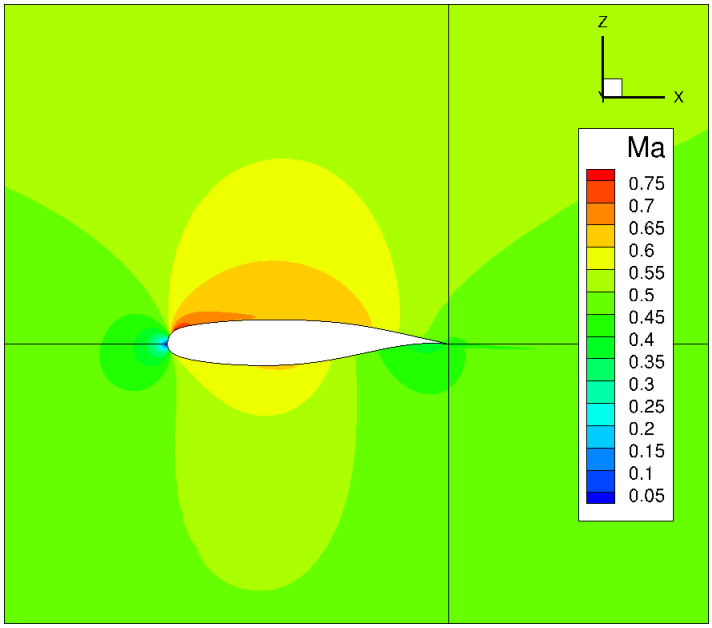

Figure 5.8: Steady simulation of the NLR7301 at $Ma_\infty = 0.5$ and $\alpha = 0.0$ deg

lower surface can be seen in Figure 5.9(b) at $Ma_\infty = 0.9$ and $\alpha = 0.0$ deg. Figure 5.9 shows that for both the Mach number considered the shock phenomenon is encountered.
Furthermore, Figure 5.10 depicts the pressure distribution on the aerofoil for the three different Mach numbers tested at $\alpha = 0.0$ deg using the Euler equations.
For this reason, in this work only Mach numbers of $Ma_\infty = 0.9$ and $Ma_\infty = 0.753$ with $\alpha = 0.0$ deg and $\alpha = 0.6$ deg will be considered in order to study the nonlinear phenomena caused by the shocks and subsequently to compare the data obtained with $\alpha = 0.6$ deg with the experimental/numerical results obtained in Weber et al. [36] and Tang et al. [20].

5.4 ROMs Training and Validation Phase

Using the training signals exposed previously, chapter 3, it is possible to train the reduced order models in order to evaluate the response of the aerodynamic system to the simultaneously superimposed modal deflection.
Thanks to the modal analysis performed in section 5.2, the values of the undamped natural frequencies of the plunge and pitch motions have been found, approximately 33 Hz for the first mode and 47 Hz for the second mode.
As explained in chapter 3, using the values of the undamped natural frequencies it is possible to find the approximate values of the reduced frequencies that can be used to design the training signals for the NLR7301 aerofoil model. Hence, the frequencies of the training signals will be centered on these values in order to capture the aeroelastic phenomena, like Limit Cycle Oscillations (LCO), which occur near these frequencies according to the experimental data of Weber et al. [36] and Tang et al. [20].
As introduced, in the aeroelastic analysis the reduced frequency is used to study the LCO phenomena. Thus, from equation 2.8 with $p_\infty = 101325$ Pa, $\rho_\infty = 1.225$ Kg/m^3, $T_\infty = 288.15$ K, $k = 1.4$, $l_{ref} = 0.3$ and $Ma_\infty = 0.753$ the first and the second reduced frequencies of the two modes are respectively $k_{red_1} = 0.24$ and $k_{red_2} = 0.34$, where l_{ref} is the reference aerodynamic length of the aerofoil. In

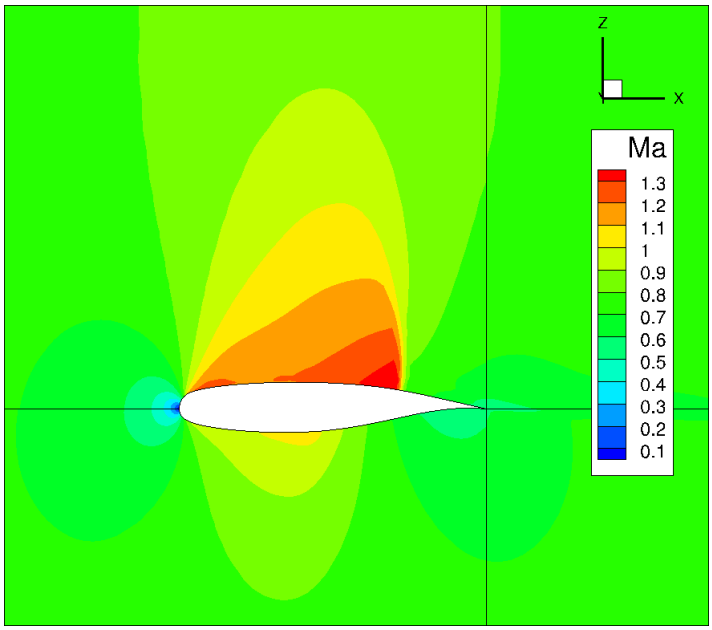

(a) $Ma_\infty = 0.753$ and $\alpha = 0.0$ deg

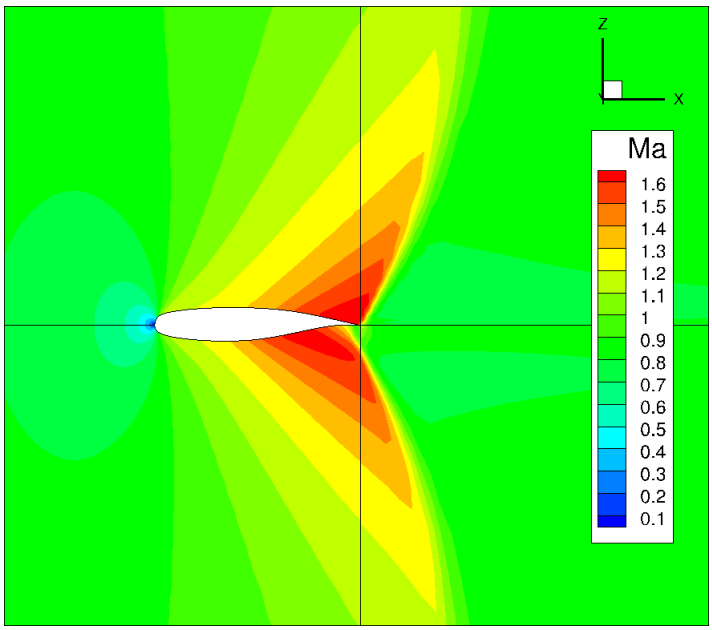

(b) $Ma_\infty = 0.9$ and $\alpha = 0.0$ deg

Figure 5.9: Steady simulation of the NLR7301

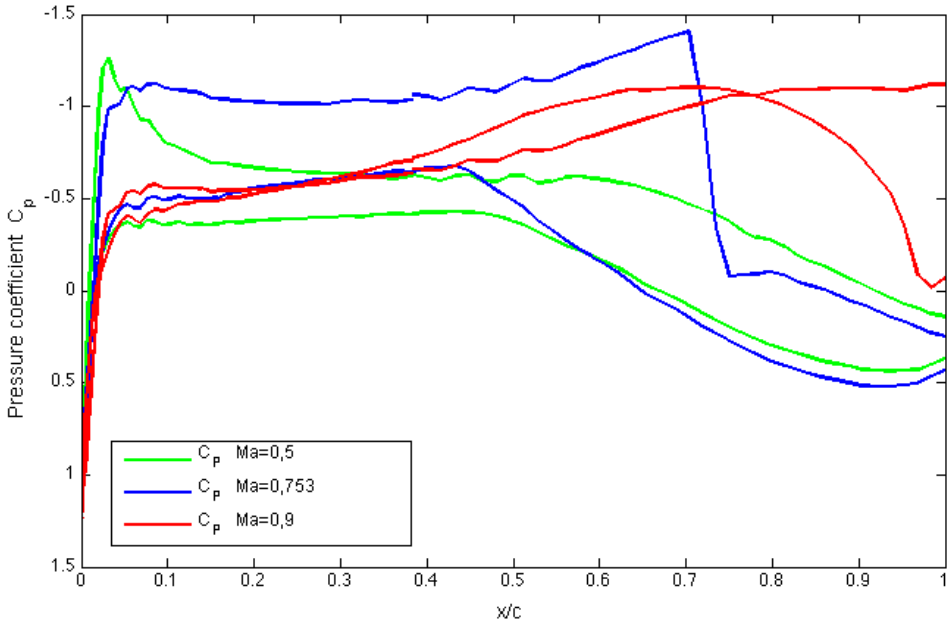

Figure 5.10: Pressure coefficient distribution of the steady-state on the NLR7301 aerofoil with $\alpha = 0.0$ deg

this work, it has been chosen to design the training signals around the reduced frequency of the two modes in order to reduce the CFD computational effort. A training signal that has a wide range of frequencies needs a lot of time in terms of computational effort for the CFD simulation.

During the unsteady AER-Eu simulation, the 2 DOF aerofoil is forced in rigid plunge and pitch motion with the training input designed in chapter 3. Thus, the CFD simulation represents a purely unsteady aerodynamic problem since no mass and stiffness characteristics of the aeroelastic system are specified and the aerofoil is treated like a rigid body. The aerodynamic system to be identified is characterized by two inputs and two outputs as a *Multi Input Multi Output* (MIMO) model. Successively, the CFD data obtained can be used for the training process of the ROM.

Figure 5.11 represents the schematic role of the RBF or LOLIMOT as aerodynamic ROM.

After the model has been trained, it has been possible to validate it with one or

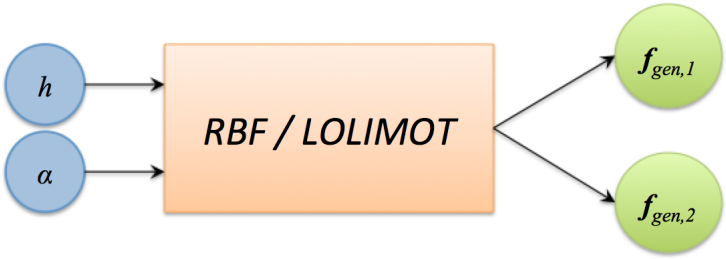

Figure 5.11: Scheme of the MIMO ROM model

more of the validation signals presented in chapter 3 in order to verify the response of the system.

To summarize the discussed reduced order methods outlined in section 2.4, a composite of the multidisciplinary approaches is given in Figure 5.12. The AER-Eu code starts from the results of the steady simulation, with the Mach number and the angle of attack chosen a priori, and solves the unsteady simulation using the designed input signal for the modal displacements. As a result of the particular AER-Eu simulation, the time-series of the generalized force vector $f_{gen}(\tau)$ is obtained. Figure 5.12 depicts the output of the unsteady ROM simulation as a function of the nondimensional time given by equation 3.1. The neural networks for the reduced order models selected in this thesis are the *Radial Basis Function Network* (RBF) and the *Local Linear Model Tree Algorithm* (LOLIMOT), which have been implemented by Dipl.-Ing. Maximilian Winter. In order to select the intrinsic parameters of both models preliminary simulations with the parameters commonly used in literature have been done. Table 5.3 shows the main parameters selected in this work after preliminary attempts.

In the following simulations, 70% of the chosen training signal is considered as the training set for conditioning the nonlinear RBF-ROM and LOLIMOT-ROM, as suggested by Winter and Breitsamter. The remaining 30% of the data is exploited for verification purposes in order to realize a stable and accurate model.

Furthermore, the present work uses the orthogonal least squares (OLS) method as training procedure for the RBF-NN. The procedure chooses radial basis function

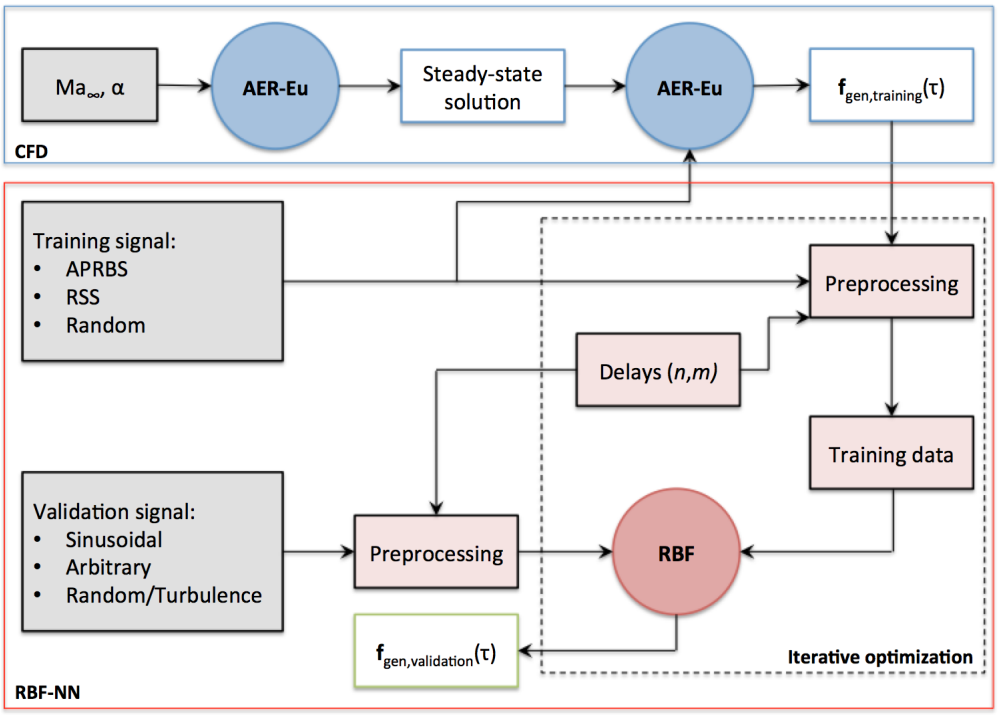

Figure 5.12: Scheme of the RBF-ROM method

centers one by one in a rational way until an adequate network has been constructed. The OLS method can be employed as a forward regression procedure to select a suitable set of centers (regressors) from a large set of candidates. At each step of the regression, the increment to the explained variance of the desired output is maximized. This rational approach provides an efficient learning algorithm for fitting adequate RBF networks [33].
Instead, for the LOLIMOT algorithm, it has been chosen a maximum number of local linear models (LLMs) of 5. In this manner, it has been reached a trade off between the computational effort and the maximum error, which no decrease employing higher number of LLMs. The delays input and output have been chosen in order to avoid some kind of instability that might show up if too high delays orders are selected. Figure 5.13, 5.14 and 5.15 depict the maximum mean squared error relative to the input-output delay order choice. In these figures, the maximum mean squared error for the two generalized aerodynamic forces captured by the ROMs is shown, whereas an empty space has been left when the system becomes numerically unstable due to the higher delay order. For example, from Figure 5.13(a), it is possible to see how the system becomes unstable already for a lower input-output delay order, respectively $m = 3$ and $n = 3$. This kind of instability is due to the properties of the APRBS training signal, which induces some kind of numerical instability in the code. Probably, the multiple plateau are not so suited for a dynamic system, but they are better for a linear system. Although using the RBF-ROM with the APRBS signal the system becomes unstable, using the LOLIMOT-ROM the system is stable even with high delay orders. Thus, Figure 5.16, underlines the input-output delay and the respective mean squared error orders for each ROM and training signal that lead to a smaller maximum mean squared error. From the figure it's clear how using a random signal for training purpose leads to an error of the order of 10^{-6} for both the generalized aerodynamic forces.

Table 5.3: Relevant parameters of the ROM used in this work

Parameters	**RBF-NN**	**LOLIMOT**
Selection of training data	Random	Random
Set of training data	70%	70%
Radial basis function	Gauss function	/
Sigma-range	$10^{-2} \div 10^{6}$	/
k_σ	/	$\frac{1}{3}$
Splitting ratio	/	2
LLM	/	5

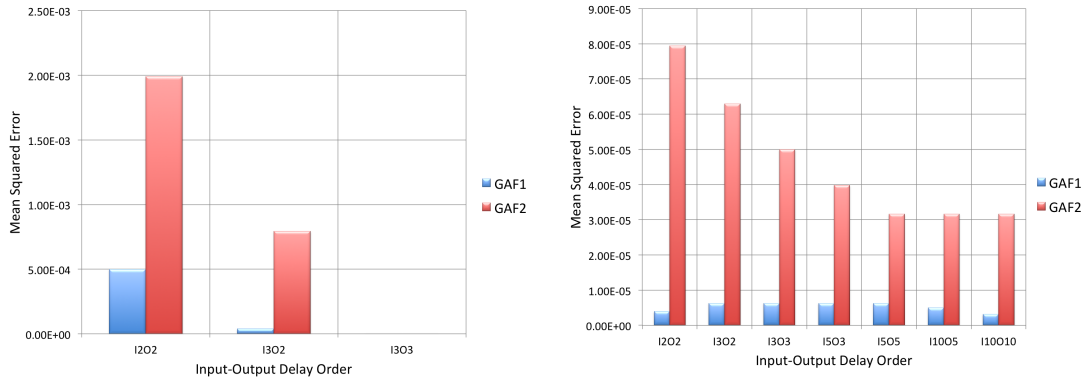

(a) RBF-ROM mean squared error

(b) LOLIMOT-ROM mean squared error

Figure 5.13: Maximum mean squared error relative to the input-output delay order chosen for a ROM trained with the APRBS signal

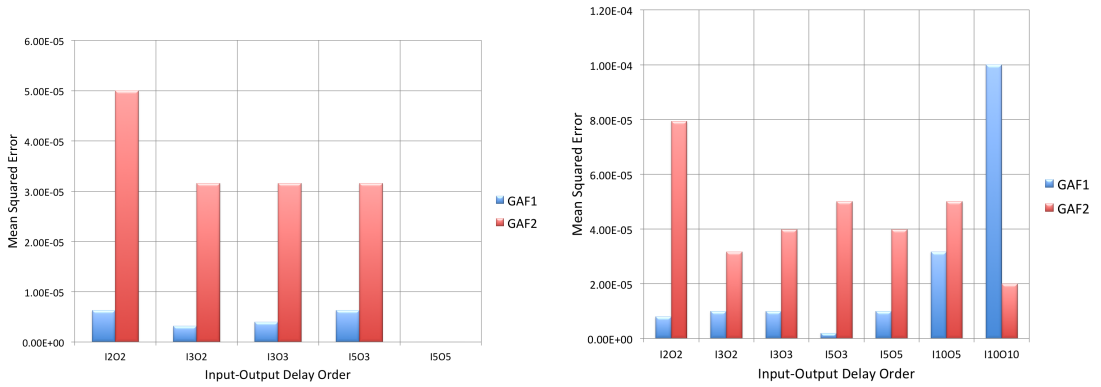

(a) RBF-ROM mean squared error (b) LOLIMOT-ROM mean squared error

Figure 5.14: Maximum mean squared error relative to the input-output delay order chosen for a ROM trained with the random sinusoidal signal

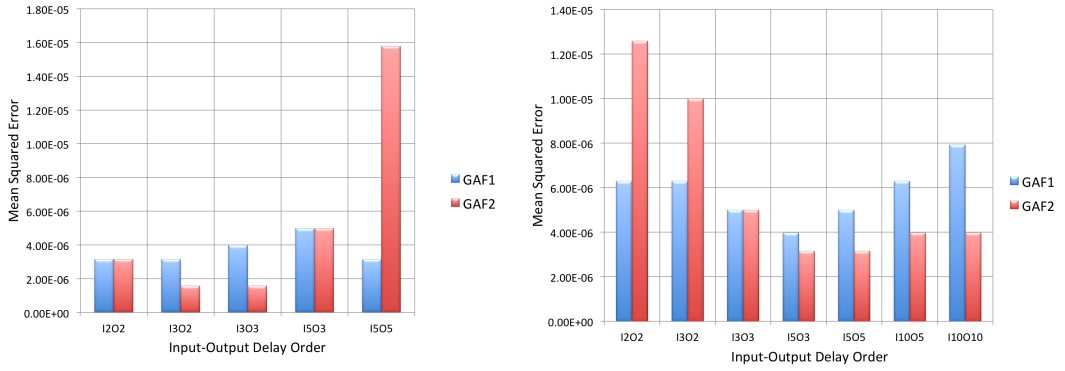

(a) RBF-ROM mean squared error (b) LOLIMOT-ROM mean squared error

Figure 5.15: Maximum mean squared error relative to the input-output delay order chosen for a ROM trained with the random signal

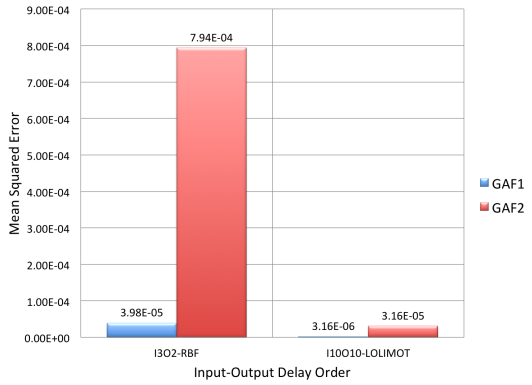

(a) ROM trained with the APRBS signal

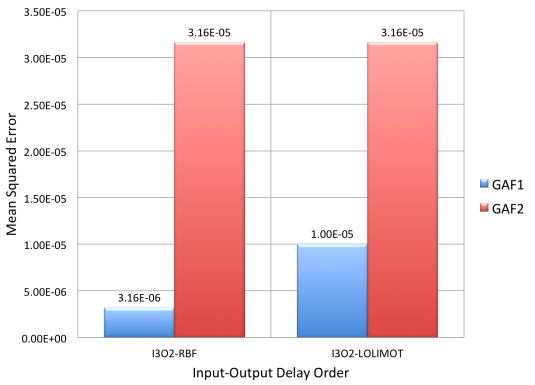

(b) ROM trained with the random sinusoidal signal

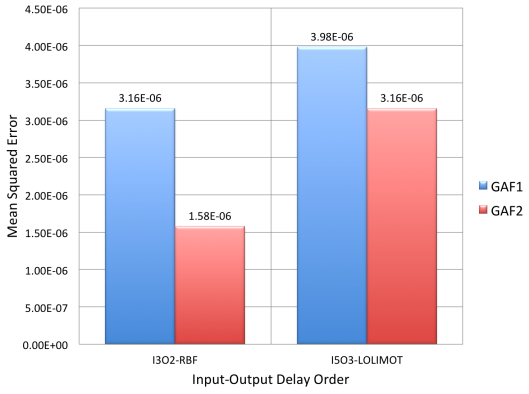

(c) ROM trained with the random signal

Figure 5.16: Maximum mean squared error relative to the optimal input-output delay order chosen for the either ROM

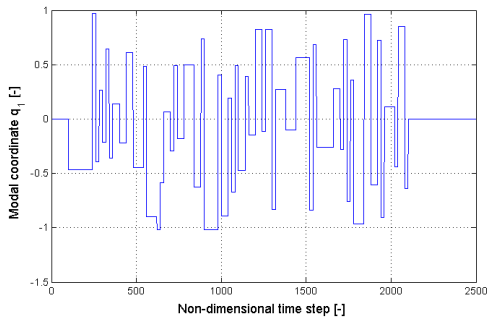

(a) APRBS signal for the first modal displacement

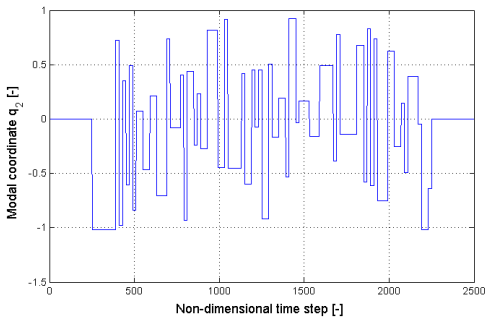

(b) APRBS signal for the second modal displacement

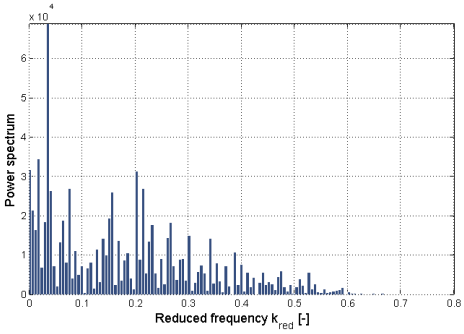

(c) APRBS PSD for the first modal displacement

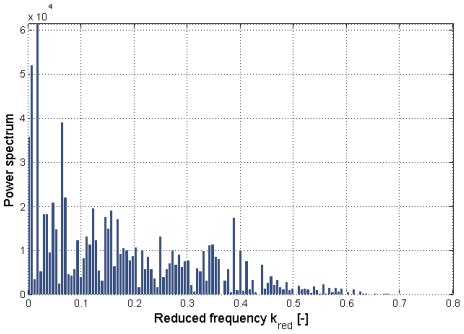

(d) APRBS PSD for the second modal displacement

Figure 5.17: APRBS training signal

5.4.1 APRBS Training

As suggested by Nelles [27] and Winter and Breitsamter [22], the first training signal selected is the APRBS. For the MIMO model there are two different inputs that represent the first and the second modal displacement. Figure 5.17 shows the two modal displacements and the relative PSD. From the figure it can be seen how the reduced frequency of both displacements is chosen in the range between 0 and 0.7 in order to decrease the computational effort and involve the reduced frequencies of the undamped NLR7301 aerofoil.

The APRBS signal has been used to train both the reduced order models chosen in this work. Figure 5.18 shows the response of the system of the two generalized aerodynamic forces for the RBF-ROM trained with an APRBS signal and tested

with the same signal. Instead, Figure 5.19 depicts the response of the LOLIMOT-ROM. In this case, the LOLIMOT-ROM shows better agreement for the trained system for both the generalized aerodynamic forces, as it was demonstrated previously in Figure 5.13. This should suggest a better approximation of the results during the validation phase.
In order to verify that the system has been well trained and hence verify the capacity of the APRBS to be a good training signal for a dynamic system, the reduced order models have been tested with the three different signals proposed in chapter 3. The three signals that have been built for the 2-DOF model are shown in Figure 5.20, 5.21 and 5.22. The reasons for the choice of these three signals have already been explained in chapter 3. Also here, for all validation signals a reduced frequency k_{red} in the range of the training signal has been assumed in order to allow to the model to approximate the tested signals.

The simple sinusoidal signal with fixed amplitude and frequency has been chosen as the basis to validate the ROM. In this manner it is possible to understand if the model has been trained accurately for the purpose of this work, see Figure 5.23. Both models can approximate the first generalized aerodynamic force $f_{gen,1}$ well, whereas for the second generalized aerodynamic force $f_{gen,2}$ the model appears less fit to approximate the results obtained by the AER-Eu CFD simulations.
More problems occur if the model is tested with a signal that changes both the amplitude and the frequency, like the *generic signal* and the *random/turbulence signal*. Figure 5.24 and 5.25 show the response of the system tested with these signals.
Studying the response of the two models employed here and trained with the APRBS, it is possible to see how the LOLIMOT-ROM model is more stable than the RBF-ROM and has the capacity to approximate the results of the CFD better.

5.4.2 Random Sinusoidal Signal Training

In this work it has been chosen to build a *random sinusoidal signal* for training purpose insofar as this signal has the property to change both the frequency and

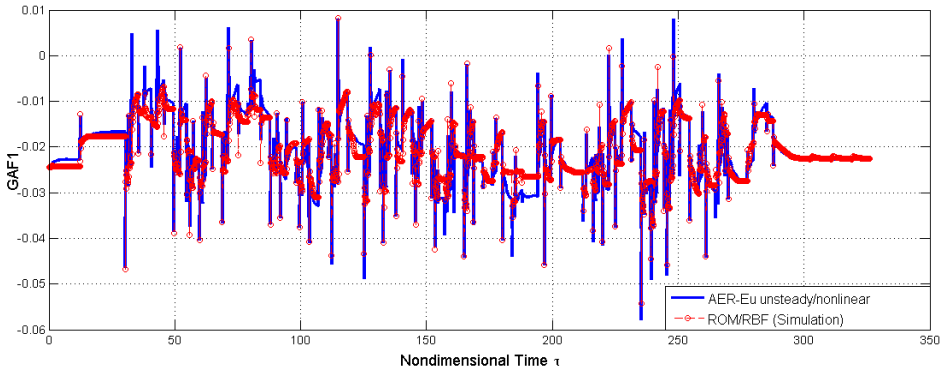

(a) $f_{gen,1}$ for the APRBS signal response

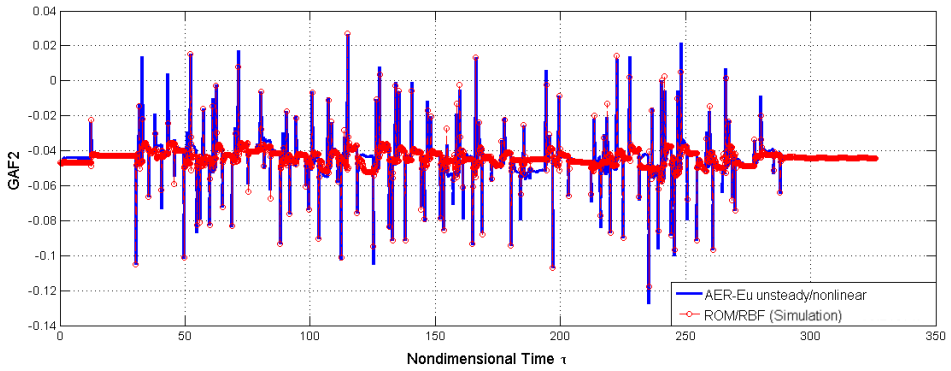

(b) $f_{gen,2}$ for the APRBS signal response

Figure 5.18: Simulation of the system using the RBF-ROM trained with the APRBS

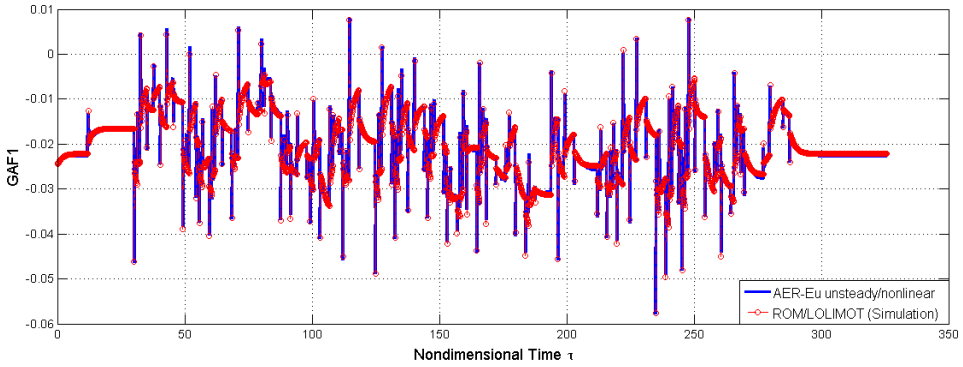

(a) $f_{gen,1}$ for the APRBS signal response

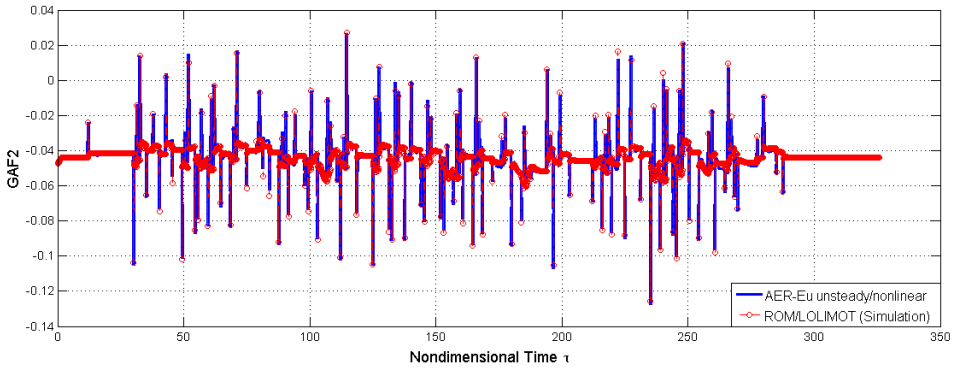

(b) $f_{gen,2}$ for the APRBS signal response

Figure 5.19: Simulation on the system using the LOLIMOT-ROM trained with the APRBS

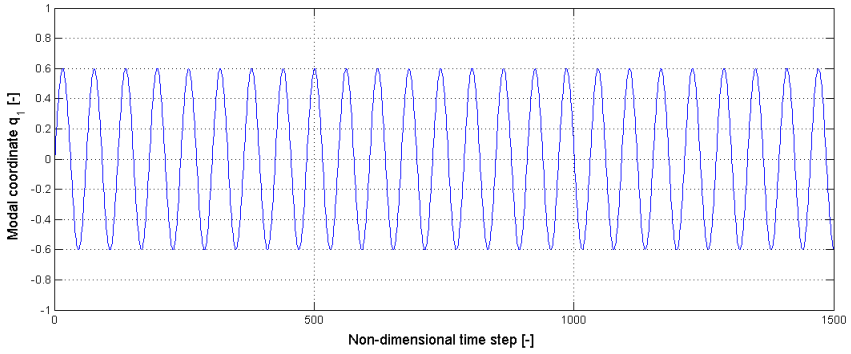

(a) Sinusoidal signal for the first modal displacement

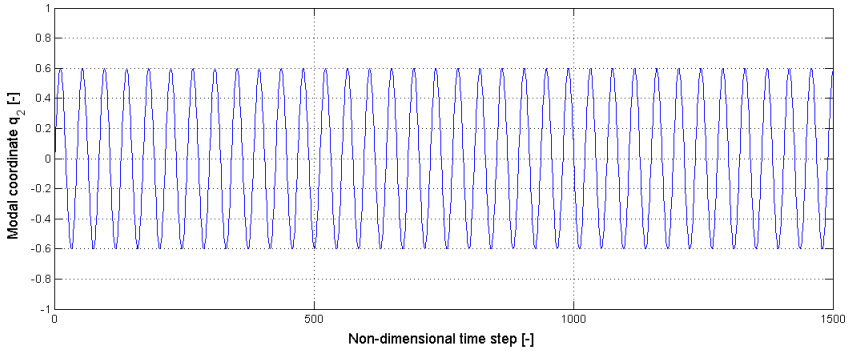

(b) Sinusoidal signal for the second modal displacement

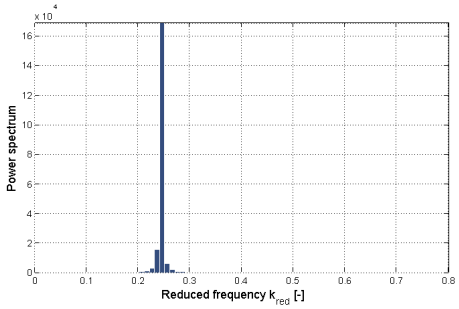

(c) Sinusoidal PSD for the first modal displacement

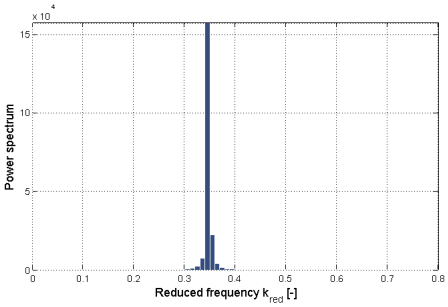

(d) Sinusoidal PSD for the second modal displacement

Figure 5.20: Sinusoidal signal for the modal validation

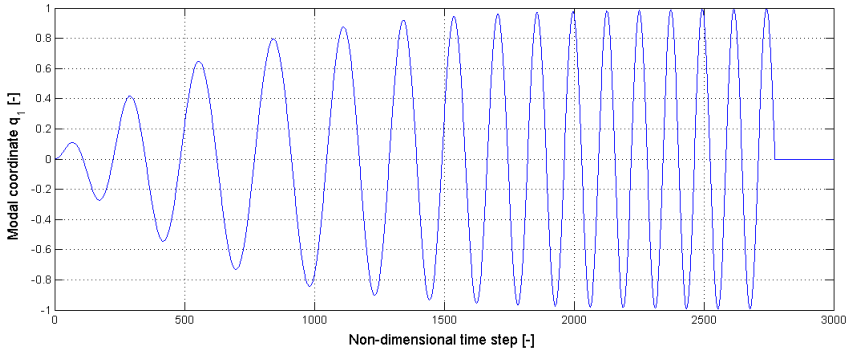

(a) Generic signal for the first modal displacement [21]

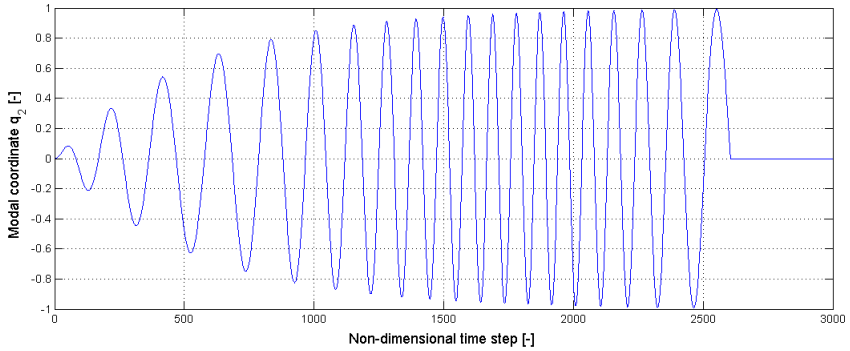

(b) Generic signal for the second modal displacement [21]

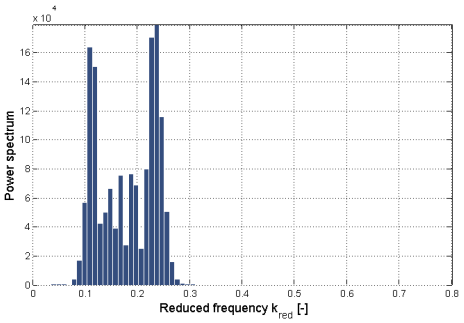

(c) PSD of the generic signal for the first modal displacement

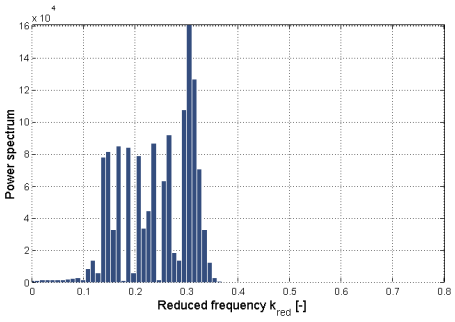

(d) PSD of the generic signal for the second modal displacement

Figure 5.21: Generic signal for the modal validation according to Winter and Breitsamter [21]

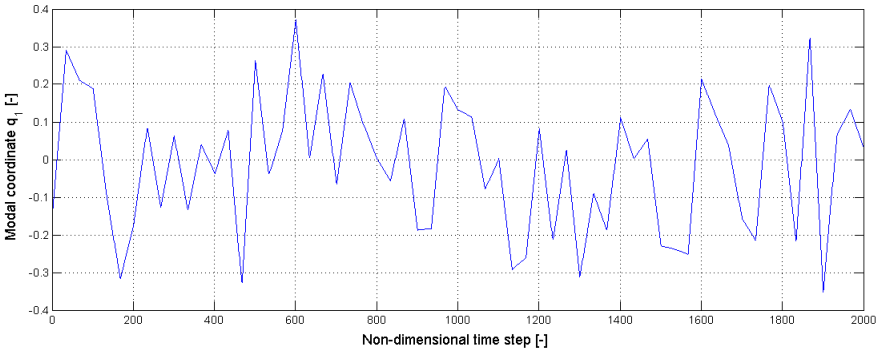

(a) Random signal for the first modal displacement

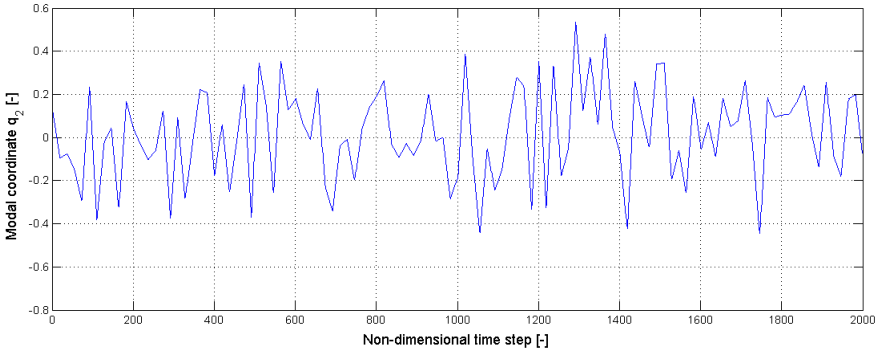

(b) Random signal for the second modal displacement

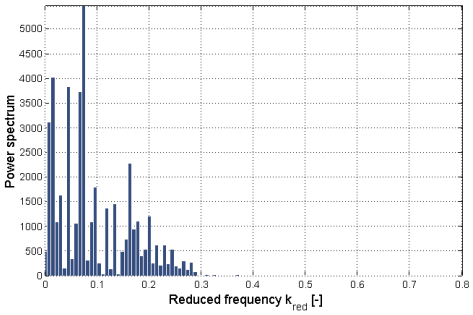

(c) Random signal PSD for the first modal displacement

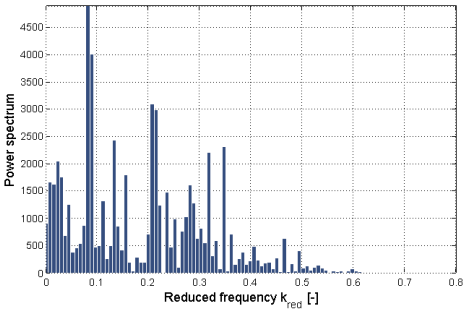

(d) Random signal PSD for the second modal displacement

Figure 5.22: Random signal for the model validation

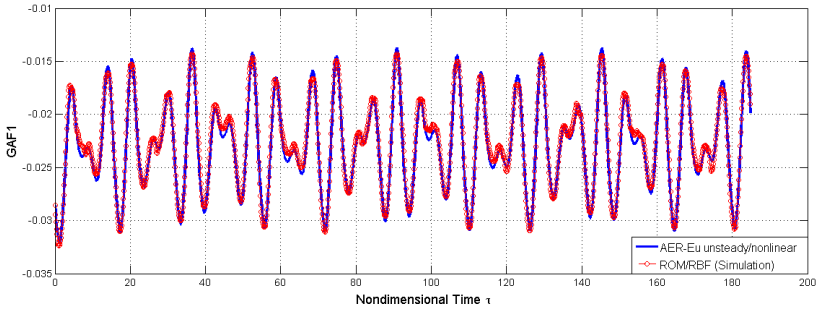

(a) $f_{gen,1}$ of the RBF-ROM

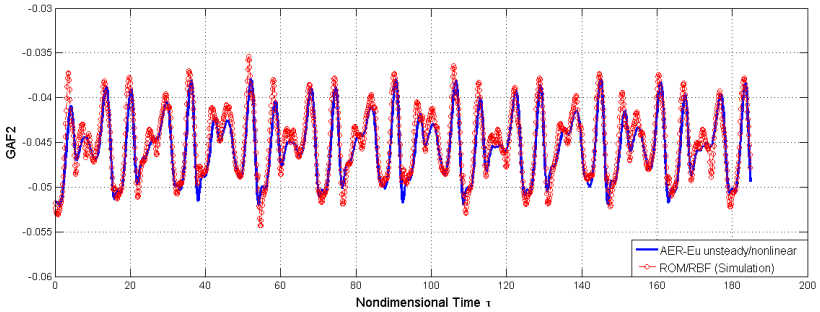

(b) $f_{gen,2}$ of the RBF-ROM

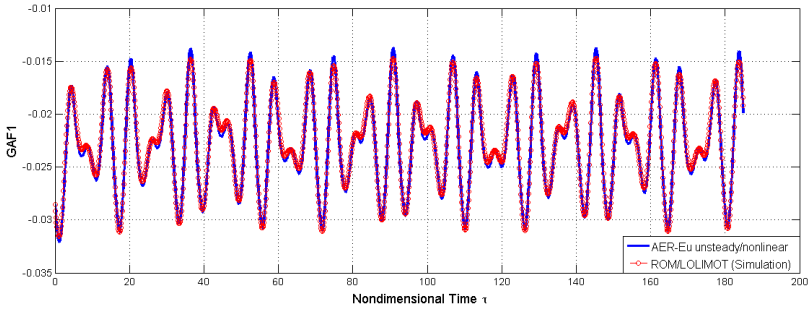

(c) $f_{gen,1}$ of the LOLIMOT-ROM

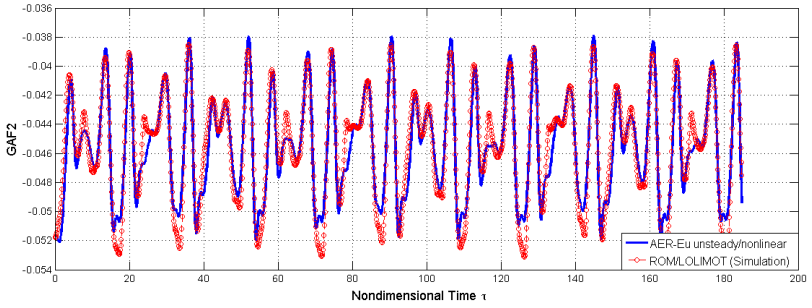

(d) $f_{gen,2}$ of the LOLIMOT-ROM

Figure 5.23: Response of the RBF-ROM and LOLIMOT-ROM trained with the APRBS and tested with the *sinusoidal* signal

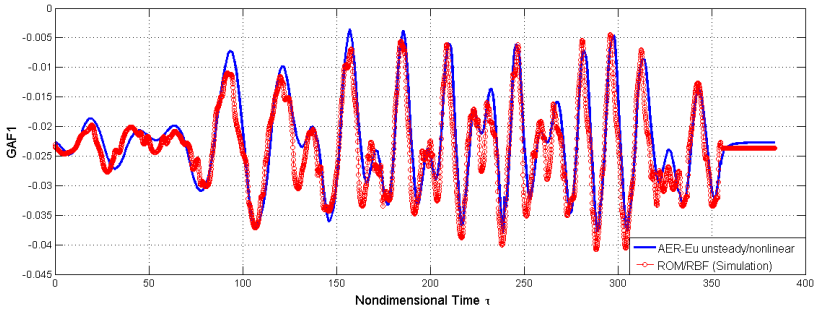

(a) $f_{gen,1}$ of the RBF-ROM

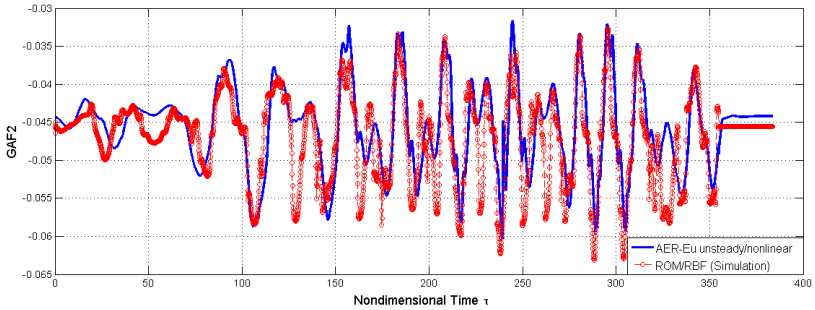

(b) $f_{gen,2}$ of the RBF-ROM

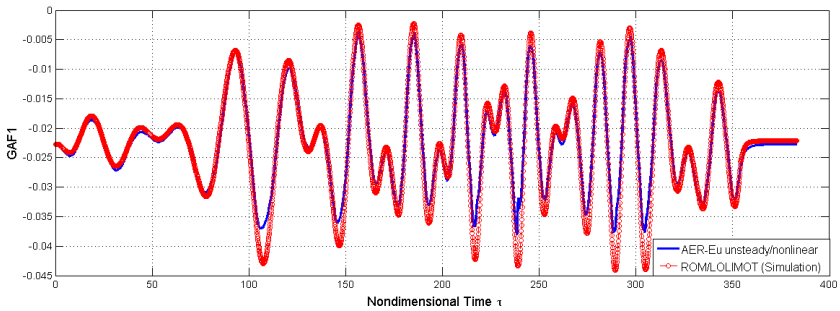

(c) $f_{gen,1}$ of the LOLIMOT-ROM

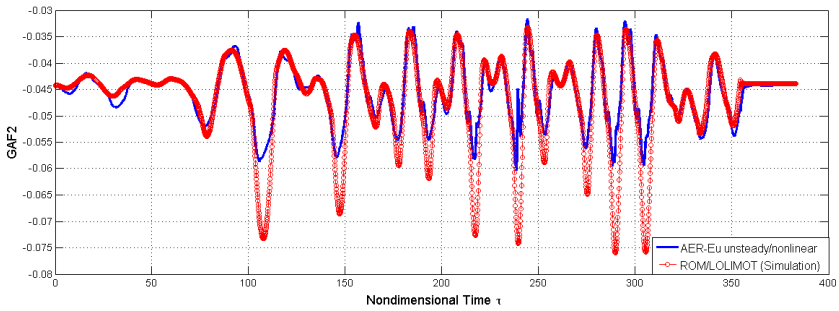

(d) $f_{gen,2}$ of the LOLIMOT-ROM

Figure 5.24: Response of the RBF-ROM and LOLIMOT-ROM trained with the APRBS and tested with the *generic* signal

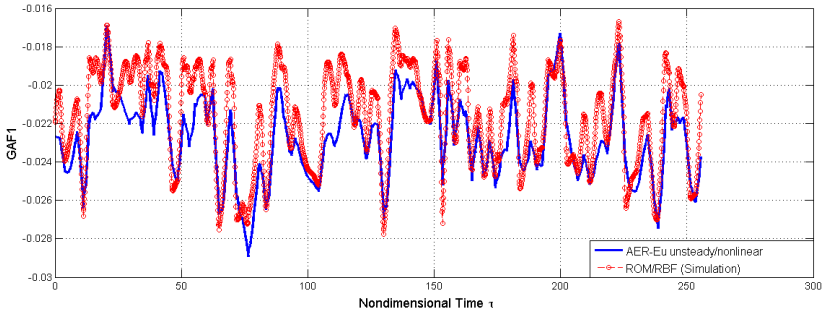

(a) $f_{gen,1}$ of the RBF-ROM

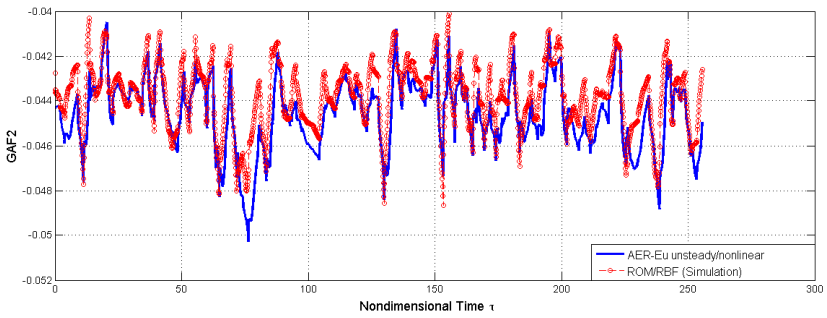

(b) $f_{gen,2}$ of the RBF-ROM

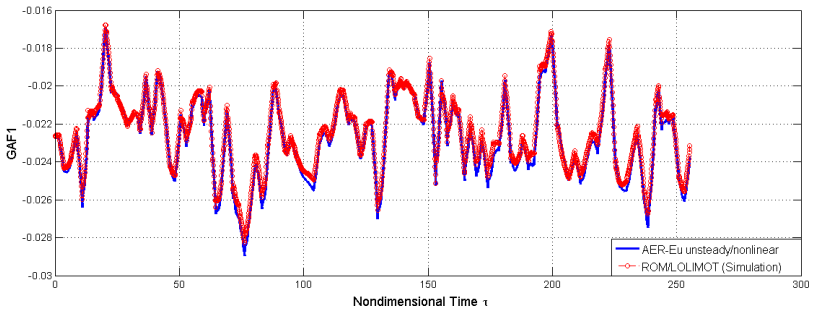

(c) $f_{gen,1}$ of the LOLIMOT-ROM

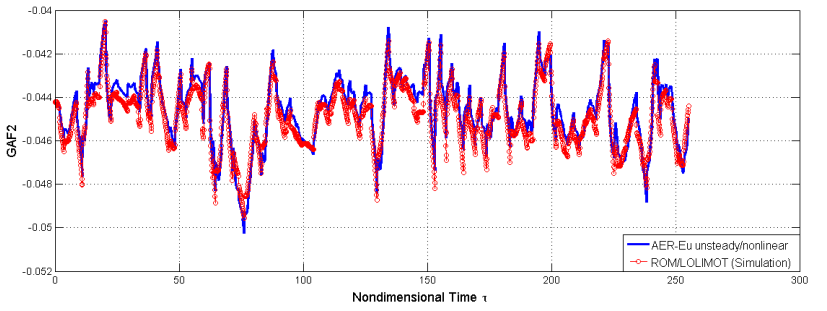

(d) $f_{gen,2}$ of the LOLIMOT-ROM

Figure 5.25: Response of the RBF-ROM and LOLIMOT-ROM trained with the APRBS and tested with the *random/turbulence* signal

the amplitude during its length. This behaviour is of fundamental relevance because the system can be trained for more than one frequency and one amplitude, as in the APRBS. The amount of frequencies and amplitudes inside the signal strictly depends on its length. Here, the length is a trade off between the desired frequencies and amplitudes and the computational effort. Figure 5.26 depicts the random sinusoidal signal and the respective PSD, which is in the range of $k_{red} \in [0, 0.8]$ with a slight difference from the two modal displacements. The frequency of the first modal displacement q_1 is centred around $k_{red,1} = 0.24$, whereas the frequency of the second modal displacement q_2 is centred around $k_{red,2} = 0.34$. Furthermore, this signal has less constant values, like plateaus, compared to the APRBS. Thus, it seems to be more suited for the unsteady problem, because can trained the model with more frequencies and amplitudes in a shorter length saving computational effort.

The simulations on the training signal for the two ROM proposals are depicted in Figure 5.27 and 5.28. As for the APRBS training, the LOLIMOT-ROM is more stable than the RBF-ROM. With the LOLIMOT is possible to use higher input-output delay orders without losing stability. Regardless, in this case the RBF-ROM can better approximate the results from the CFD for both the generalized aerodynamic forces.

The same validation signals used for the APRBS training have been employed here and the results can be seen in Figures 5.29, 5.30, and 5.31.

With the random sinusoidal signal, in relation to the LOLIMOT-ROM, the RBF-ROM approximates extremely well the CFD results of the first generalized aerodynamic forces $f_{gen,1}$ and very well the second generalized aerodynamic forces $f_{gen,2}$. As it is expected, compared to the APRBS training, the random sinusoidal signal gives better results in the approximation of the nonlinear solution.

5.4.3 Random Training

As the random sinusoidal signal, the *random signal* has the property to sweep a broad range of frequencies and amplitudes. The only difference is related to the regularity of the signal. Whereas the random signal presents different thin

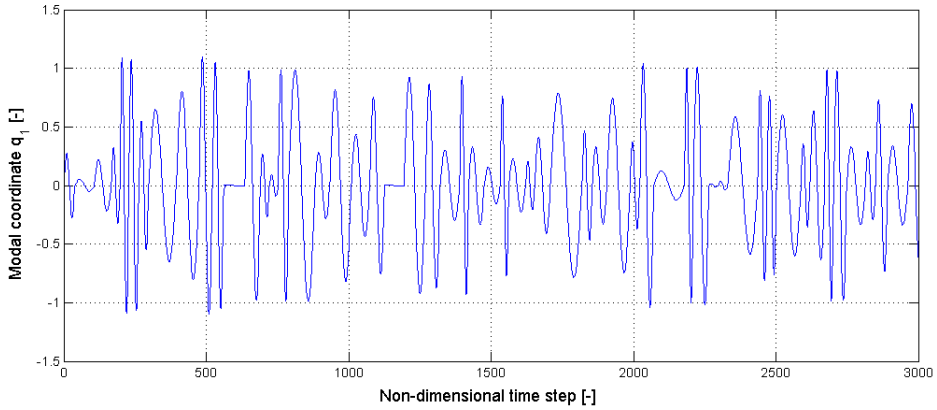

(a) Random sinusoidal signal for the first modal displacement

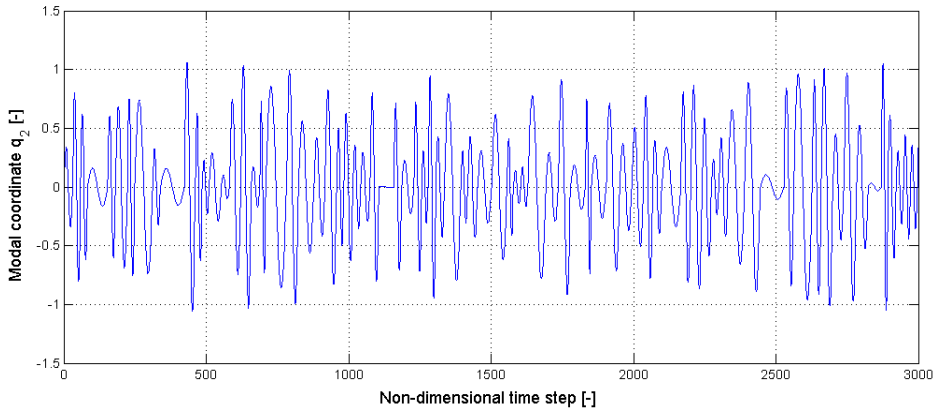

(b) Random sinusoidal signal for the second modal displacement

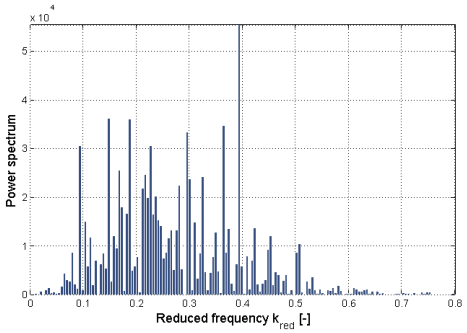

(c) Random sinusoidal signal PSD for the first modal displacement

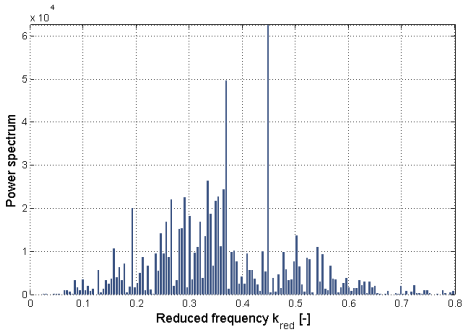

(d) Random sinusoidal signal PSD for the second modal displacement

Figure 5.26: Random sinusoidal training signal

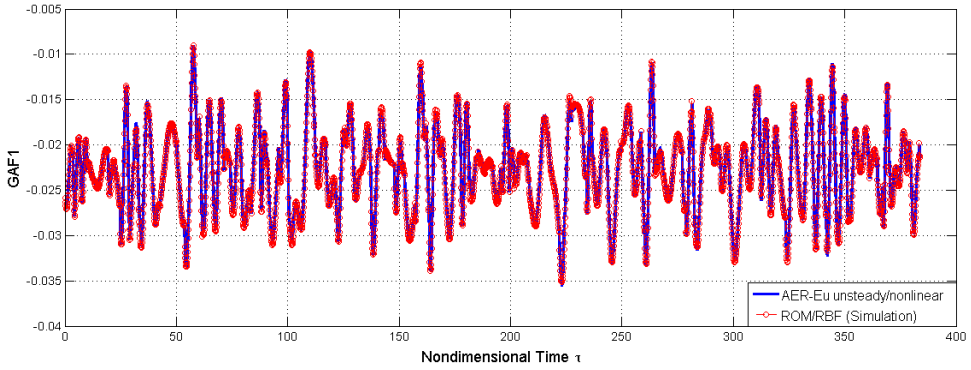

(a) $f_{gen,1}$ for the random sinusoidal signal response

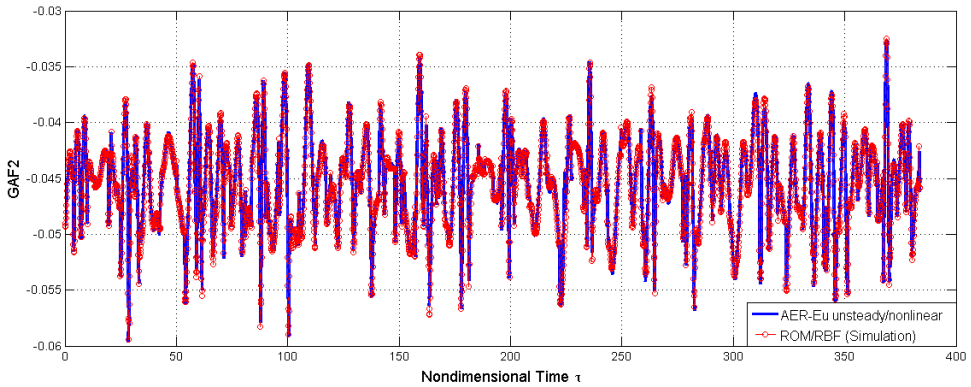

(b) $f_{gen,2}$ for the random sinusoidal signal response

Figure 5.27: Simulation of the system using the RBF-ROM trained with the *random sinusoidal* signal

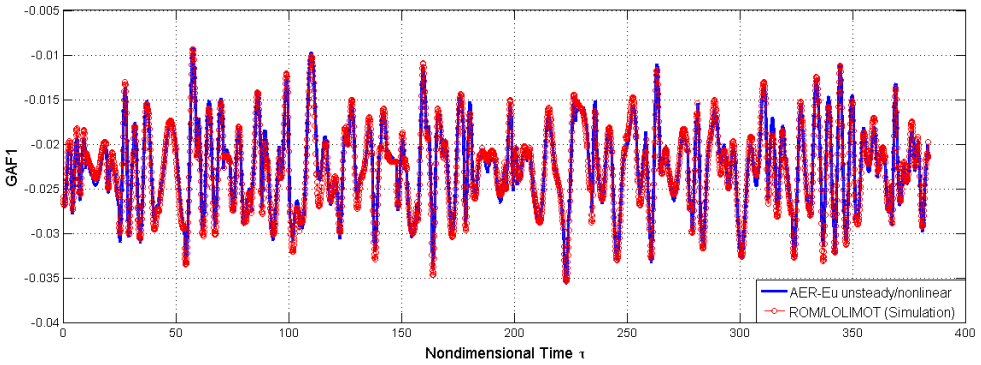

(a) $f_{gen,1}$ for an random sinusoidal signal response

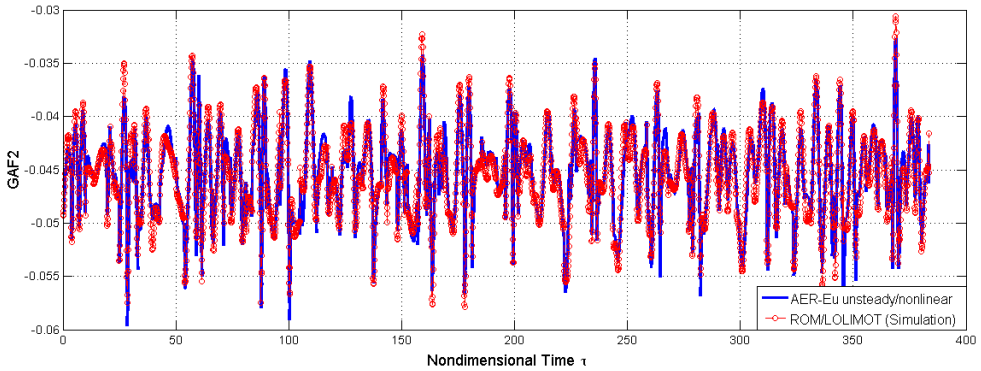

(b) $f_{gen,2}$ for an random sinusoidal signal response

Figure 5.28: Simulation of the system using the LOLIMOT-ROM trained with the *random sinusoidal* signal

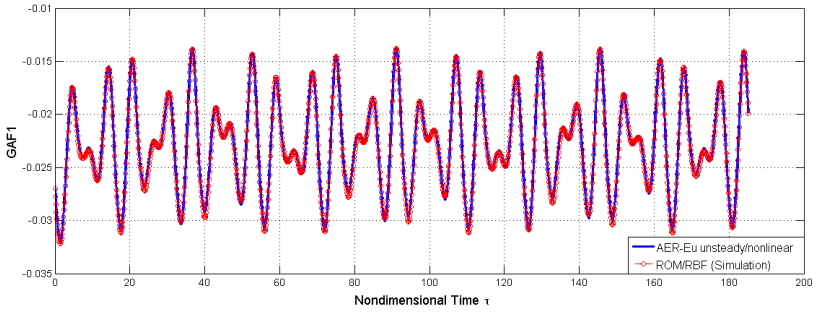

(a) $f_{gen,1}$ of the RBF-ROM

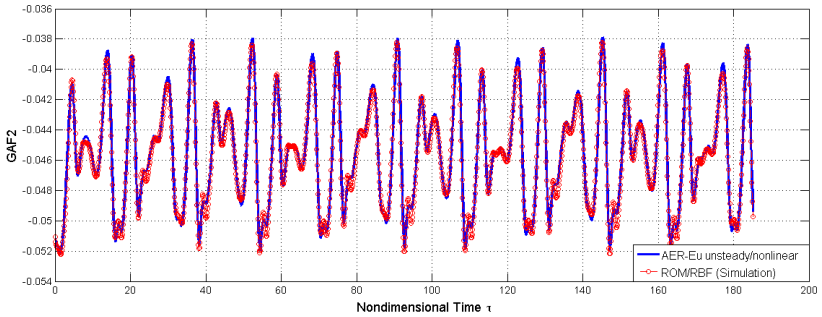

(b) $f_{gen,2}$ of the RBF-ROM

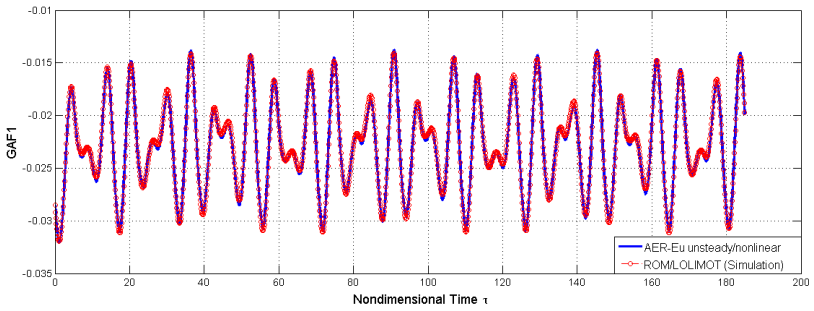

(c) $f_{gen,1}$ of the LOLIMOT-ROM

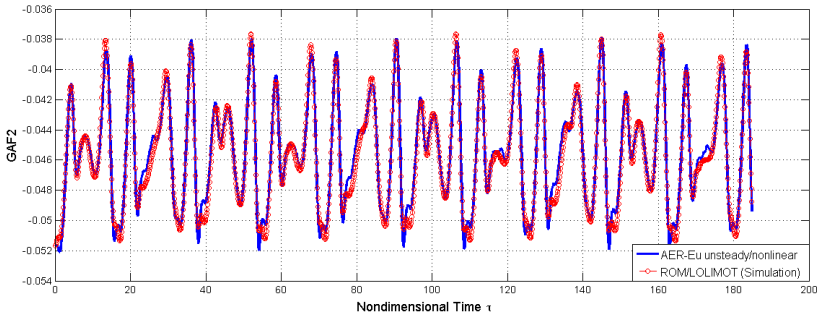

(d) $f_{gen,2}$ of the LOLIMOT-ROM

Figure 5.29: Response of the RBF-ROM and LOLIMOT-ROM trained with the *random sinusoidal* signal and tested with the *sinusoidal* signal

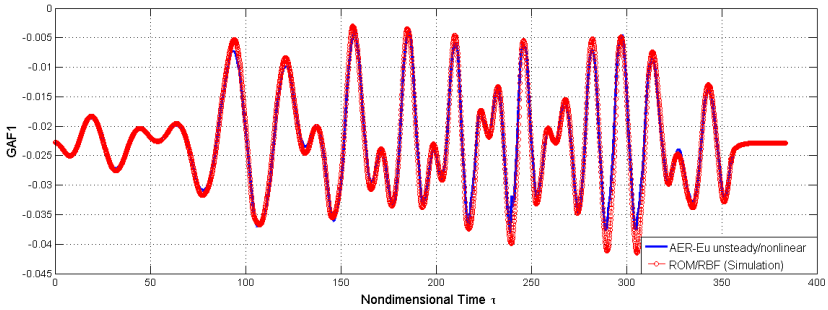

(a) $f_{gen,1}$ of the RBF-ROM

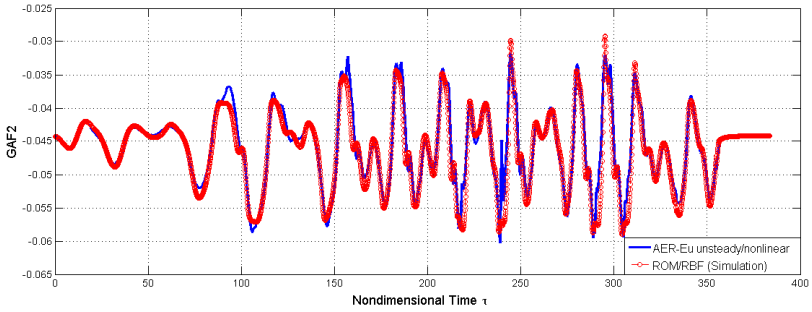

(b) $f_{gen,2}$ of the RBF-ROM

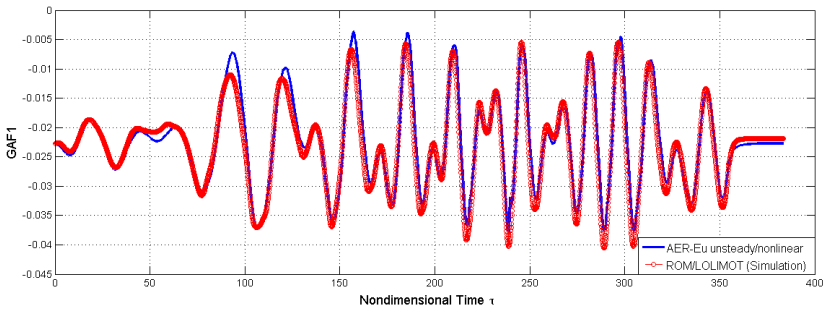

(c) $f_{gen,1}$ of the LOLIMOT-ROM

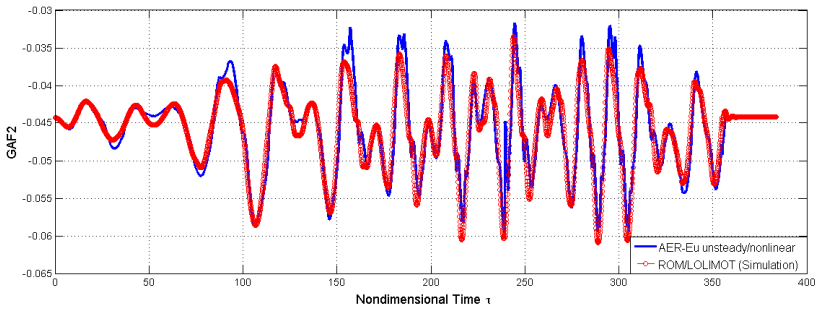

(d) $f_{gen,2}$ of the LOLIMOT-ROM

Figure 5.30: Response of the RBF-ROM and LOLIMOT-ROM trained with the *random sinusoidal* signal and tested with the *generic* signal

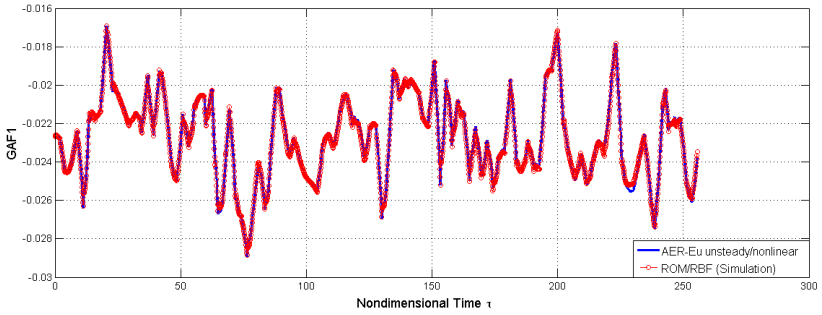

(a) $f_{gen,1}$ of the RBF-ROM

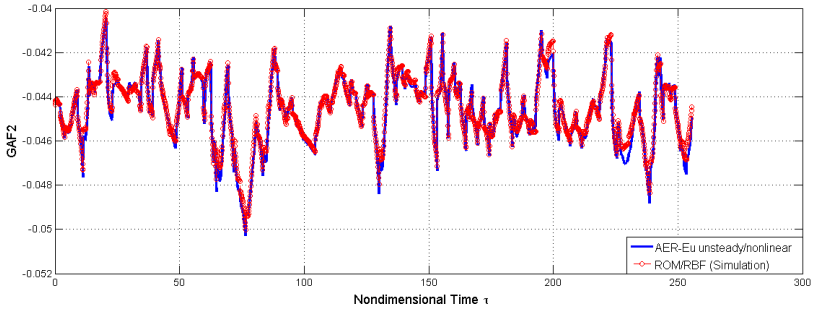

(b) $f_{gen,2}$ of the RBF-ROM

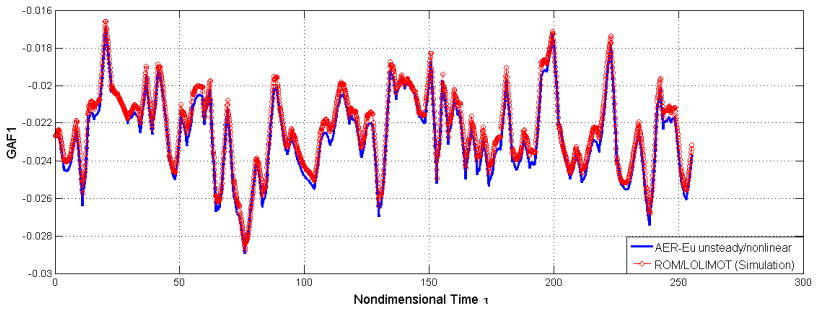

(c) $f_{gen,1}$ of the LOLIMOT-ROM

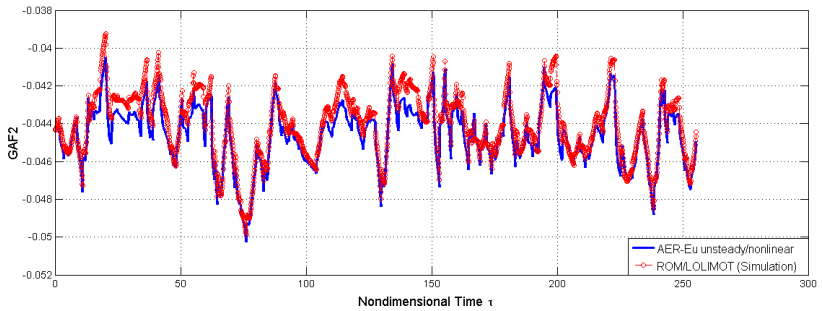

(d) $f_{gen,2}$ of the LOLIMOT-ROM

Figure 5.31: Response of the RBF-ROM and LOLIMOT-ROM trained with the *random sinusoidal* signal and tested with the *random/turbulence* signal

peaks with a corresponding discontinuous derivative, the random sinusoidal signal is smoother, with discontinuity only from a period to another. Here, a trade off between the length of the signal and the computational effort has also been done. For this reason the frequencies employed for the two modal displacements are centered around the natural undamped frequencies of the two eigenmodes. Figure 5.32 depicts the random training signal and the respective PSD.
The reduced frequency of the first modal displacement is in the range of $k_{red,1} \in [0, 0.7]$, whereas for the second mode is in the range of $k_{red,2} \in [0, 0.8]$.

Figure 5.33 and 5.34 depict the response of the system to the training signal respectively for the RBF-ROM and for the LOLIMOT-ROM. In this case both models extremely well approximate the first and the second generalized aerodynamic forces with a maximum squared error of the order of 10^{-6}. Probably, the totally random behaviour of the signal is more suited to approximate the response of the system and using the random signal more frequencies and amplitudes can be introduced in a shorter length.

From Figure 5.35 it can be seen how the RBF-ROM is more suited than the LOLIMOT-ROM to approximate the sinusoidal signal with a model trained with the random signal. Especially, the second generalized aerodynamic forces $f_{gen,2}$ shows better results using the RBF-ROM.
The stability properties of the LOLIMOT-ROM can be seen from Figure 5.36, where the RBF-ROM is unable to approximate all the response of the system due to the instability of the model, even using small order input-output delays. This could depends on the range of frequencies and amplitudes of the random training signal. Certainly, employing a longer signal the system could well approximate the generic signal.
The good behaviours of the ROM trained with a random signal are depicted again in Figure 5.37 for the approximation of the random/turbulence test signal. In this case no instability problems occur and both ROMs can approximate well the CFD results, especially the RBF-ROM.
Hence, a ROM trained with a random signal shows better ability to approximate the correct response of the system and could be used to study a random signal,

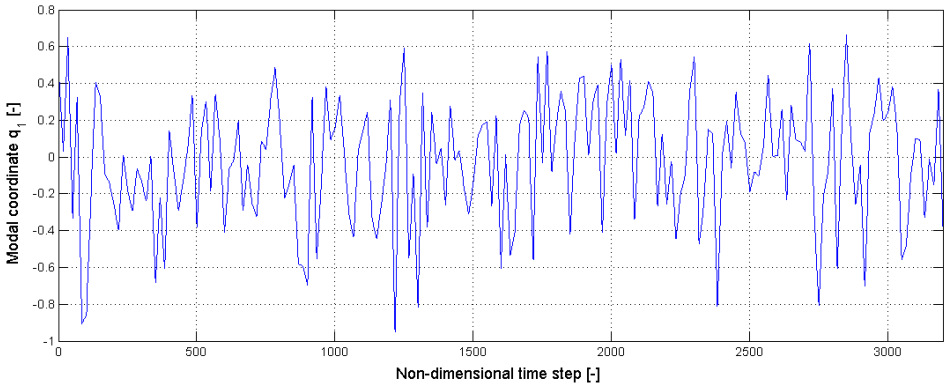

(a) Random signal for the first modal displacement

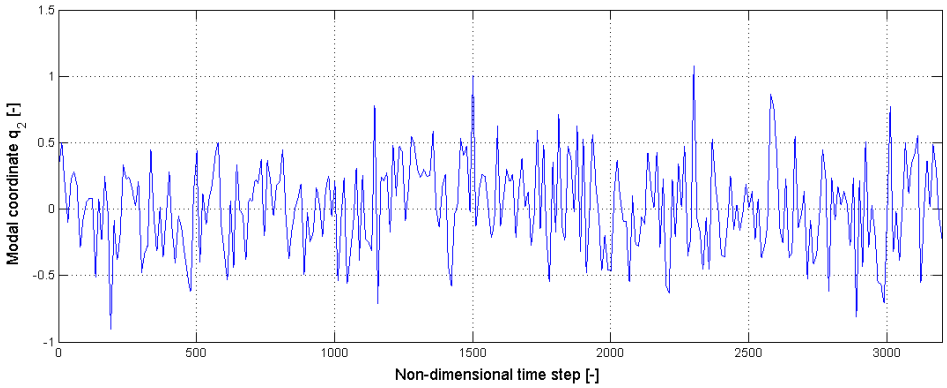

(b) Random signal for the second modal displacement

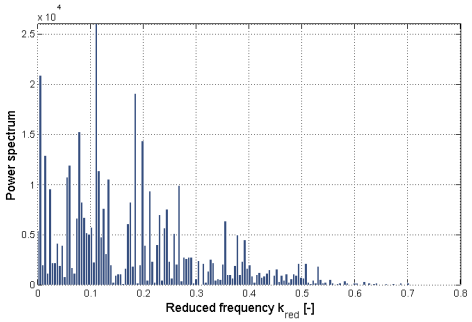

(c) PSD of the random signal for the first modal displacement

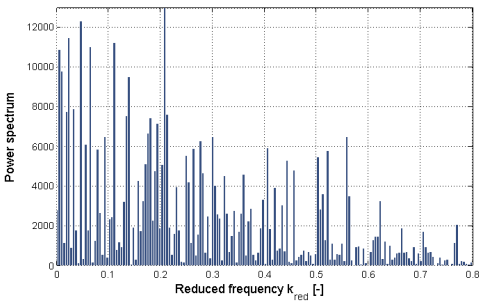

(d) PSD of the random signal for the second modal displacement

Figure 5.32: Random training signal

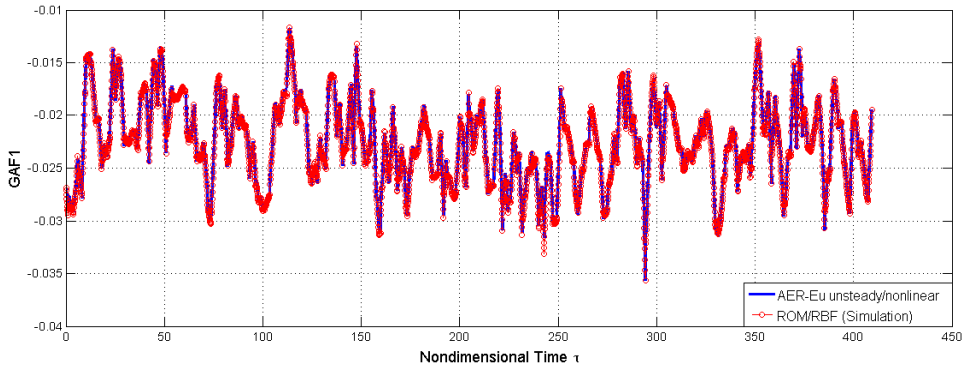

(a) $f_{gen,1}$ for the random signal response

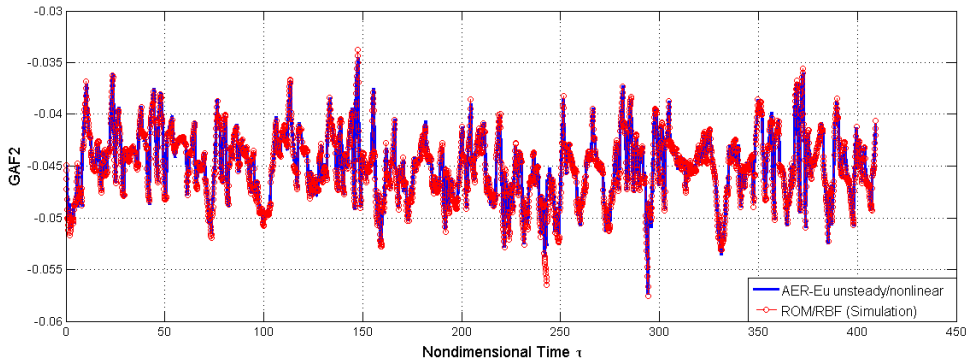

(b) $f_{gen,2}$ for the random signal response

Figure 5.33: Simulation of the system using the RBF-ROM trained with the *random* signal

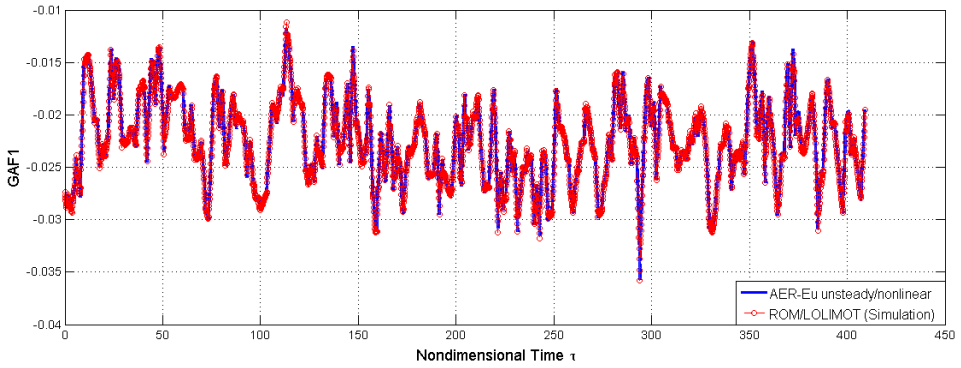

(a) $f_{gen,1}$ for an random sinusoidal signal response

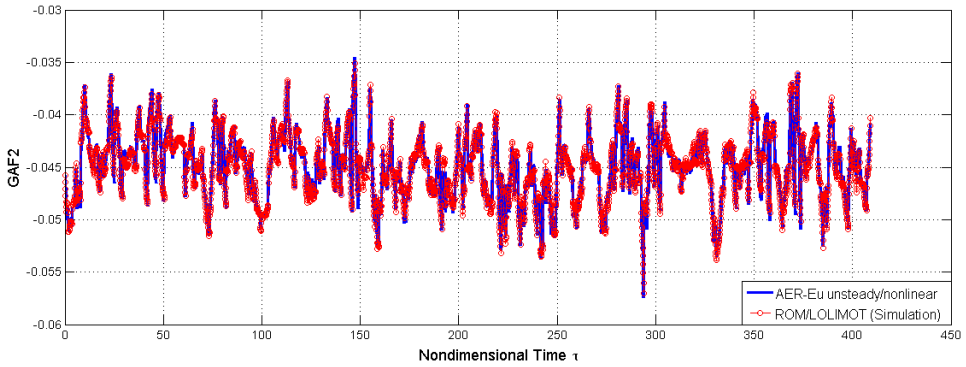

(b) $f_{gen,2}$ for an random sinusoida signal response

Figure 5.34: Simulation of the system using the LOLIMOT-ROM trained with the *random* signal

like a turbulence.

In order to test the potential of the random trained ROM it was decided to use the random sinusoidal training signal as validation signal. This signal is longer than the previous validation signal and hence it contains more frequencies and amplitudes. For these reasons, the approximation of this signal should be a tough task. From Figure 5.38 it is clearly visible how the model can approximate the random sinusoidal signal, even if the random signal has not got smooth peaks. Some errors occur during the approximation of $f_{gen,2}$, but this depends on the frequencies and amplitudes used in the training signal and the trade off for saving the computational effort. Choosing a longer training signal with more information should lead to a better approximation.

The main advantage to employ a reduced order model is the possibility to reduce the computational effort produced by the CFD aerodynamic simulations, maintaining approximately the same accuracy. To obtain the generalized aerodynamic forces and hence the response of the system relative to a specific input signal, a lot of CFD simulations are needed. The computational time to carry out the aerodynamic simulation using the CFD is shown in Table 5.4. The CFD computation has been performed on a computer with an Intel®XEON E3-1220 CPU with 3.10 GHz, 7.7 GB of RAM and a Linux operating system version 2.6.32. This time is relatively low compared to a CFD simulation, which employs the Navier-Stoker equations or a turbulence model. As matter of fact, in this work the Euler equations have been used for solving the aerodynamic problem. Furthermore, the frequency of the employed signal has been set near the undamped natural frequencies of the structural model in order to obtain a shorter signal. All these factors are liable to keep the computational time low. As it is depicted in Table 5.4 and 5.5, using a ROM the computational effort decreases at least of 3 orders of magnitude compared to the same CFD simulation. For example, taking into account the random sinusoidal signal (RSS) simulation, the computational time is of 9916 s with the CFD and only 0.627 s using the RBF-ROM already trained. The time saving is more than 15000 times compared to a standard CFD simulation. Taking into account the time for the training process of the ROM, the total simulation

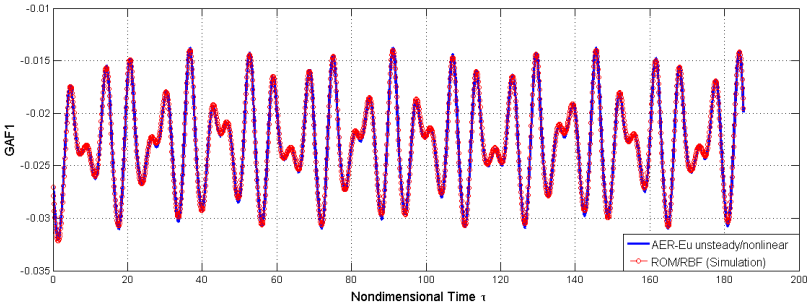

(a) $f_{gen,1}$ of the RBF-ROM

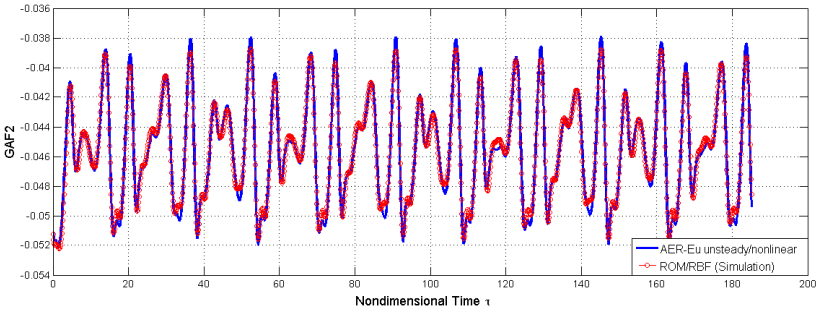

(b) $f_{gen,2}$ of the RBF-ROM

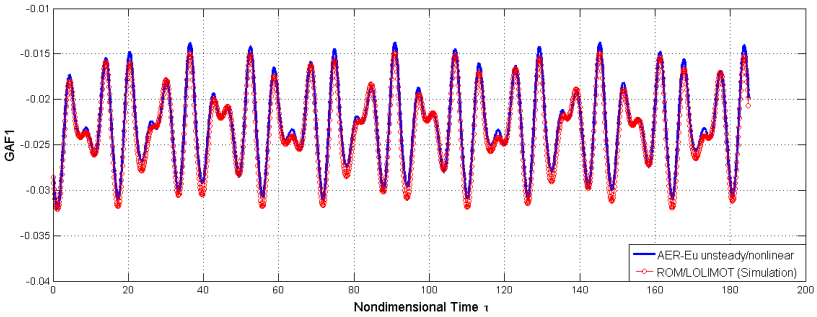

(c) $f_{gen,1}$ of the LOLIMOT-ROM

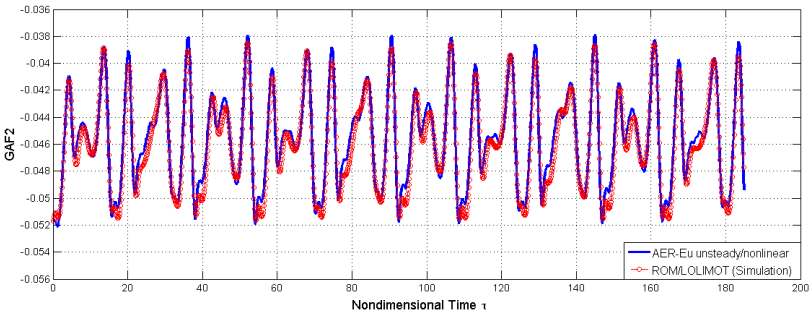

(d) $f_{gen,2}$ of the LOLIMOT-ROM

Figure 5.35: Response of the RBF-ROM and LOLIMOT-ROM trained with the *random* signal and tested with the *sinusoidal* signal

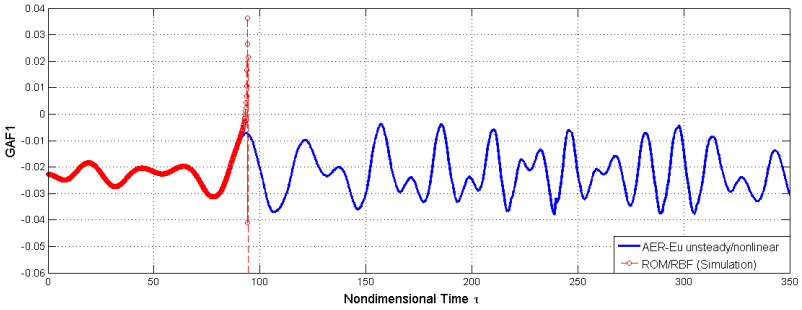

(a) $f_{gen,1}$ of the RBF-ROM

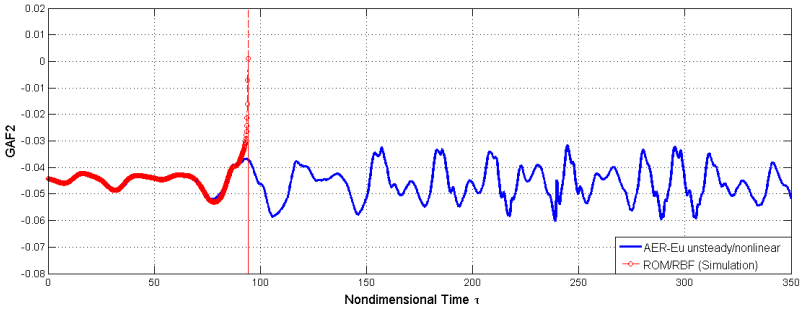

(b) $f_{gen,2}$ of the RBF-ROM

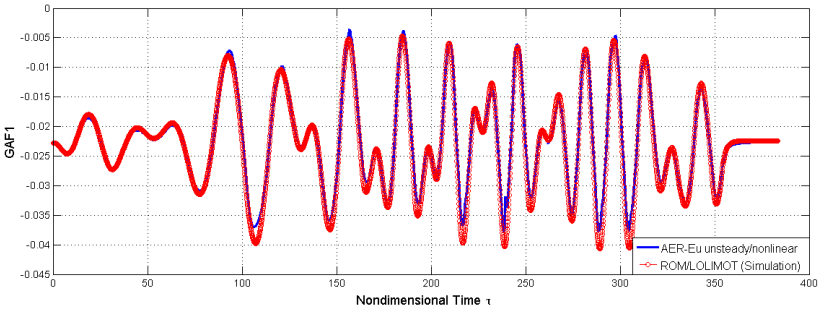

(c) $f_{gen,1}$ of the LOLIMOT-ROM

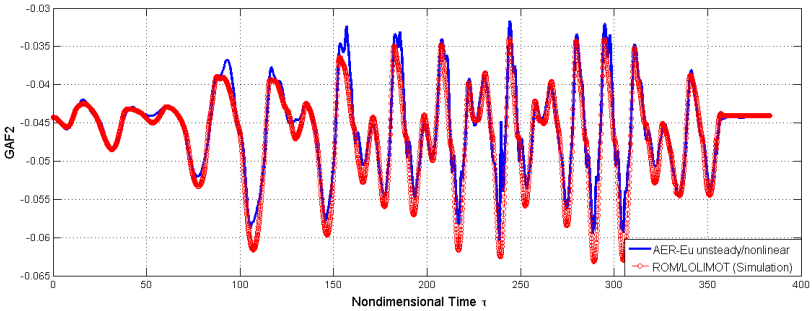

(d) $f_{gen,2}$ of the LOLIMOT-ROM

Figure 5.36: Response of the RBF-ROM and LOLIMOT-ROM trained with the *random* signal and tested with the *generic* signal

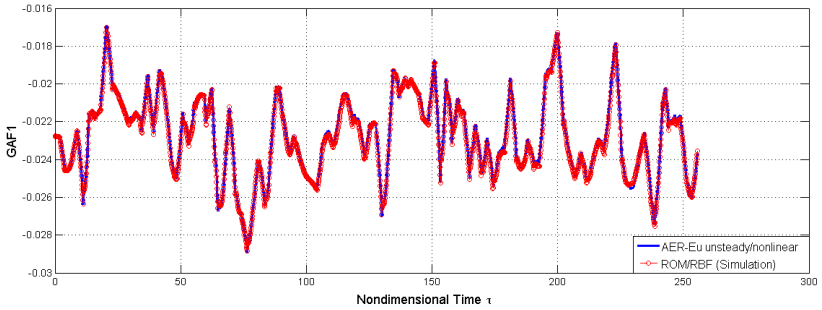

(a) $f_{gen,1}$ of the RBF-ROM

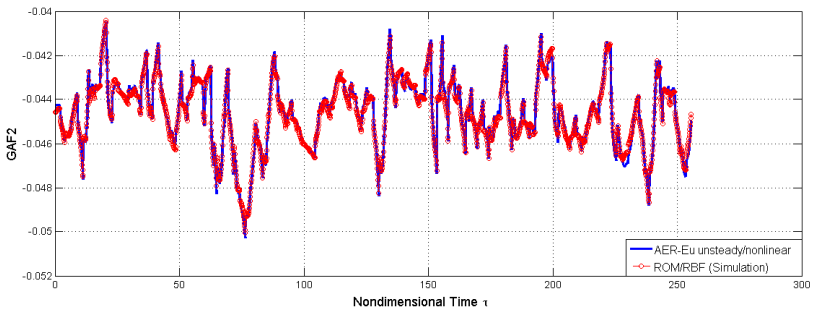

(b) $f_{gen,2}$ of the RBF-ROM

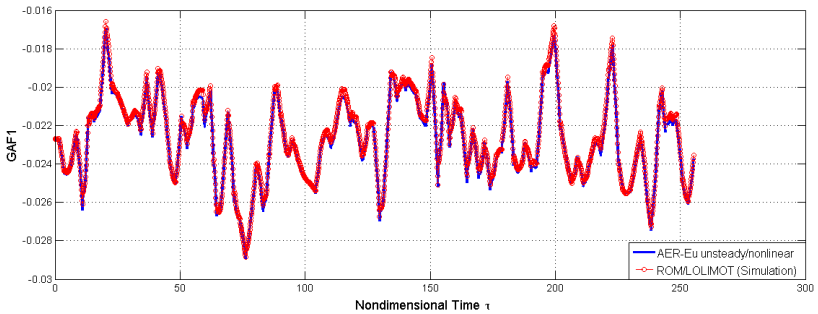

(c) $f_{gen,1}$ of the LOLIMOT-ROM

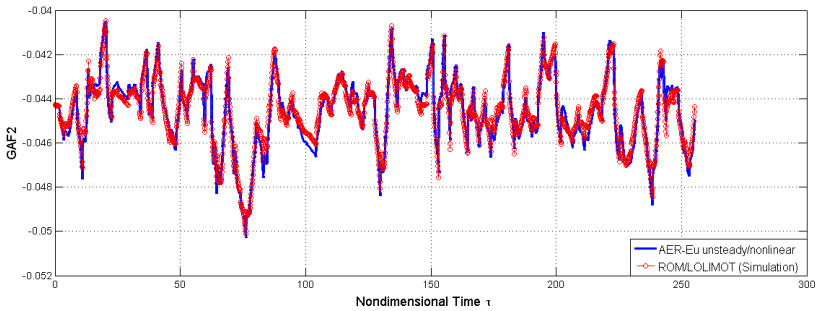

(d) $f_{gen,2}$ of the LOLIMOT-ROM

Figure 5.37: Response of the RBF-ROM and LOLIMOT-ROM trained with the *random* signal and tested with the *random/turbulence* signal

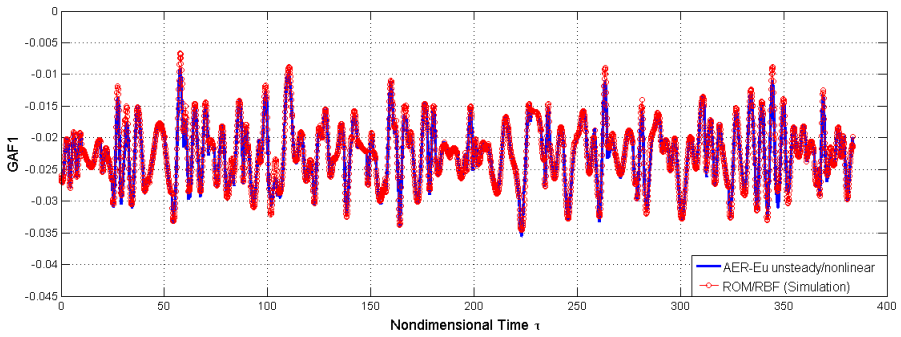

(a) $f_{gen,1}$

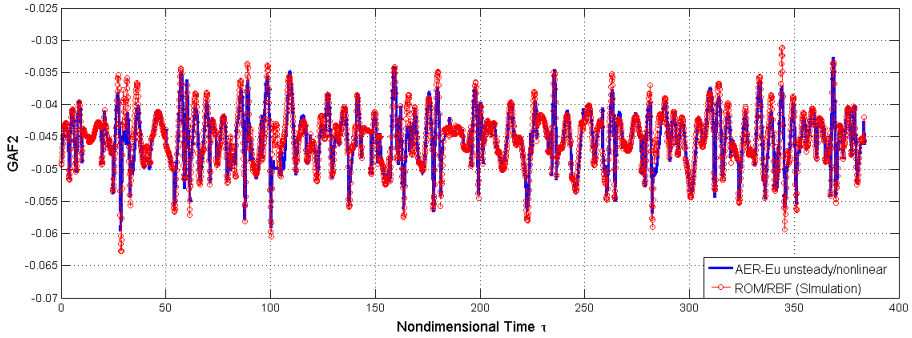

(b) $f_{gen,2}$

Figure 5.38: Response of the RBF-ROM trained with the *random* signal and tested with the *random sinusoidal* signal used previously for the training phase

Table 5.4: CPU simulation time using CFD

Signal	**CFD simulation time (s)**
APRBS	6032
RSS	9916
Random	8995
Sinusoidal	5102
Generic	10846
Random/Turbulence	4921

Table 5.5: CPU time for training and simulation process using a ROM

Signal	**Training time (s)**		**Simulation time (s)**	
	RBF	LOLIMOT	RBF	LOLIMOT
APRBS	15.29	208.55	0.4708	0.9318
RSS	19.45	74.91	0.627	1.0483
Random	18.87	131.39	0.55169	1.365
Sinusoidal			0.9686	1.3926
General			1.04	1.7133
Random/Turbulence			0.8429	1.4

time is approximately 20 s, 495 times faster than CFD. Whereas, comparing the RBF-ROM with the LOLIMOT-ROM Table 5.5 shows that the RBF is approximately 3.75 times faster than the LOLIMOT. Thus, with the LOLIMOT it is possible to achieve more stability, but losing computational effort.

5.5 NLR 7301 Aeroelastic Analysis

In the transonic regime, limit cycle oscillations (LCOs) have been observed in several aircrafts in flight, wind tunnel aeroelastic tests and nonlinear transonic flutter calculations. Wind tunnel flutter tests near the transonic dip at DLR in Göttingen on the NLR7301 supercritical aerofoil have demonstrated the presence of multiple LCOs with different amplitudes, coexisting at the same Mach number and angle of attack [2, 14, 28].

For subsonic regimes, the post-flutter response of the aerofoil is composed by oscillations with grow in time amplitude. On the other hand, for transonic regimes, the amplitude of the oscillations grows since a constant oscillation has been reached due to the displacement of the shock waves which reduces the divergence. It has been observed that the displacement and the change in intensity of the shock waves modify the pressure distribution in a manner that is favourable for the damping response [28]. Hence, as demonstrated by Kousen and Bendiksen [19], post-flutter response presents oscillations with high but steady amplitude.

In this thesis, in order to study the nonlinear response of the system a coupled fluid-structure model based on ROMs has been employed, whose structure has been introduced in chapter 4. Here, only the solutions with the smallest mean squared error, obtained from the ROM, will be used in the coupled system for the aeroelastic analysis. Previously, the potential of the random sinusoidal signal and the random signal has been seen. Thus, it has been chosen to use the ROMs trained with these two signals, so that these models can well capture the nonlinearities of the system.

Hence, the ROM used in the aeroelastic simulation is the RBF-NN trained with a random signal for the nonlinear simulation with $\alpha = 0.0$ deg and with a random sinusoidal signal for the simulation with $\alpha = 0.6$ deg. The RBF-NN has been trained with the OLS procedure employing a delay input order $m = 3$ and a delay output order $n = 2$, whereas the other NN parameters are the same used previously and summarized in Table 5.3. From the following analysis it will be possible to see how both signals can capture the nonlinearities well.

Referring to Tang et al. [20], a transonic LCO at a Mach number of 0.768 in two

Table 5.6: Flow parameters for the aeroelastic analysis in order to compare the results with Tang et al. [20]

Parameters	**Unit**	**Value**
Ma_∞		0.753
α	deg	0.6
V_∞	$m \cdot s^{-1}$	254.7
ρ_∞	$kg \cdot m^{-3}$	1.225
k		1.4
R	$J \cdot kg^{-1} \cdot K^{-1}$	287.0

degrees of freedom is experimentally observed at a free-stream velocity of 254.7 m/s. In Tang et al. [20], in order to use flow conditions, which best meet the wind tunnel conditions in the computations with different flow models, a Mach number of 0.753 and an angle of attack of 0.6 have been chosen. In this work the same parameters used in Tang et al. [20] will be employed only to compare the behaviour of the LCOs and the reliability of the aeroelastic model built in this work and based on ROMs.
A secondary analysis will be exploited using a Mach number of 0.753 and 0.9 with an angle of attack of 0.0°.
Thus, employing a ROM model coupled with a structural model based on the hybrid linear multistep scheme of 2nd order the aeroelastic analysis will be exploited. The HLM of 2nd and 4th order seem to be more stable than the Euler method of 1st order. Thus, the choice to use this kind of algorithm for the coupling.
Table 5.6 shows the flow parameters used in this simulation in order to compare the results with the results obtained in Tang et al. [20], where the CFD-CSD coupled simulation has been used. The results are depicted in Figure 5.39 and are summarized in Table 5.7. These values are further compared with the aeroelastic experimental data of Knipfer et al. [2]. As it can be seen from Figure 5.39, the LCO phenomenon is encountered and the amplitude of the plunge and pitch motions, respectively 12.45 mm and 2.55°, are near those computed in Tang. The

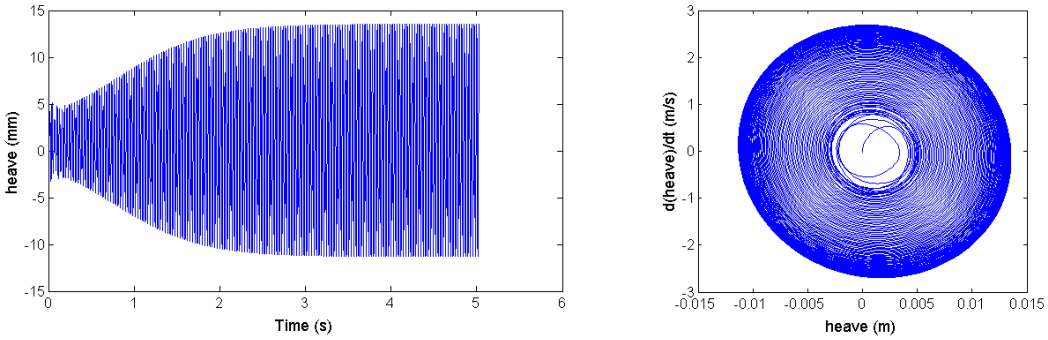

(a) Left: Time series of the heave h motion. Right: Corresponding phase-space representation

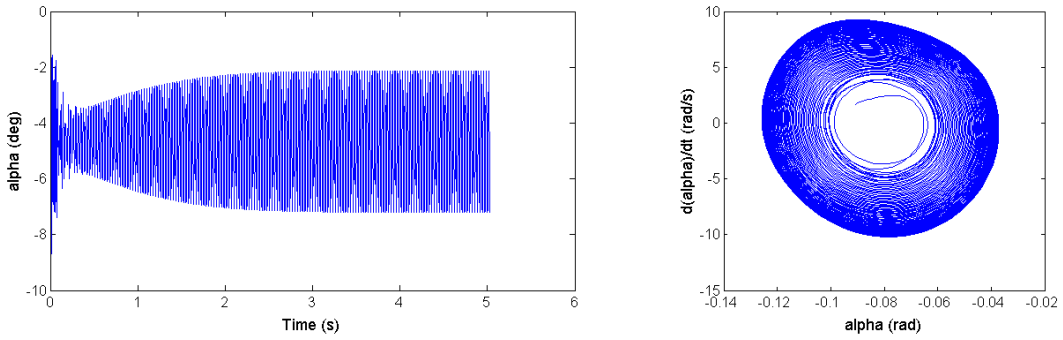

(b) Left: Time series of the pitch α motion. Right: Corresponding phase-space representation

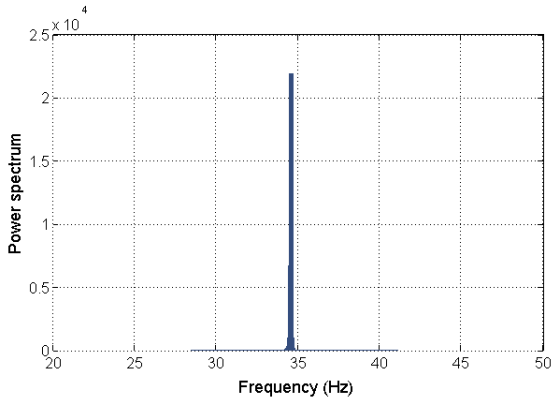

(c) PSD of the heave motion

Figure 5.39: LCO captured during the aeroelastic analysis using $Ma_\infty = 0.753$, $\alpha = 0.6°$ and $V_\infty = 254.7$ m/s

Table 5.7: Results of the aeroelastic simulation using a ROM compared with those obtained in Tang et al. [20] with CFD and Knipfer et al. [2] in the experiment

Simulation	Plunge amplitude a_h (mm)	Pitch amplitude a_α (deg)	Frequency f (Hz)
ROM-HLM2 (thesis)	12.45	2.55	34.5
Single-block grid (Tang et al. [20])	11.2	3.72	34.5
B-L-S-D model (Tang et al. [20])	4	2	32.2
Experiment (Knipfer et al. [2])	0.65	0.18	32.85

heave amplitudes show good agreements with the single-block grid model employed in Tang, whereas they are higher than the amplitudes computed using a turbulent model (B-L-S-D) or with the experimental data. These results agree with those discovered in Tang, where it was shown that the LCO amplitude predicted by the viscous computations is less than $\frac{1}{3}$ of that predicted by the inviscid computation (Euler model). Thus, using a viscous model the LCO amplitude will be limited and the results will be much closer to the experimental data. Although the amplitude of the LCO computed employing a turbulent model is much closer to the experimental data, there is anyway an error of one order of magnitude. This is possible because the wind tunnel wall boundary conditions and the three-dimensional aerodynamic effect are neglected in the computation [20].

Figure 5.39(c) depicts the PSD of the heave/pitch motion. In this case, the predicted frequency of 34.5 Hz shows good agreement with that predicted in Tang. Hence, the reduced model is able to capture the right frequency of the aeroelastic nonlinearities, even using a model with lower degrees of freedom than the full order model used in the CFD computation.

Thus, using a ROM coupled with a structural model it is possible to capture the principal nonlinearities of the system and reduce the computational effort. Indeed, employing this efficient model the elapsed CPU time for the aeroelastic simulation is approximately 20.1 s. Hence, for a whole aerodynamic-aeroelastic analysis, it must take into account the CFD computational time in order to obtain the train-

Table 5.8: LCOs measured using $Ma_\infty = 0.753$, $\alpha = 0.0°$ and increasing the free-stream velocity V_∞

Free-stream velocity V_∞ (m/s)	Plunge amplitude a_h (mm)	Pitch amplitude a_α (deg)
238	8.1	1.88
250	8.9	2.13
280	8.93	2.18

ing signal for the ROM (9916 s), the training and simulation time for the ROM (19.42 s) and the computational time for the coupled system (20.1 s), obtaining a total simulation time of 9955.52 s.

In order to understand the behaviour of the LCOs in the transonic flight regime, several simulations with different parameters have been carried out. The free-stream velocity and the Mach number have been altered to show how the flow parameters can modify the response of the nonlinear system, especially of the LCOs.

In the next simulations the angle of attack will be set to 0.0°.

For a Mach number, $Ma_\infty = 0.753$, the LCOs occur for a free-stream velocity of $V_\infty = V_{LCO}(Ma_\infty = 0.753, \alpha = 0.0) = 238$ m/s, Figure 5.40. Compared Figure 5.39 with Figure 5.40, only a slightly difference in the shape of the captured LCOs can be observed and it depends by the trained signal.

The phase-space representations of the LCO prove how the oscillations of the plunge and pitch motions reach a stable-limited condition.

Using the same flow conditions and increasing the free-stream velocity the amplitude of the heave motion should be increasing, as it is shown in Toumit and Darracq [35]. Thus, in Table 5.8 the increase in amplitude relative to an increment in the free-stream velocity is summarized.

Increasing the free-stream velocity another behaviour occurs. The number of oscillations necessary to reach the LCO depends on V_∞, as it is depicted in Figure 5.41. The higher the free-stream velocity, the faster the limit cycle oscillation is

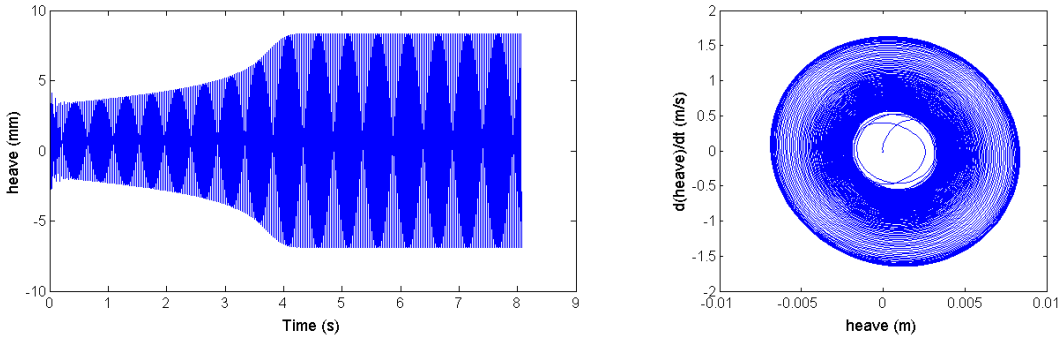

(a) Left: Time series of the heave h motion. Right: Corresponding phase-space representation

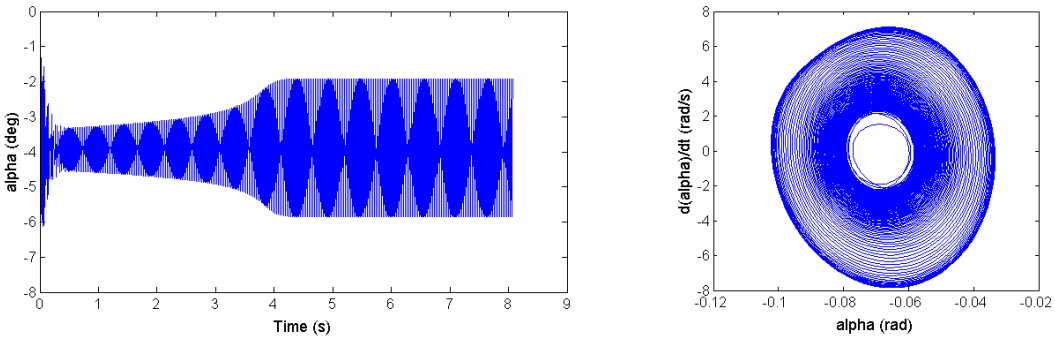

(b) Left: Time series of the pitch α motion. Right: Corresponding phase-space representation

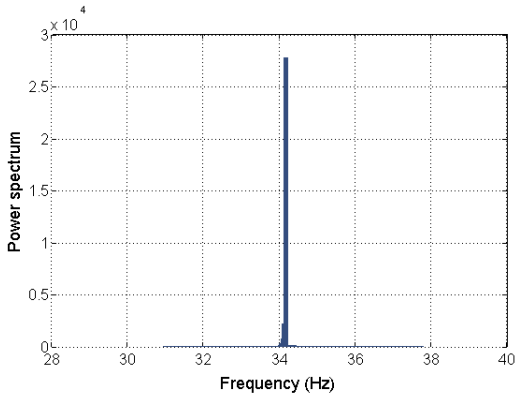

(c) PSD of the heave motion

Figure 5.40: LCO captured during the aeroelastic analysis using $Ma_\infty = 0.753$, $\alpha = 0.0°$ and $V_\infty = 238$ m/s

reached.

Another property of the LCOs is the capacity to follow the self-induced motion even with the introduction of a forced movement. Introducing a pulse movement of the order of 10^{-8} in the state-vector of the plunge/pitch motions the results are shown in Figure 5.42. The results show that the forcing amplitude has no influence on the nature of the response. The movement is always damped for $V_\infty = 210\ m/s < V_{LCO}$ and always divergent to a limit cycle for $V_\infty = V_{LCO} = 238\ m/s$ and $V_\infty = 250\ m/s > V_{LCO}$, even if the disturb is added before the LCO occurs or when the LCOs have already occurred. The amplitude of the impulse in the state-vector, 10^{-8}, is sufficient to induce a change in the plunge/pitch motions to study the response of the aeroelastic system. Choosing an higher amplitude of the impulse, the system becomes unstable due to numerical instability inside the coupled code. Considering Figure 5.42(c) it is possible to see how the LCOs amplitude can be reduced with the introduction of a force. Indeed, in Dietz [13], it has been demonstrated that LCOs can be reduced or removed by the use of electrodynamic exciters belonging to the flutter-control system. Thus, it has been seen that LCOs amplitude can be controlled by relatively small forces.

Because stronger shock waves are encountered at higher Mach numbers, it is advisable to study the properties of the LCOs using a Mach number $Ma_\infty = 0.9$ with the same flow conditions of the previous case. Figure 5.43 and table 5.9 show the properties of the LCOs that occur varying the free-stream velocity. The free-stream velocity that leads to the LCO condition is $V_\infty = V_{LCO} = 255$ m/s, higher than the V_{LCO} with $Ma_\infty = 0.753$. Also in this case the amplitude of the LCOs increases with the increment in the free-stream velocity, Table 5.9.

Compared the LCOs amplitude of the first case, $Ma_\infty = 0.753$, and of the second case, $Ma_\infty = 0.9$, it is noticeable how the amplitude becomes lower when increasing Mach number. When the Mach number is increasing, the shock waves get stronger and their damping effect on the structure motion becomes more effective. A similar property has been showed in Toumit and Darracq [35] for a two degrees of freedom NACA-64010 aerofoil. Thus, the bifurcation diagrams show in Figure 5.44 give the LCO heave amplitude as a function of the free-stream velocity.

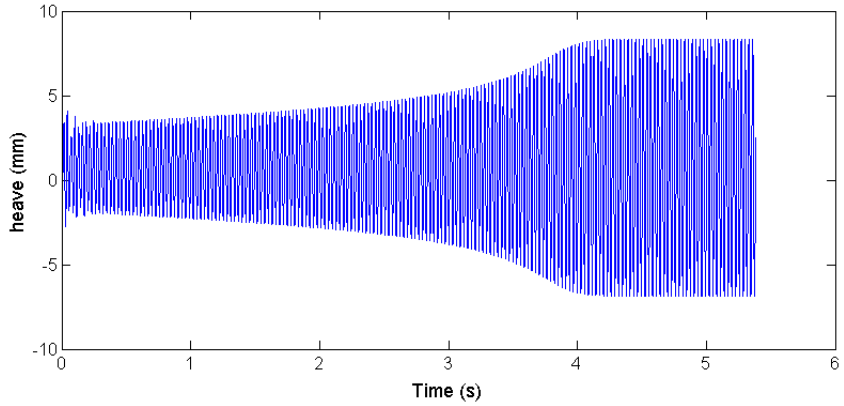

(a) $V_\infty = 238$ m/s

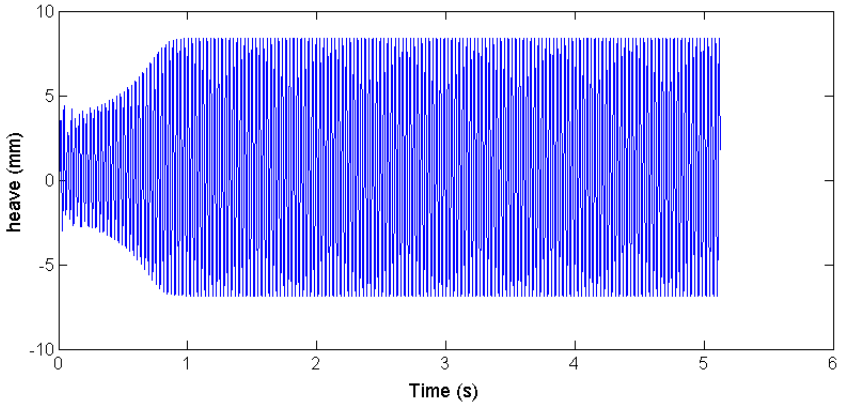

(b) $V_\infty = 250$ m/s

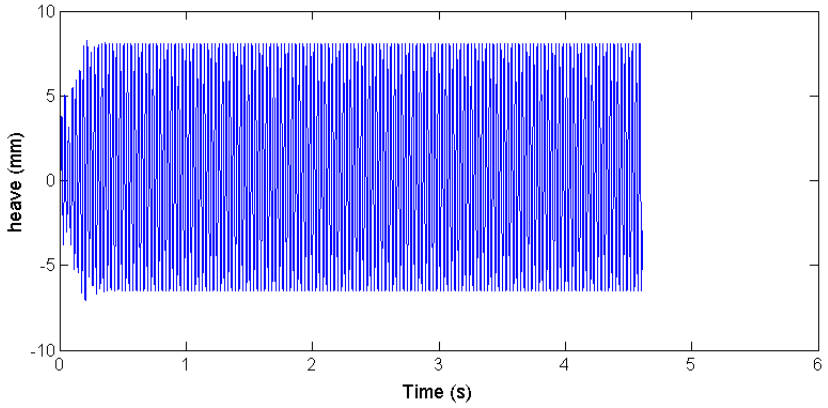

(c) $V_\infty = 280$ m/s

Figure 5.41: Time to reach the LCO condition increasing the free-stream velocity using $Ma_\infty = 0.753$ and $\alpha = 0.0°$

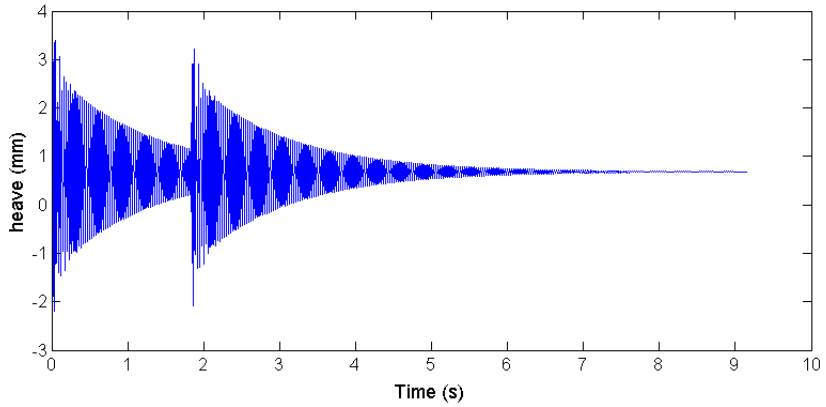

(a) Response of the damped system, $V_\infty = 210$ m/s

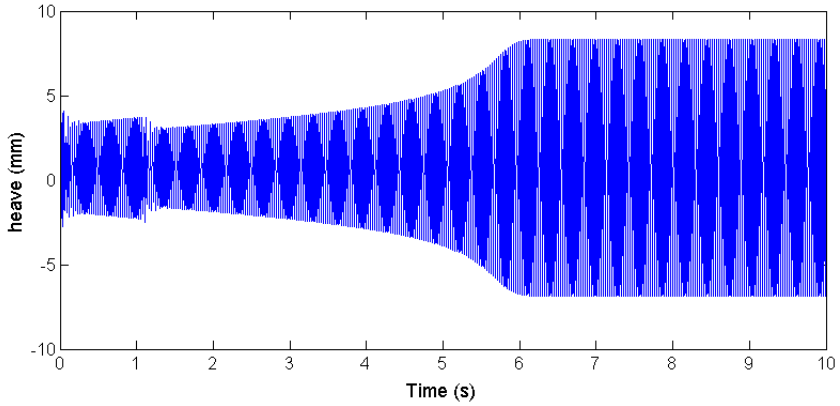

(b) Response of the divergent system, $V_\infty = 238$ m/s

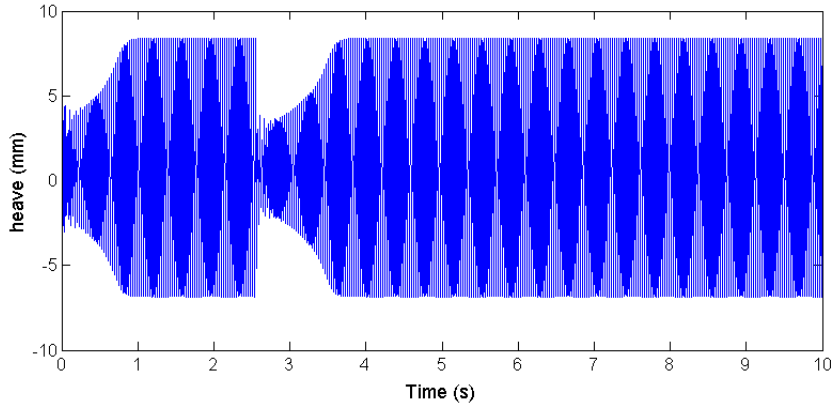

(c) Response of the divergent system, $V_\infty = 250$ m/s

Figure 5.42: Different responses of the heave motion with the introduction of a pulse movement using $Ma_\infty = 0.753$ and $\alpha = 0.0°$

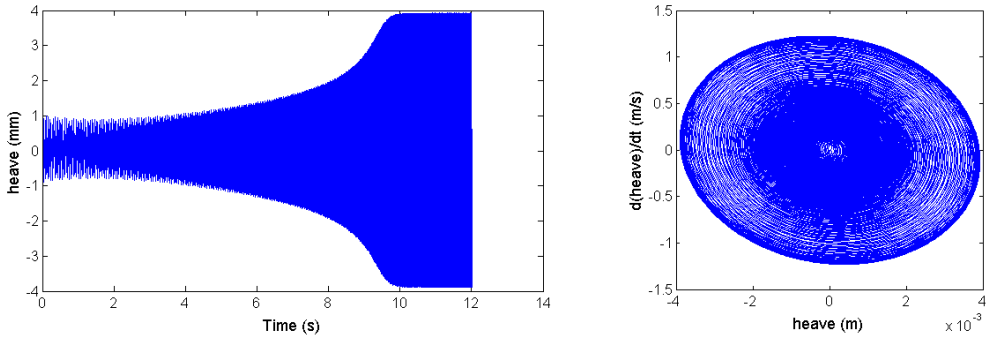

(a) Left: Time series of the heave h motion. Right: Corresponding phase-space representation

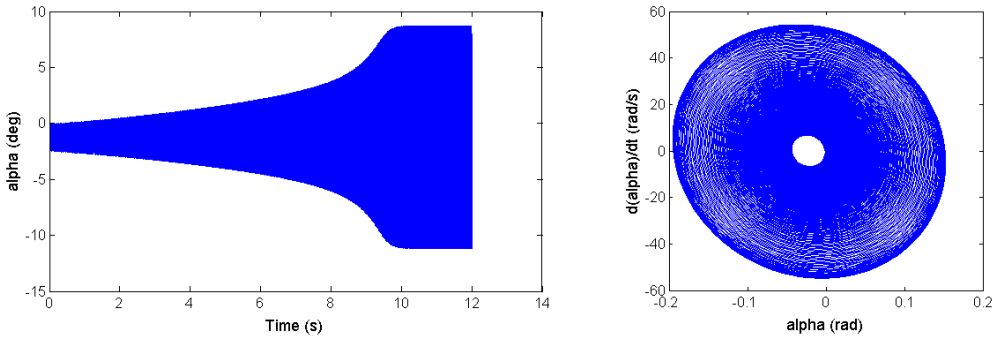

(b) Left: Time series of the pitch α motion. Right: Corresponding phase-space representation

Figure 5.43: LCO captured during the aeroelastic analysis using $Ma_\infty = 0.9$, $\alpha = 0.0°$ and $V_\infty = 255$ m/s

Table 5.9: LCOs measured using $Ma_\infty = 0.9$, $\alpha = 0.0°$ and increasing the free-stream velocity V_∞

Free-stream velocity V_∞ (m/s)	Plunge amplitude a_h (mm)	Pitch amplitude a_α (deg)
255	3.85	9.4
280	4.2	10.4
310	5.2	10.4

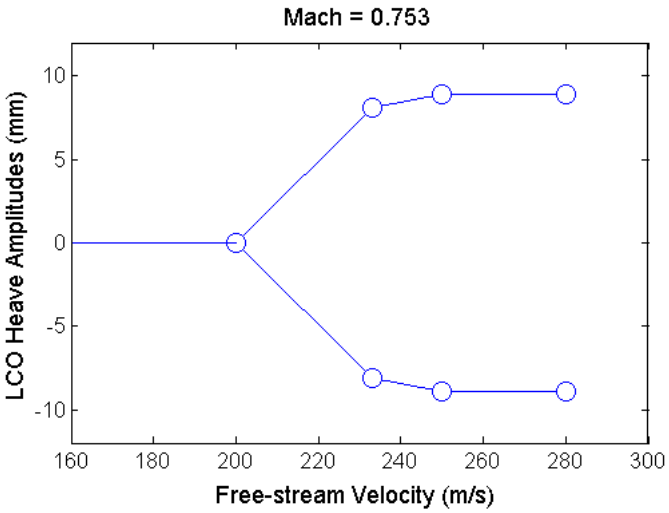

(a) Bifurcation for $Ma_\infty = 0.753$

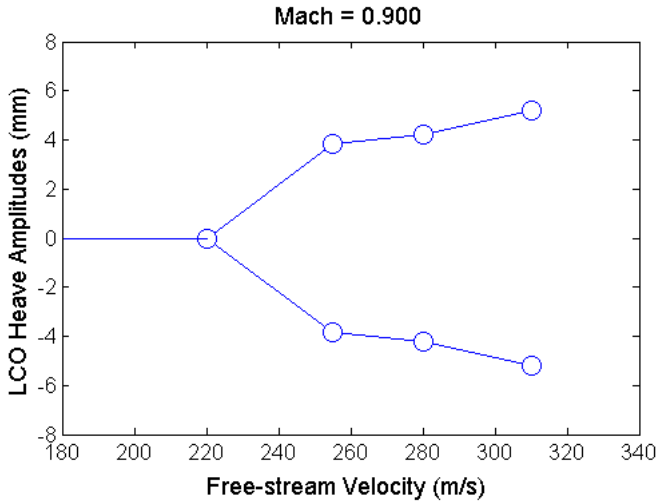

(b) Bifurcation for $Ma_\infty = 0.9$

Figure 5.44: NLR7301 bifurcation diagrams for $Ma_\infty = 0.753$ and $Ma_\infty = 0.9$ with $\alpha = 0.0^\circ$

Chapter 6

Conclusion and Outlook

In this work, starting from several CFD simulations for the training process, two different reduced order models have been employed in order to approximate the nonlinear aerodynamic response of the NLR7301 aerofoil in the transonic regime. Finally, a complete nonlinear aeroelastic analysis based on ROMs has been carried out with the aim of studying the limit cycle oscillations (LCO).
The aerodynamic reduced order modeling approaches have been presented, as well as the radial basis function network (RBF) and the local linear model tree algorithm (LOLIMOT). It was demonstrated that both ROMs can adequately capture the main nonlinearities aerodynamic effects of a phenomenon which has been obtained with a very large dynamic system. Generally, it was shown that the RBF-NN error in the prediction of the generalized aerodynamic forces is smaller than the error which occurs employing the LOLIMOT-ROM. The LOLIMOT model seems to be more suited to approximate the aerodynamic response of a signal that involves steady values, like plateaus in the APRBS. Nevertheless, using the LOLIMOT it is possible to adopt higher input-output delays orders, because this kind of model presents better properties in terms of numerical stability for all the signals tested in this work. It has been seen that the accuracy of the reduced order model employed to capture the nonlinear aerodynamic response depends strictly on the considered system and the efficiency of the training signal. This is why the training process is a key point in the ROMs building. In this context, the training

signal should have the right amount of informations, amplitudes and frequencies, in order to design a ROM fitted for the user's purposes. The use of a training signal which possesses a lot of information, or more information than needed, leads to an increase in the computational time. A tradeoff must be achieved by the user. In this thesis, it was shown how different signals, from those proposed in Nelles [27], can train the ROM and capture the main aerodynamic nonlinearities better. Among these, the random signal stands out particularly, managing to approximate the generalized aerodynamic forces with only a maximum mean squared error of the order of 10^{-6}. Thus, it has been demonstrated that the employment of a ROM can approximate the aerodynamic response of the system with a small error. Consequently, the CFD simulations could be reduced, because a well trained ROM can simulate the response of the system tested with other different signals. In this context, in the future, it will be possible to employ the ROMs in order to test the aircraft response to the air turbulence or to other signals which come from external/internal environment (gust, control device noise, pilot's maneouvre [26], etc.). A first attempt to capture the response of the system imposed by a turbulence has been realized in this work with good results.

Subsequently, the ROMs employed in this work have been used for a nonlinear aeroelastic analysis in order to capture the limit cycle oscillations that arise due to the shocks motion on the aerofoil in the transonic regime. Here, the ROM has been coupled with a structural solver to build the fluid-structure interaction.

The amplitudes and the frequencies of the LCOs obtained coupling the ROM with a structural model, which employs a hybrid linear multistep algorithm (HLM), show good agreements with those computed in Tang et al. [20] with the CFD-CSD simulation. The amplitudes computed in this work are higher than those measured in the wind tunnel by Knipfer et al. [2], whereas the frequency of the LCOs are the same measured in Tang. The much higher amplitudes of the heave and pitch motion depends strictly on the model used to solve the aerodynamic model and on real conditions, which occur in the wind tunnel, which have been neglected in this analysis. In Tang, it was demonstrated that the use of a viscous model allows to reach values of the heave LCO amplitudes less than $\frac{1}{3}$ relative to

those obtained with the Euler equations. Hence, another development could be the use of a RANS model as starting condition for the ROM in order to achieve solutions near the experimental values.
Thus, using a ROM coupled with a structural model, the LCO can well predict maintaining low the computational effort. As matter of fact, this kind of simulation permits to exploit a nonlinear aeroelastic analysis in few seconds starting from an already trained ROM.
One of the results of this work has been obtained comparing the LCOs that arise at different Mach numbers. When the Mach number is increasing, the shock waves get stronger on the aerofoil surfaces and their damping effect on the structure motion becomes more effective. Because of that, the heave amplitude of the LCOs becomes smaller.
Another relevant result has been obtained by increasing the free-stream velocity at a fixed Mach number. The higher the free-stream velocity, the faster the LCO is reached, for both the Mach numbers tested. Furthermore, increasing the free-stream velocity, the amplitude of the heave and pitch LCOs becomes higher getting the bifurcation diagrams.
Another interesting result has been achieved disturbing the aeroelastic system when the LCOs have already started. It has been demonstrated that the introduction of a disturb doesn't affect the response of the system, which follows the nature of the motion. In this case, it has been showed that the introduction of a relatively small impulse can control the amplitude of the LCO. Hence, using a control system it is possible to switch off this kind of nonlinearities reducing the relative vibration on the system and solving the relative problems. The fatigue life of the components can be increased reducing the substitution of the components itself and hence the costs to the aircraft maintenance. Furthermore, the LCOs analysis can lead to an improvement in the fighter aircraft keeping safe the integrity of the weapons attached on the wings and reducing the level of fatigue and stress of the pilot himself.
The efficiency of the presented ROMs is of great interest, since with a limited computational effort it makes the employment of nonlinear dynamic behaviours

possible even in the first stages of an aircraft design, keeping practically the same level of accuracy as the CFD solution. Furthermore, the accurate prediction of these nonlinearities can be a significant contribution to define a safelight envelope required by modern aircrafts or a range of working conditions for turbomachines.

Bibliography

[1] ANDERSON A. *Fundamentals of Aerodynamics*. McGraw-Hill, 2001.

[2] KNIPFER A. and SCHEWE G. Investigation of an oscillating supercritical 2d wing section in a transonic flow. Reno, Nevada, January 1999. 37th Aerospace Sciences Meeting and Exhibit.

[3] HARRIS C. D. Nasa supercritical airfoils; a matrix of family related airfoils. Technical report, NASA Langley Research Center; Hampton, VA, United States, Washington, 1990.

[4] DENEGRI C. M. Limit cycle oscillation flight test results of a fighter with external stores. *Aircraft Journal*, 37(5):761–769, 2000.

[5] FLEISCHER D. Schulung Euler-Verfahren Eu/SDEu: Theoretische Grundlagen, Programmaufbau, Programmanwendung. TUM, Garching bei München, 2008.

[6] LUCIA D. J., BERAN P. S., and SILVA W. A. Reduced-order modeling: new approaches for computational physics. *Progress in Aerospace Sciences*, 40(1-2):51–117, 2004.

[7] TANG D. M., KERRY J. K., and DOWELL E. H. Limit cycle oscillations of delta wing models in low subsonic flow. *AIAA Journal*, 37(11):1355–1362, 1999.

[8] JONES D. P., ROBERTS I., and GAITONDE A. L. Identification of limit cycles for piecewise nonlinear aeroelastic systems. *Journal of fluids and structures*, 23(7):1012–1028, 2007.

[9] KREISELMAIER E. Berechnung instationäre Tragflügelumströmungen auf Basis der zeitlinearisierten Eulergleichungen: Dissertation. Master's thesis, Garching bei München, 1997.

[10] DOWELL E. H., THOMAS J. P., and HALL K. C. Transonic limit cycle oscillation analysis using reduced order aerodynamic models. *Journal of fluids and structures*, 19(5):1212, April 2004.

[11] DOWELL E. H. and HALL K. C. Modelling of fluid-structure interaction. *Fluid Mech.*, 33:445–490, 2001.

[12] DOWELL E. H., CLARK R., COX D., and CURTIS H. C. *A Modern Course In Aeroelasticity.* Kluver Academic Publishers, 2004.

[13] DIETZ G., SCHEWE G., and MAI H. Experiments on heave/pitch limit-cycle oscillations of a supercritical airfoil close to the transonic dip. *Journal of fluids and structures*, 19(1):1–16, January 2004.

[14] SCHEWE G., KNIPFER A., and MAI H. Experimentelle und numerische Untersuchung nichtlineare Effecte beim transonischen Flattern. *DLR Göttingen*, 2001.

[15] VIO G.A., DIMITRIADIS G., and COOPER J. E. Bifurcation analysis and limit cycle oscillation amplitude prediction methods applied to the aeroelastic galloping problem. *Journal of fluids and structures*, 23(7):983–1011, 2007.

[16] THOMAS J. P., DOWELL E. H., and HALL K. C. Nonlinear inviscid aerodynamic effects on transonic divergence, flutter, and limit-cycle oscillations. *AIAA Journal*, 40(4):638–646, April 2002.

[17] WRIGHT J. R. and COOPER J. E. *Introduction to Aircraft Aeroelasticity and Loads.* John Wiley and Sons Ltd, 2007.

[18] EDWARDS J. W. Transonic shock oscillations and wing flutter calculated with an interactive boundary layer coupling method. Simulation of Fluid-Structure Interaction in Aeronautics, Göttingen, Germany, September 1996. EROMECH-Colloquium 349.

[19] KOUSEN K. and BENDIKSEN O. O. Nonlinear aspects of the transonic aeroelastic stability problem. 29th Structures, Structural Dynamics and Materials Conference, 1988.

[20] TANG L., BARTELS R. E., CHEN P. C., and D. D. LIU. Numerical investigation of transonic limit cycle oscillations of a two-dimensional supercritical wing. *Journal of fluids and structures*, 17(1):29–41, January 2003.

[21] WINTER M. *Numerische Flatteranalyse im Frequenzbereich.* PhD thesis, Technische Universität München, Lehrstuhl für Aerodynamik und Strömungsmechanik, 2012.

[22] WINTER M. Entwicklung von Verfahren reduzierter Ordnung für die instationäre aeroelastische Analyse basierend auf neuronalen Netzwerkstrukturen. *STAB Workshop*, 2013.

[23] WINTER M. and BREITSAMTER C. Reduced-order modeling of unsteady aerodynamic loads using radial basis function neural networks. Paper 340013, Augsburg, Germany, 2014. Deutscher Luft- und Raumfahrtkongress.

[24] PATIL M. J. and HODGES D. H. Limit cycle oscillations of a complete aircraft. Number 1395. 41st AIAA Structures, Structural Dynamics, and Materials Conference and Exhibit, 2000.

[25] HENSHAW M.J. de C., BADCOCK K.J., VIO G.A., and Allen C.B. Nonlinear aeroelastic prediction for aircraft applications. *Progress in Aerospace Sciences*, 43:65–137, 2007.

[26] KUMAR N. S. Input excitation techniques for aerodynamic derivatives-estimation of highly augmented fighter aircraft. *Defence Science Journal*, 49(3):187–196, July 1999.

[27] NELLES O. *Nonlinear System Identification, From Classical Approaches to Neural Networks and Fuzzy Models*. 2001.

[28] BENDIKSEN O. O. Review of unsteady transonic aerodynamics: Theory and applications. *Progress in Aerospace Sciences*, 47(2):135–167, February 2010.

[29] NIYOGI P. and GIROSI F. On the relationship between generalization error, hypothesis complexity and sample complexity in regularization networks. *Proceedings of IEEE*, 8:819–842, 1996.

[30] CHEN PC., DENEGRI CM., and SULAEMAN E. Influence of external store aerodynamics on flutter/lco of a fighter aircraft. Number 1410, Denver, Colorado, April 2002. 43rd AIAA Structures, Structural Dynamics, and Materials Conference.

[31] KAMAKOTI R. and SHYY W. Fluid-structure interaction for aeroelastic applications. *Progress in Aerospace Sciences*, 40(8):535–558, November 2004.

[32] LOT R. *Meccanica delle vibrazioni*. ESU Padova, 2012-2013.

[33] CHEN S., COWAN C.F.N., and GRANT P.M. Orthogonal least squares learning algorithm for radial basis function networks. *IEEE transactions on neural networks*, 2(2):302–309, 1991.

[34] HAYKIN S. *Neural Networks, A Comprehensive Foundation*. Prentice Hall Internation, Inc., 2nd edition edition, 1999.

[35] TOUMIT S. and DARRACQ D. Simulation of flutter boundary and hopf bifurcation of a 2dof airfoil. Barcelona, September 2000. ECCOMAS.

[36] WEBER S., JONES K. D., EKATERINARIS J. A., and PLATZER M. F. Transonic flutter computations for the nlr 7301 supercritical airfoil. *Aerospace Science Technology*, 5(4):293–304, June 2001.

[37] SCHUMACHER T. Coupling of aerodynamic reduced-order models with structural dynamics for aeroelastic analysis. Master's thesis, Technische Universität München, Lehrstuhl für Aerodynamik und Strömungsmechanik, 2014.

[38] MEGSON T. H. G. *Aircraft Structures for Engineering Students*. Elsevier, 5th edition, 2007.

[39] ZHANG W. and WANG B. Efficient method for limite cycle flutter analysis by nonlinear aerodynamic reduced-order models. *AIAA Journal*, 50(5):1019–1028, May 2012.

[40] ZHANG W. and YE Z. Effect of control surface on airfoil flutter in transonic flow. *Acta Astronautica*, 66(7-8):999–1007, April 2010.

[41] SILVA W. A. Simultaneous excitation of multiple-input multiple-output cfd-based unsteady aerodynamic system. *Journal of Aircraft*, 45(4):1267–1274, 2007.

[42] ZHU Y. *Multivariable System Identification for Process Control*. 2001.

Appendix A

NLR-7301 aerofoil

Table A.1: Parameters of the set-up NLR7301 according to Tang et al. [20]

Parameters	**Symbol**	**Unit**	**Value**
Total mass	m_h	kg	26.64
Mass moment of inertia about the quarter-chord line	$I_c/4$	$kg \cdot m^2$	0.086
Static unbalance	s_α	$kg \cdot m$	0.378
Damping factor of the plunge motion	D_h	$kg \cdot s^{-1}$	82.9
Damping factor of the pitch motion	D_α	$kg \cdot m^2 \cdot rad^{-1} \cdot s^{-1}$	0.197
Stiffness of the plunge spring	K_h	$N \cdot m^{-1}$	$1.21 \cdot 10^6$
Stiffness of the pitch spring	K_α	$N \cdot m \cdot rad^{-1}$	$6.68 \cdot 10^3$
Undamped natural frequencies of the plunge motion	ω_h	$rad \cdot /s$	205.4
Undamped natural frequencies of the pitch motion	ω_α	$rad \cdot /s$	299.3
Plunge damping ratios	ξ_h		0.00649
Plunge damping ratios	ξ_α		0.00521